



**NTNU – Trondheim**  
Norwegian University of  
Science and Technology

# Fatigue Assessment of Threaded Riser Connections

**Moritz Braun**

Marine Technology

Submission date: June 2014

Supervisor: Torgeir Moan, IMT

Co-supervisor: Gunnar Härkegård, IPM

Norwegian University of Science and Technology  
Department of Marine Technology





Version	Date	Comment
1.0	10. June 2014	final version

I certify that the work presented here is, to the best of my knowledge and belief, original and the result of my own investigations, except where otherwise indicated. It has not been submitted, either in part or whole, for a degree at any other University. I gratefully acknowledge supervision and guidance I have received from Prof. Gunnar Härkegård, Anders Wormsen from FMC, and Philippe Maincon and Vidar Osen from SINTEF.

Moritz Braun

Copyright © 2014, Moritz Braun

No part of this work may be reproduced, stored in a retrieval system or transmitted in any form or by any means, electronic, mechanical, photocopying, recording or otherwise, without prior permission.

Moritz Braun  
Norwegian University of  
Science and Technology  
Otto Nielsens veg 10  
NO-7491 Trondheim Norway  
Tel: + 47 402 997 26  
email: [moritz.br@googlemail.com](mailto:moritz.br@googlemail.com)

**MASTER THESIS SPRING 2014  
FOR  
STUD.TECHN.MORITZ BRAUN**

**FATIGUE ASSESSMENT OF THREADED RISER CONNECTIONS  
Utmattingsvurdering av gjengede stigerørsforbindelser**

A riser carries oil or gas between a wellhead and a production unit (platform or ship). A riser consists of several pipes connected by threaded joints. Movements between the production unit and the riser cause variable loading of the riser, which may lead to fatigue damage. In particular, this holds for the threaded joints. It is therefore of considerable interest to make a fatigue assessment of the riser connections.

The following Master Assignment comprises stress analyses as well as peak-stress (S-N) and crack-growth ( $da/dn$ ) based fatigue life predictions of threaded riser connections and a comparison with experimental observations.

- Stress analysis of threaded riser connections, for which fatigue test data are available, with focus on specimens tested by Wittenberghe [1] (optional: FMC connections)
  - 2D (axisymmetric) modelling whenever feasible
  - Make a clear distinction between (due to plasticity and contact phenomena possibly non-linear) 'make-up' pre-stressing and (generally linear elastic) cyclic stressing due to external loading
- S-N based fatigue assessment (systematic overview of relevant standards and criteria)
  - DNV-RP-C203 [2], ISO 13628-7 [3]
  - ASME BPVC Div. 2 and Div. 3 [4]
  - Other standards or handbooks
  - (Optional) Taking pressure cycling into account
  - Compare predicted fatigue lives with experimental observations
- Calculate the final crack size from a failure assessment diagram using LINKpipe or procedure outlined in BS 7910; according to ASME Div. 3, S-N based fatigue assessment is permissible only if leak-before-burst can be ensured
- FCG based fatigue assessment using suitably chosen  $da/dn$  data
  - 2D stress distribution (BS 7910, ASME BPVC Div. 3: Buchalet-Bamford method, Bueckner weight function)
  - (Optional) 3D stress distribution (LINKpfat)
  - (Optional) Taking pressurised crack surfaces into account
  - Compare predicted fatigue lives with experimental observations
- Optional: Implement selected methods and criteria in LINKpfat; post-processing of 2D stress fields

## References

1. Jeroen Van Wittenberghe, Experimental Analysis and Modelling of the Fatigue Behaviour of Threaded Pipe Connections, PhD Thesis.
2. Recommended practice DNV-RP-C203, *Fatigue Design of Offshore Steel Structures*, October 2012,  
[http://exchange.dnv.com/publishing/Codes/ToC\\_edition.asp#Standards](http://exchange.dnv.com/publishing/Codes/ToC_edition.asp#Standards).
3. ISO 13628-7:2005 Petroleum and natural gas industries -- Design and operation of subsea production systems -- Part 7: Completion/workover riser systems
4. J.R. Sims, Jr. Section VIII, Div. 3, Alternative rules for the construction of high-pressure vessels. *Companion Guide to the ASME BPVC*.

Three weeks after start of the thesis work, an A3 sheet illustrating the work is to be handed in. A template for this presentation is available on the IPM's web site under the menu "Masteroppgave" (<http://www.ntnu.no/ipm/masteroppgave>). This sheet should be updated one week before the Master's thesis is submitted.

Performing a risk assessment of the planned work is obligatory. Known main activities must be risk assessed before they start, and the form must be handed in within 3 weeks of receiving the problem text. The form must be signed by your supervisor. All projects are to be assessed, even theoretical and virtual. Risk assessment is a running activity, and must be carried out before starting any activity that might lead to injury to humans or damage to materials/equipment or the external environment. Copies of signed risk assessments should also be included as an appendix of the finished project report.

The thesis should include the signed problem text, and be written as a research report with summary both in English and Norwegian, conclusion, literature references, table of contents, etc. During preparation of the text, the candidate should make efforts to create a well-arranged and well-written report. To ease the evaluation of the thesis, it is important to cross-reference text, tables and figures. For evaluation of the work, a thorough discussion of results is appreciated.

The thesis shall be submitted electronically via DAIM, NTNU's system for Digital Archiving and Submission of Master's thesis.

Contact persons are:

Prof. B. Haugen NTNU/IPM

V. Osen LINKftr AS

Dr.ing. A. Wormsen FMC Kongsberg

Torgeir Moan  
Main Supervisor

Gunnar Härkegård  
Professor/Supervisor

# Fatigue assessment of threaded riser connections

Master Thesis

Moritz Braun

Delivered: 10.06.2014

**Abstract:** Threaded connections as found in applications like rigid riser, drillstrings, and workover riser are manufactured with sharp notches. Subjected to cyclic loading, those notches lead to high stress concentrations, which increase the risk of fatigue crack initiation significantly. A common connection type that has been the basis for extensive studies is the API Line Pipe connection.

The basic API thread type consists of truncated triangular threads. In order to tighten the connection the male and female part or pin and box are assembled by applying a make-up torque. This process already leads to stress in the connection that exceed the material yield strength at the roots of the threads. Subjected to cyclic loading a complex stress state arises at the thread roots of both parts of the connection. From screwed connections it is known that approximately half of the axial load is carried by the last engaged thread. Consequently, fatigue cracks develop at this location.

Fatigue assessment of threaded riser connections (TRC) is commonly based on a peak stress approach. This is the prescribed method in standards and recommended practices like DNV-RP-C203, BS 7608 or ASME B31.3. For this purpose, the peak stress at the root of the last engaged thread is found by finite element analysis (FEA). Subsequently, a given design curve is corrected for the notch effect of the thread root and the fatigue life of a connection can be calculated by means of linear damage accumulation. It was shown in different research projects that fatigue assessment of TRC based on this method leads to overly conservative lifetime estimates when combining design curves with FEA.

In order to achieve more precise lifetime estimates, alternative fracture mechanics methods based on ASME BPVC VIII-3-App. D have been applied. The intention was to establish stress-life diagrams for design purposes of threaded riser connections based on alternative methods. Moreover, comparison of the chosen approach and test results was included to review the obtained results.

It was found that the chosen fracture mechanics methods yield unconservative results, when compared with test data, common stress - life design curves and other methods based on the peak stress approach.

Advisor: Prof. Gunnar Härkegård, Dr.ing. Anders Wormsen, Prof. Torgeir Moan

Number of pages: 62 + Appendix

# Contents

<b>1. Introduction</b>	<b>1</b>
1.1. Motivation . . . . .	1
1.2. Objective . . . . .	2
1.3. Structure of the Thesis . . . . .	3
<b>2. Fatigue Assessment based on Deterministic Methods</b>	<b>4</b>
2.1. Introduction . . . . .	4
2.2. Stress-Based Methods . . . . .	4
2.2.1. Fundamentals . . . . .	4
2.2.2. The Peak Stress Method . . . . .	5
2.2.3. Discussion of the Stress-Based Methods . . . . .	6
2.3. Fracture Mechanics Methods . . . . .	6
2.3.1. Basic Theory . . . . .	6
2.3.2. Weight Function Method . . . . .	8
2.3.3. Discussion of the Fracture Mechanic Method . . . . .	10
<b>3. Threaded Riser Connections</b>	<b>11</b>
3.1. Connection Details . . . . .	11
3.2. Load Condition . . . . .	12
<b>4. Finite Element Analysis</b>	<b>13</b>
4.1. Introduction . . . . .	13
4.2. FE Models . . . . .	13
4.3. Axisymmetric Model . . . . .	14
4.3.1. Mesh . . . . .	15
4.3.2. Loading Condition . . . . .	16
4.3.3. Simulation of Make-up Processes . . . . .	17
4.3.4. Make-up Process of the 1" API Line Pipe Connection . . . . .	19
4.3.5. Results of Model with Elastic-Plastic Material Model . . . . .	21
4.3.6. Results of Model with Linear Elastic Material Model . . . . .	24
4.4. 3D Model . . . . .	25
4.4.1. Mesh . . . . .	26
4.4.2. Results of 3D Model . . . . .	29
4.5. Finite Element Post-Processor LINKpfat . . . . .	31
<b>5. Fatigue Assessment of Threaded Riser Connections</b>	<b>33</b>
5.1. Introduction . . . . .	33
5.2. Overview of relevant standards and criteria . . . . .	33
5.3. Peak Stress Approach . . . . .	34
5.4. Fracture Mechanics Methods . . . . .	36
5.4.1. ASME Crack Growth Method . . . . .	37



5.4.2. Weight Function Method . . . . .	39
5.4.3. LINKpfat Simulations . . . . .	42
5.4.4. Fatigue Crack Growth Data and Fatigue Limit . . . . .	43
5.5. Results of Fracture Mechanics Methods . . . . .	44
5.5.1. Results of ASME Crack Growth Method . . . . .	45
5.5.2. Results of Weight Function Method . . . . .	47
5.5.3. Results of LINKpfat Simulations . . . . .	48
5.6. Comparison of Fatigue Assessment Methods and Test Data . . . . .	50
<b>6. Summary and Conclusion</b>	<b>53</b>
<b>7. Suggestion for Future Work</b>	<b>57</b>
<b>Bibliography</b>	<b>58</b>
<b>A. FE results</b>	<b>63</b>
A.1. Results of axisymmetric model with elastic-plastic material model . . . . .	63
A.2. Results of 3D model . . . . .	64
<b>B. Fatigue crack growth calculation</b>	<b>65</b>
B.1. Polinomial fitting of stress field . . . . .	65
B.2. Weight function method . . . . .	67
<b>C. Source code</b>	<b>70</b>

# List of Figures

1.1. Crack initiation at the root of the last engaged thread of a TRC . . . . .	1
2.1. Crack growth stages . . . . .	7
2.2. Weight function method based on superposition principle . . . . .	8
2.3. Example of the notation and the coordinate system for the one-dimensional weight function . . . . .	9
2.4. Integration of weight function . . . . .	10
3.1. Thread geometry . . . . .	11
3.2. Schematic view of the API Line Pipe connection . . . . .	12
4.1. Sketch of the 2D axisymmetric model of the API Line Pipe connection . . . . .	14
4.2. Elastic plastic material data . . . . .	15
4.3. Mesh of the 2D axisymmetric model of the API Line Pipe connection . . . . .	16
4.4. Mesh at the root of the LET of the 2D axisymmetric model . . . . .	17
4.5. Sketch of a drilling riser connection with interferences and contact pressures . . . . .	18
4.6. Interference of the contact surfaces for the final configuration . . . . .	20
4.7. Pressure distribution along the thread flanks . . . . .	21
4.8. Von Mises stress results of the full 2D axisymmetric model of the 1" API Line Pipe connection with elastic-plastic material model . . . . .	22
4.9. Equivalent plastic strain at the root of the LET of the 2D axisymmetric model of the 1" API Line Pipe connection made of API Grade B steel . . . . .	23
4.10. Axial stress results of the 2D axisymmetric elastic-plastic model of the 1" API Line Pipe connection . . . . .	24
4.11. Von Mises stress results of the full 2D axisymmetric elastic model of the 1" API Line Pipe connection . . . . .	25
4.12. Axial stress results of the 2D axisymmetric elastic model of the 1" API Line Pipe connection . . . . .	26
4.13. 3D model of the 1" API Line Pipe connection . . . . .	27
4.14. Mesh of the first submodel . . . . .	27
4.15. Mesh of the second submodel . . . . .	28
4.16. Von Mises stress result after the make-up process and a tensile stress of 44.4 MPa of the 2nd 3D submodel of the 1" API Line Pipe connection with linear elastic material model . . . . .	29
4.17. Axial stress result after the make-up process and a tensile stress of 44.4 MPa of the 2nd 3D submodel of the 1" API Line Pipe connection with linear elastic material model . . . . .	30
4.18. Comparison of 2D and 3D stress field along the anticipated crack growth path . . . . .	31
5.1. Stress gradient from a notch including peak stress . . . . .	35
5.2. Cyclic stress-strain results at the root of the LET for $S_a = 10$ MPa and $R=0.1$ . . . . .	36

5.3. Basis of ASME crack growth method . . . . .	37
5.4. Illustration of the method for correcting $K_I$ if several polynomial fits are used to describe the stress field . . . . .	39
5.5. Fracture surface of a fatigue crack in a 1" API Line Pipe connection specimen . .	40
5.6. Initial crack at the thread root of the LET in LINKpfat with the axial stress results for a nominal tensile stress of 44.4 MPa . . . . .	43
5.7. S-N curve for the 1" API Line Pipe connection made of API Grade B steel based on ASME FCG method . . . . .	45
5.8. Comparison of the S-N curve for the 1" API Line Pipe connection models from project and master thesis based on the ASME method . . . . .	46
5.9. Change of stress intensity factors and stress intensity factor ranges during crack growth from an initial crack with depth $a_i = 0.1$ mm and nominal tensile stress amplitude $S_a = 10$ MPa . . . . .	47
5.10. Number of elapsed cycles per crack growth increment of a crack with initial crack depth $a_i = 0.1$ mm and $S_a = 10$ MPa . . . . .	48
5.11. Crack growth stages of a crack with aspect ratio $a/c = 0.2$ from an initial crack with depth $a_i = 0.1$ mm and $S_a = 10$ MPa . . . . .	49
5.12. Final crack at the thread root of the LET in LINKpfat with the axial stress results for a nominal tensile stress of 44.4 MPa . . . . .	49
5.13. Comparison of the S-N curve for the 1" API Line Pipe connection models based on the results from weight function method and LINKpfat . . . . .	50
5.14. S-N curves for the 1" API Line Pipe connection . . . . .	51
A.1. Axial stress distribution of the 2D axisymmetric model of the API Line Pipe connection from the root of the LET for a tensile stress of 150 MPa . . . . .	63
A.2. Equivalent strain distribution of the 2D axisymmetric model of the API Line Pipe connection from the root of the LET for a tensile stress of 150 MPa . . . . .	63
A.3. Von Mises stress results of the full 3D model of the 1" API Line Pipe connection with linear elastic material model . . . . .	64
A.4. Von Mises stress results of the 1st 3D submodel of the 1" API Line Pipe connection with linear elastic material model . . . . .	64
B.1. Total axial stress distribution from the root of the LET for a tensile stress of 44.4 MPa with 3rd order polynomial fit . . . . .	65
B.2. Part 1 of the axial stress distribution from the root of the LET for a tensile stress of 44.4 MPa . . . . .	66
B.3. Part 2 of the axial stress distribution from the root of the LET for a tensile stress of 44.4 MPa . . . . .	66
B.4. Crack growth results for a crack depth $a = 0.3$ mm and a nominal tensile stress amplitude of 10 MPa . . . . .	67
B.5. Crack growth results for a crack depth $a = 1$ mm and a nominal tensile stress amplitude of 10 MPa . . . . .	68
B.6. Crack growth results for a crack depth $a = 3.21$ mm and a nominal tensile stress amplitude of 10 MPa . . . . .	69

# List of Tables

4.1. Material properties of API Grade B as used in FEA . . . . .	15
4.2. Mesh details of 2D axisymmetric model . . . . .	16
4.3. Comparison of results at the root of the LET from 2D axisymmetric elastic-plastic model with the results of van Wittenberghe . . . . .	24
4.4. Mesh details of global 3D model . . . . .	28
4.5. Mesh details of global 1st 3D submodel . . . . .	28
4.6. Mesh details of global 2nd 3D submodel . . . . .	29
4.7. Comparison of results from 2D axisymmetric elastic model with the results of the 2nd 3D submodel . . . . .	30
4.8. LINKpfat modules . . . . .	31
5.1. Fatigue crack growth parameter . . . . .	43
5.2. S-N curves used for comparison . . . . .	51

# List of Abbreviations

<b>API</b>	American Petroleum Institute
<b>ASME</b>	American Society of Mechanical Engineers
<b>C/WO</b>	Completion/ workover
<b>FCG</b>	Fatigue crack growth
<b>FEA</b>	Finite element analyses
<b>LEFM</b>	Linear elastic fracture mechanics
<b>LET</b>	Last engaged thread
<b>S-N</b>	Stress-life
<b>TRC</b>	Threaded riser connection

# List of Formulas

Symbol	Unit	Meaning
$a$	mm	Crack depth
$a_{eff}$	mm	Effective crack depth
$a_i$	mm	Initial crack depth
$a_{inc}$	mm	Crack growth increment
$A$	–	Interception of S-N curve with the log $N$ axis
$A_0, A_1, A_2, A_3$	–	Coefficients of polynomial fit
$b$	–	Slope of the S-N curve
$c$	mm	Crack width
$C$	$(\text{mm/cycle})/(\text{MPa}\sqrt{\text{mm}})^m$	Paris coefficient
$C_1$	kNm/mm	Interference correction factor
$D_i$	mm	Inner diameter
$D_o$	mm	Outer diameter
$D_p$	mm	Pin diameter
$D_S$	mm	Outer diameter at the end of the shoulder stop face
$E$	GPa	Young's modulus
$f_s$	–	Coefficient of friction
$F$	–	Geometrical form function
$F_1, F_2, F_3, F_4$	–	Magnification factor of ASME FCG method
$K_c$	$\text{MPa}\sqrt{\text{mm}}$	Fracture toughness
$K_I$	$\text{MPa}\sqrt{\text{mm}}$	Stress intensity factor
$K_{I,region1}$	$\text{MPa}\sqrt{\text{mm}}$	Stress intensity factor of 1. region
$K_{I,region2}$	$\text{MPa}\sqrt{\text{mm}}$	Stress intensity factor of 2. region
$K_t$	–	Geometrical stress concentration factor
$i$	–	ASME S-N correction factor
$I_c$	mm	Interference at the conical thread-free portion
$I_r$	mm	Radial interference
$I_s$	mm	Axial interference at the shoulder stop face
$l$	mm	Notch depth
$L_c$	mm	Contact length at the conical thread-free portion
$L_f$	mm	Contact length at the thread flanks
$L_r$	mm	Contact length at the thread roots
$m$	–	Slope of the Paris curve
$m_a$	–	Weight function in depth direction a
$m_b$	–	Weight function in direction c

Symbol	Unit	Meaning
$M_b$	Nm	Bending moment
$M_{i,j}$	Nm	Weight function parameter number $i$ for point $j$
$M_{up}$	Nm	Make-up torque
$n_f$	–	Number of engaged thread flanks
$N_f$	–	Number of cycles to failure
$N_i$	–	Number of elapsed cycles
$n_r$	–	Number of engaged thread root sections
$p$	MPa	Contact pressure
$p_c$	MPa	Contact pressure at the conical thread-free portion
$p_{f,i}$	MPa	Contact pressure at thread flank $i$
$p_{r,i}$	MPa	Contact pressure at thread root $i$
$p_s$	MPa	Contact pressure at the shoulder stop face
$R$	–	Stress ratio
$R_C$	–	Stress ratio for which $C$ was given
$S$	MPa	Nominal stress
$S_a$	MPa	Nominal stress amplitude
$S_A$	MPa	Fatigue limit
$S_{max}$	MPa	Maximum nominal stress
$S_{min}$	MPa	Minimum nominal stress
$S_p$	N	Splitting force
$T_1$	Nm	Friction torque corresponding to a coefficient of friction of 1
$T_h$	Nm	Helix torque term
$T_S$	Nm	Torsional strength
$WT$	mm	Wall thickness
$\gamma$	–	Walker exponent
$\Delta K$	MPa $\sqrt{\text{mm}}$	Stress intensity factor range
$\Delta K_{1,2}$	MPa $\sqrt{\text{mm}}$	Difference of stress intensity factor where region 1 and 2 join
$\Delta K_{eff}$	MPa $\sqrt{\text{mm}}$	Effective stress intensity factor range
$\Delta K_{th}$	MPa $\sqrt{\text{mm}}$	Fatigue crack growth threshold
$\Delta M_b$	Nm	Bending moment range
$\Delta S$	MPa	Nominal stress range
$\Delta \sigma$	MPa	Stress range
$\nu$	–	Poisson's ratio
$\xi$	–	Relative crack depth $a/t$
$\rho$	mm	Fillet radius
$\sigma(x)$	MPa	Stress at location $x$
$\sigma_a$	MPa	Stress amplitude
$\sigma_{ar}$	MPa	Equivalent fully-reversed stress amplitude
$\sigma_b$	MPa	Bending stress
$\sigma_{max}$	MPa	Maximum or peak stress
$\sigma_{UTS}$	MPa	Ultimate tensile stress
$\sigma_Y$	MPa	Yield stress
$\chi$	–	Crack aspect ratio $a/c$

# 1. Introduction

## 1.1. Motivation

Threaded connections as found in applications like rigid riser, drillstrings, and workover riser are manufactured with sharp notches. Subjected to cyclic loading, those notches lead to high stress concentrations, which increase the risk of fatigue crack initiation significantly. Within a study for the oil and gas industry, Hill [33] reported that approximately 65% of all drillstring failures for example could be traced back to fatigue phenomena.

A common connection type that has been the basis for extensive studies is the API Line Pipe connection. The reason for this is its widely availability as standardized connection type [54]. Starting from the 1960's, advanced connection types have been developed [54], by changing small details like thread shape or wall thickness for example, to improve fatigue life. However, those so-called premium connections are usually patented and test results of such connections are therefore seldom published.

The basic API thread type as shown in figure 1.1 consists of truncated triangular threads. In order to tighten the connection the male and female part or pin and box are assembled by applying a make-up torque. This process already leads to stress in the connection that exceed the material yield strength at the roots of the threads. Subjected to cyclic loading a complex stress state arises at the thread roots of both parts of the connection. From screwed connections it is known that approximately half of the axial load is carried by the last engaged thread (LET) [10]. Consequently, fatigue cracks as seen in figure 1.1 develop at this location.

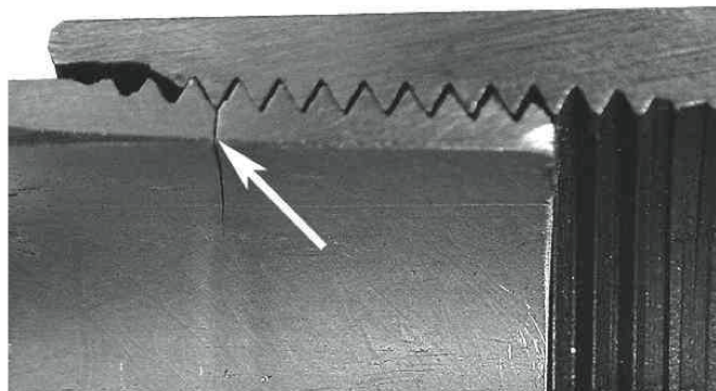


Figure 1.1.: Crack initiation at the root of the last engaged thread of a threaded riser connection taken from [54]

Fatigue assessment of threaded riser connections (TRC) is commonly based on a local stress



methods. This is the prescribed method in standards and recommended practices like DNV-RP-C203 [24], BS 7608 [17] or ASME B31.3 [6]. For this purpose, the peak stress at the root of the last engaged thread is found by finite element analysis (FEA). Subsequently, a given design curve is corrected for the notch effect of the thread root and the fatigue life of a connection can be calculated by means of linear damage accumulation.

It was shown in different research projects that fatigue assessment of TRC based on the peak stress approach leads to overly conservative lifetime estimates. The reason for this is that for example DNV's stress-life curves (S-N curves) are based on testing of smooth specimens. Correcting these curves for the maximum stress concentration due to the notch is overestimating the crack growth, since the crack is growing into a reduced stress field. Furthermore, up to date, no uniform industry standards exist regarding loading conditions, testing, and also damage detection. The combination of those problems leads to lifetime estimate of TRC that do not agree with actual test results [21]. A series of recent works on this field has been conducted, but the complete problem of the lifetime prediction procedure from load definition to lifetime estimates have not been possible to solve yet.

## 1.2. Objective

A lot of research projects focus on finding design improvements for TRC, but without the right tools to assess the effect on fatigue performance, none of the findings are reliable. In fact, it is usually tried to optimize the design by using FEA in connection with a peak stress approach [54], but, as has been shown by several authors, the results of this approach should be carefully assessed. The goal of this project shall therefore be to validate the applicability of other fatigue assessment methods for TRCs. Methods that seem to yield reasonable results are weakest-link [21], multi-axial fatigue models [26], and fracture mechanics approaches [9, 15, 54].

In an earlier master thesis by Cetin [21], different stress-based methods as well as a weakest-link approach have been studied with interesting results regarding their applicability. To complement his results this thesis will focus on fatigue crack growth (FCG) methods. For this purpose the following items were scheduled.

1. Stress analysis of TRC, for which test data are available, with focus on specimens tested by van Wittenberghe [54]
2. S-N based fatigue assessment
3. Calculation of final crack size from a failure assessment diagram
4. FCG based fatigue assessment

During the work on the thesis, it was realized that the final crack size calculation from a failure assessment diagram would rely on a significant number of assumptions. It was therefore agreed upon excluding this part from the master thesis. Instead, the optional task FCG based fatigue assessment based on a 3D stress distribution became a main item of the thesis.

### 1.3. Structure of the Thesis

The thesis has been divided into the following 6 parts.

1. Review of deterministic fatigue assessment methods that will be considered in this thesis
2. Short description of TRCs
3. FE modelling
4. Overview of relevant standards and criteria
5. Fatigue assessment based on selected methods
6. Discussion of results, summary, conclusion and suggestions for future work

Compared to the project thesis precedent to this master thesis, the scope of this master thesis has been extended to cover more fatigue assessment methods. For some of the new methods, additional FE models are required. For example a 3D model has been established. Moreover, the previous FE models and the simulation of the make-up process have been improved. Since the existing 2D axisymmetric model was updated, also the FCG based fatigue assessment methods of the project thesis has been improved and repeated.

## 2. Fatigue Assessment based on Deterministic Methods

### 2.1. Introduction

Many methods exist for fatigue assessment of a component or structure. One way of dividing fatigue assessment methods is into deterministic and probabilistic models. However, only deterministic approaches will be considered within this project. By a deterministic description the occurrence of an event A will definitely result in second event B. Whereas for probabilistic models the occurrence of an event A might lead to a second event B with a certain probability.

For a limit state deterministic description of failure it is sufficient that one single point satisfies the criterion. In other words, if for example the capacity of a structure is exceeded, failure is inevitable. In the following chapter two methods based on this assumption are introduced that will later be applied to fatigue assessment of TRCs.

### 2.2. Stress-Based Methods

#### 2.2.1. Fundamentals

Fatigue phenomena have been studied for more than 150 years now, but the basis for modern design strategies to avoid fatigue failure are mainly credited to August Wöhler. He laid the foundation for the so-called stress-based methods with his work that was motivated by railway axle failures. There are a lot of other authors who contributed to the development of fatigue failure investigation and the methods we use to predict and prevent accidents due to fatigue in materials. In particular Basquin [12] is worth mentioning for describing the relation between the number of cycles to failure  $N_f$  of a component and the applied stress amplitude  $S_a$  by a power law, which is referred to as Basquin's equation.

$$S_a = AN_f^b \quad , \quad (2.1)$$

with  $A$  as the characteristic fatigue strength or intercept of the design S-N curve with the log  $N$  axis and  $b$  as the slope of the S-N curve. Based on this assumption prediction of total life of a component are possible. For this purpose a number of test specimens are subjected to cyclic loading at different levels and the number of cycles to failure is measured. During these tests,

the load fluctuates with constant amplitude until failure occurs or a given number of cycles is reached. Fatigue test data is prone to scatter around a median, since every test specimen is different. Therefore, stochastic methods are used to find the parameter of Basquin's equation that yield the best fit to test data. The standard curve of failure is then corrected by two-standard-deviations [24]. The corresponding probability of failure for this curve is so reduced to only 2.28% which is more suitable for design purposes.

The stress amplitude against which the number of cycles is plotted, is usually a nominal stress, since it can easily be derived from the force applied in the experimental test setup. Moreover, no complex stress analysis is required to evaluate the stress state of the test specimen. On the other side, it is often infeasible to perform a sufficient number of tests for complex or large components. In such cases, it is necessary to find the relation between the local stress inside the component and a nominal stress that is applied to it. This is usually done by means of FEA, which has the advantage that smooth test specimen or S-N curves from standards can be used.

S-N curves are obtained by tests with constant amplitude loading, while in practice structures subjected to variable amplitude loading. In order to obtain a life estimate for the latter a load spectrum is divided into several blocks, and the damage calculated for each block is summed up by means of the cumulative fatigue damage model by Miner-Palmgren. This is based on the assumption that fatigue damage accumulates linearly, which means that damage for a given set of stress ranges can be superimposed, and that there is no interaction between different stress levels, in the sense that it is unimportant in which order the component experiences the stress cycles.

### 2.2.2. The Peak Stress Method

The peak stress method is the simplest form of the stress-based methods and a direct extension to cover cases, where local changes in geometry such as holes, fillets, and notches affect the stress field. At those positions, the stress is raised and the fatigue strength is consequently reduced. One way to describe this effect is to apply the concept of an elastic stress concentration factor  $K_t$  as follows:

$$K_t = \frac{\sigma_{max}}{S} \quad , \quad (2.2)$$

where the peak stress is expressed as  $\sigma_{max}$  and the nominal stress acting at the smallest cross-sectional area of the test specimen by  $S$ .

It is clear that fatigue failure is likely to initiate at position of higher local stresses. Fatigue assessment of components based on the peak stress approach consequently aims at finding the position of the peak stress and the corresponding magnitude.

As earlier mentioned, it is possible to utilize S-N curves obtained by testing of smooth specimens for fatigue design of complex structures, if the local stress is introduced in Basquin's equation.

The fatigue strength can so be expressed by the nominal stress acting at a well defined posi-

tion inside the structure and the maximum stress concentration factor due to a local change in geometry.

$$S_a = \frac{AN_f^b}{K_t} \quad (2.3)$$

### 2.2.3. Discussion of the Stress-Based Methods

However, many other methods exist for calculating the local stress that causes fatigue failure. Here only the peak-stress method was introduced. The advantages of this method are its wide applicability, because of the relatively simple formulation and the easy and quick fatigue assessment it permits. No complex stress analysis is needed, because the stress which the fatigue life is related too can be maximum principal stress or often just axial stress acting normal to the plane of the smallest cross-section. Moreover, S-N curves defined for smooth specimens can be used and results obtained by this method are usually on the safe side.

However, there are also important disadvantages to mention. The most important is probably that lifetime estimates based on this method are often overly conservative, especially for structures with sharp notches or other structural details that lead to steep stress gradients. The reason is that cracks that initiate at the notch tip grow into a region where the stress field is less pronounced. In addition, it is possible that at another position a more critical initial defect can be found. Moreover, no distinction is made between crack initiation and propagation, since this method aims at predicting the total lifetime of a component only.

## 2.3. Fracture Mechanics Methods

### 2.3.1. Basic Theory

As earlier mentioned the lifetime of a component can be divided into two stages. Those are the initiation of microscopic cracks and the growth of such cracks until failure of the component. Originally, fracture mechanics models were only meant for prediction of fatigue crack growth and therefore the component's crack propagation life, but lately extension have been made to cover the complete life cycle of components. However, it is unusual that a crack with dangerous size is initially present in the material. In general small defects also referred to as flaws are included in every engineering material due to manufacturing. Depending on their size, loading and the material properties they might initiate cracks which could later lead to fracture of the component. Therefore, regular inspections are necessary to assure that growing cracks are detected before they reach a critical size. In practice inspection methods and intervals are chosen pair wise according to the minimum crack size that can be detected and the expected time until such a crack grows to its critical size.

The basic of the fracture mechanic approach is formed by the so-called stress intensity concept. [25] Herein, the stress intensity factor  $K_I$  is a function of crack length, crack geometry and

location, and loading.

$$K_I = FS\sqrt{\pi a} \quad , \quad (2.4)$$

where  $S$  is the nominal stress in a crack-free body,  $F$  is a dimensionless geometrical form function depending on both the crack geometry and location, and  $a$  as the crack depth. This concept arose from linear elastic fracture mechanics (LEFM) and allows to relate the local conditions at the crack tip to the global parameter loading and overall geometry. It is therefore possible to condense a difficult three dimensional problem to a simple workable form [15].

Based on the work by Griffith and Irwin it can be shown that the local stress field around the crack tip can be expressed by the single parameter  $K_I$ . The stress intensity factor will increase with increasing crack depth  $a$  and therefore accelerate the crack growth itself. Considering a nominal stress range  $\Delta S$  it can be shown that a crack growth of  $\Delta a$  is primarily linked to the range of the stress intensity factor  $\Delta K$ .

$$\Delta K = F\Delta S\sqrt{\pi a} \quad (2.5)$$

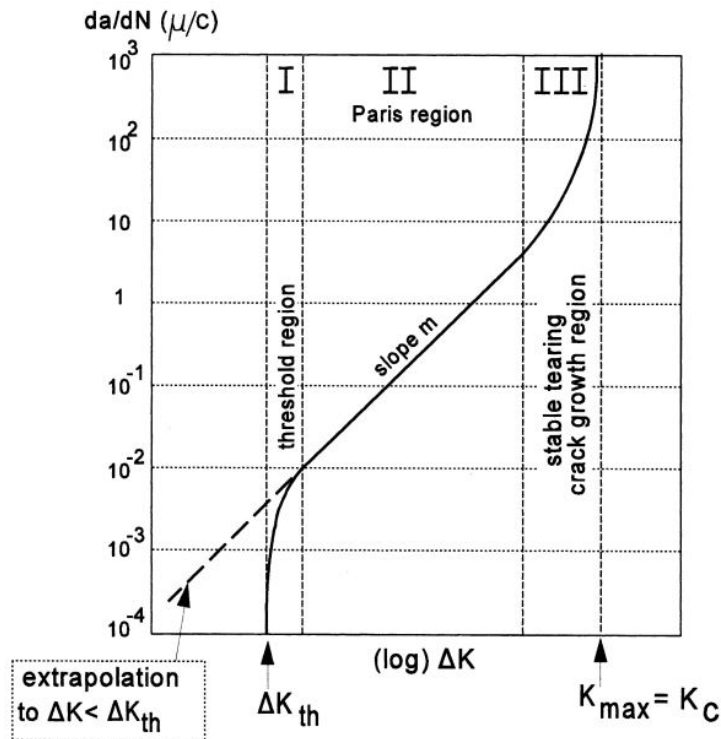


Figure 2.1.: Crack growth stages taken from [45]

The relation between the rate of crack growth per cycle  $da/dN$  and the stress intensity range  $\Delta K$  and the first application of fracture mechanics to fatigue was done by Paris in the early 1960s [25]. Plotting both quantities in a log-log diagram such as in figure 2.1, he found that the intermediate region of crack growth can be well described by a straight line. This yields the following expression in a linear scale on both axes:

$$\frac{da}{dN} = C\Delta K^m \quad , \quad (2.6)$$

with  $C$  and  $m$  as material constants. For low growth rates, the curve approaches a vertical asymptote  $\Delta K_{th}$ , referred to as fatigue crack growth threshold, below which no crack growth will occur. For high stress intensity factor ranges  $\Delta K$ , close to the critical value  $K_c$ , the curve approaches another vertical asymptote due to rapid crack growth. This maximum stress intensity factor  $K_c$  is referred to as fracture toughness, beyond which unstable fracture will occur.

However, the intermediate region is usually the one of main interest. Assume that the nominal loads  $S_{min}$ ,  $S_{max}$ , and the load ratio  $R$  is constant during a limited number of cycles it is often feasible to assume that the change of stress intensity factor range is small. In that case it is possible to obtain an expression for the number of elapsed cycles  $N_i$  required to grow a crack from an initial crack depth  $a_i$  to an arbitrary crack depth  $a$  by substituting the equation for the stress intensity factor into Paris law and integrating both sides.

$$N_i = \int_{a_i}^a \frac{da}{C\Delta K^m} = \frac{a_i}{\left(\frac{da}{dN}\right)|_{a=a_i}} \frac{1 - \left(\frac{a_i}{a}\right)^{\frac{m}{2}-1}}{\frac{m}{2} - 1} \quad (2.7)$$

### 2.3.2. Weight Function Method

In the previous section, LEFM and the stress intensity factor concept was introduced. However, due to its limitation to constant nominal stress fields and the fact that cracks usually occur in complex non-linear stress fields like around notches, the stress intensity factor for cracks at such locations cannot be calculated by means of equation 2.4. In order to overcome the shortcomings of calculating stress intensity factor from form functions and nominal loading, the weight function concept was proposed by Bueckner [20] and successively generalised by Rice [41].

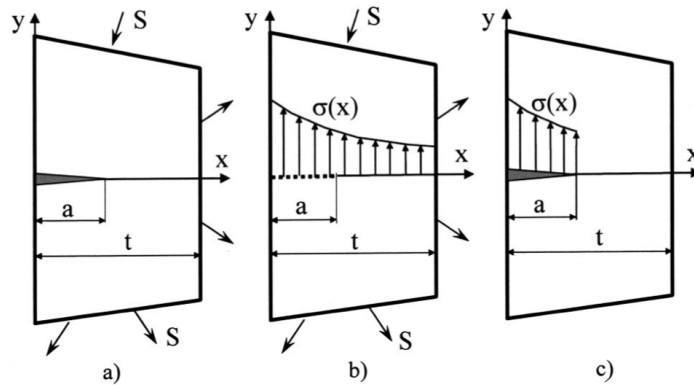


Figure 2.2.: Weight function method based on superposition principle taken from [36]

The local stress field is determined in the prospective crack plane of an uncracked body [36] and then superimposed on the crack body as illustrated in figure 2.2. In a one-dimensional case the

stress intensity factors  $K_I$  is obtained by integrating the product of local stress distribution  $\sigma(x)$  and weight function  $m(x, a)$  over the crack length  $a$ .

$$K_I = \int_0^a \sigma(x)m(x, a)dx \quad (2.8)$$

Once a weight function is found for a particular crack geometry, it can be used to find the stress intensity factor for every loading condition. Within the last 25 years a variety of generic weight functions have been published for different crack geometries. However, their mathematical form vary considerably, which was the reason for Glinka and Shen to propose a general weight function expression for one-dimensional mode I cracks [29].

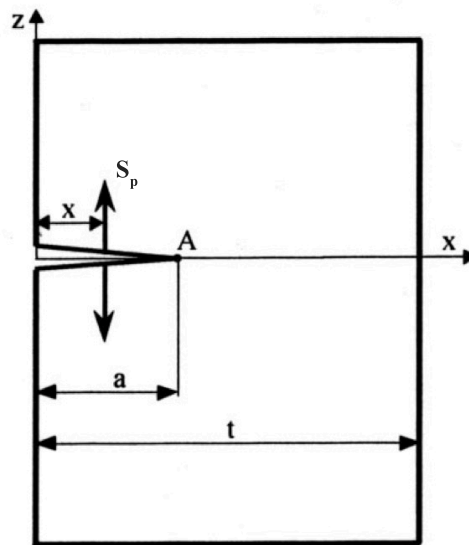


Figure 2.3.: Example of the notation and the coordinate system for the one-dimensional weight function based on [36]

The weight function  $m(x, a)$  can be interpreted as the stress intensity factor  $K_I$  that would result if a pair of splitting forces ( $S_p = 1$ ) were applied to the crack at point  $x$  as shown in figure 2.3. How the weight function method is applied to calculate stress intensity factors will be discussed in detail, when it is applied for fatigue assessment of threaded riser connections in section 5.4.2.

$$m(x, a) = \frac{2S_p}{\sqrt{2\pi(a-x)}} \left[ 1 + M_1 \left(1 - \frac{x}{a}\right)^{\frac{1}{2}} + M_2 \left(1 - \frac{x}{a}\right) + M_3 \left(1 - \frac{x}{a}\right)^{\frac{3}{2}} \right] \quad (2.9)$$

One of the difficulties in using the weight function method is the accurate integration of the stress distribution  $\sigma(x)$  and weight function  $m(x, a)$  [36]. The shape of the stress distribution ahead of a notch and the integration of the product is illustrated in figure 2.4.



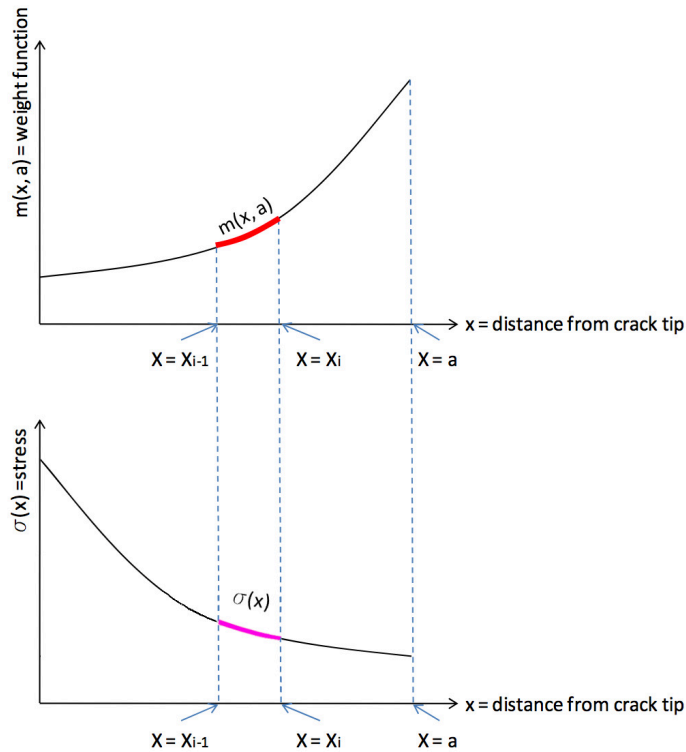


Figure 2.4.: Integration of weight function based on [53]

### 2.3.3. Discussion of the Fracture Mechanic Method

First of all, the advantage of fracture mechanics models is its versatility and accuracy in calculation of remaining lifetime if all input variables are known. Unfortunately, this is also its weakest point. As was shown in the project thesis precedent to this master thesis, uncertainties in crack growth parameter as well as finding an appropriate weight or form function for a given crack shape influences the estimated remaining lifetime significantly [14]. Moreover, LEFM underestimates the severity of a crack if the plastic zone size is large compared to the distance from the crack tip to any boundary of the member [25]. This will further be discussed when assessing the results based on FCG methods.

### 3. Threaded Riser Connections

Threaded connections are used for many applications in oil & gas industry ranging from riser coupling to drillstring or casing connections. They all have in common that they can't be pre-tensioned due to some functional requirements [21], but they are generally pre-loaded due to make-up processes. The preload is introduced by assembling the connection with a certain torque to ensure adequate sealing [54]. Contact forces are then transferred by the threads to prevent separation. Already during the make-up process, high stresses are introduced that can exceed the yield strength at the root of the threads, which act as notches. Moreover, TRCs are subjected to cyclic loading, which leads to high stress concentrations at the root of the LET.

#### 3.1. Connection Details

Since premium riser connections are patented and the available test data are limited to a few cases, a good starting point for analysis are so called standard connections. These connections also build the basis for more advanced connection types. Moreover, the principle fatigue failure mechanism is the same for all TRC. Improvements in fatigue assessment of such standard connections are therefore directly transferable to similar types of threaded connections. In this regard the most common studied connection type is a 1" API Line Pipe connection. This particular connection is a downscaled version of a commonly used TRC and frequently used in testing due to its relatively small size. It consists of truncated triangular threads with a thread angle of  $60^\circ$  and usually a taper of 1/16. Moreover, due to the work by van Wittenberghe [54] it is one of the few connections for which test data and reference FEA results is available.

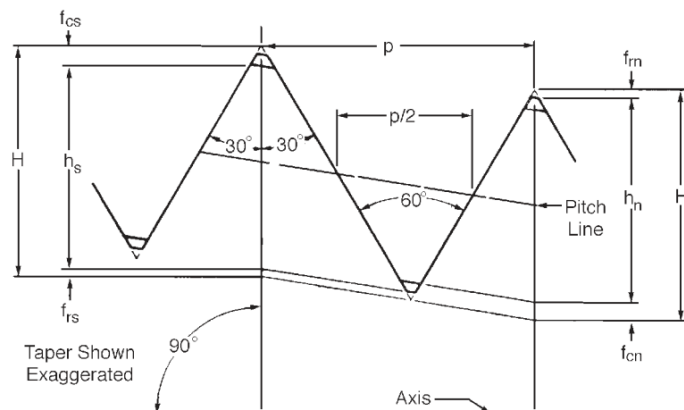


Figure 3.1.: Thread geometry taken from [5].

The 1" API Line Pipe connection has a pin diameter of  $D_p = 33.4$  mm, a wall thickness of

$WT = 3.21$  mm and a fillet radius of  $\rho = 0.05$  mm. The schematic view of the connection is presented in figure 3.2.

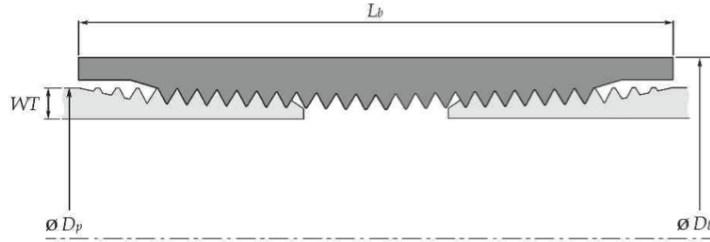


Figure 3.2.: Schematic view of the API Line Pipe connection taken from [54].

### 3.2. Load Condition

Risers are subjected to cyclic wave loads and loads due to relative motion of ships or platforms the riser is connected to. However, it is not part of this thesis to go into detail of the loading. For this purpose it is assumed that a segment of a riser is cyclic loaded in bending. In this case the bending stress  $\sigma_b$  is expressed by an equivalent nominal tensile stress acting on the pipe cross-section outside the threaded segment of the riser. The linear transformation is then given by the following expression by

$$M_b = \frac{\sigma_b \pi (D_o^4 - D_i^4)}{64 \frac{D_o}{2}} \quad , \quad (3.1)$$

with  $M_b$  as the acting bending moment,  $D_o$  as the outer diameter, and  $D_i$  as the inner diameter of the pipe.

As already mentioned in the introduction, the aim of this thesis is to perform fatigue assessment of TRCs based on different methods, which means that no data are needed for the actual loading of the connection. However, it is necessary to do analysis on different alternating load levels to be able to compare the results of the tested methods, but this loading will be an equivalent nominal tensile stress.

## 4. Finite Element Analysis

### 4.1. Introduction

Probably, the most common way for fatigue assessment nowadays is to use finite element analysis in conjunction with a local-stress method such as the peak stress approach, due to its simplicity and close relation to experimental testing [54]. It is the prescribed method in standards, recommended practice and norms like DNV-RP-C203 [24], BS 7608 [17] or ASME B31.3 [6].

This method is based upon calculation of the structural response of a structure by FEA for example. As mentioned earlier, the elastic stress concentration factor  $K_t$  can be calculated from the ratio of maximum local stress and applied nominal stress. Once the stress concentration factor is found for the critical location of a particular structure, it can be used to calculate the lifetime of this structure for every loading condition from a S-N design curve. Based on this procedure it is possible to perform basic fatigue assessment according to standards and regulations. However, previous research projects for instance by Fjeldstad et al. [27], as well as by Härkegård and Halleraker [32] have shown that this approach leads to fairly conservative lifetime estimates for structures with step stress gradients such as TRCs. In this thesis different fatigue assessment methods will therefore be used and compared to the results of the local-stress method.

### 4.2. FE Models

Since the different fatigue assessment methods, that were introduced in chapter 2, require different material properties, different FE models have been created. In this chapter the different models will be introduced and the results of the simulations will be discussed. An important part of the discussion will also be the application of loads including the make-up process. Finally, the FE post-processor LINKpfat, which will be used for one fatigue assessment method, will be introduced in the last section of this chapter.

The 2D axisymmetric elastic-plastic model was the first created model. It will be used for stress-based fatigue assessment by means of the peak stress approach and for a comparison with the FE model of van Wittenberghe [54]. The second and third model are both based on a linear elastic material model, in order to be used for fatigue assessment based on FCG methods. One is also a 2D axisymmetric model, which was created by modifying the first model and the other is a 3D half model. For the FCG analysis based on the own scripts, which will be introduced in chapter 5.4, a 2D axisymmetric model is sufficient, but for the FE post-processor LINKpfat, which will later be introduced, a 3D model is required.

- 2D axisymmetric model with elastic-plastic material model
- 2D axisymmetric model with linear elastic material model
- 3D model with linear elastic material model

The first model to be analysis is the 2D axisymmetric model with elastic-plastic material model. In the subsequent section the model will be presented including general details, meshing, load condition, and make-up process. Although, the loading condition and the make-up process are identical for all models used in this thesis. Afterwards, the analysis of the 2D axisymmetric model will be repeated with linear elastic material model and the last model to be analysis is the 3D model with linear elastic material model. Finally, the FE post-processor LINKpfat will be introduced before the results of all three models are used for fatigue assessment of TRCs in the next chapter.

### 4.3. Axisymmetric Model

Although computing power has increased a lot within the last years, 3D FEA is still very time consuming. It is therefore widely accepted to perform FEA of threaded connections based on 2D axisymmetric models. For instance Cetin [21] and van Wittenberghe [54] have shown that the difference in resulting stress accuracy is negligible. Nevertheless, 3D models are important to verify the results achieved by means of 2D FEA and for crack growth analysis.

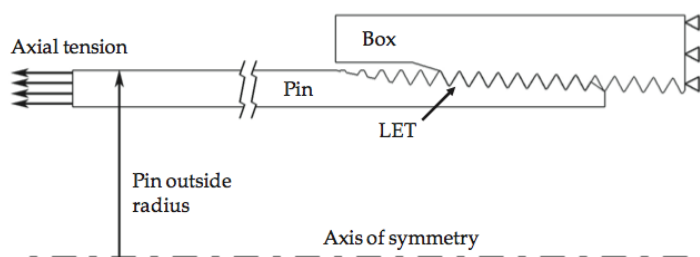


Figure 4.1.: Sketch of the 2D axisymmetric model of the API Line Pipe connection taken from [54].

The model was built according to API 5B - Specification for Threading, Gauging and Thread Inspection of Casing, Tubing, and Line Pipe Threads [5], and consists of a male and a female part also called pin and box. Both were modelled separately and brought into contact before the load is applied. Moreover, the contact description was based on suggestions by van Wittenberghe [54], Cetin [21] and an example case in the Abaqus Example Problems Manual [50].

It is important to mention, that van Wittenberghe's test specimen and FE models does not correspond to the original specification given in API 5B - Specification for Threading, Gauging and Thread Inspection of Casing, Tubing, and Line Pipe Threads [5]. Moreover, no detailed information about the geometry of van Wittenberghe's test specimen and FE models is available. The FE models used in this thesis are therefore build as close as reasonable to the API specification.

Just the run-out region behind the LET, where no contact between the male and female part is, was shortened to be able to use less elements.

The contact definition is based on node to surface interaction, which allows for finite sliding of the members. In this regard the box surface was defined as master surface since it is the more rigid part of the connection. The pin was consequently defined as slave surface. A Coulomb friction model with isotropic friction coefficient of 0.08 was introduced, with the parameter based on tests results by Baragetti et al. and Ferjani et al. [10, 11, 26]. The material properties based on experimental test results of API Grade B steel were adopted from van Wittenberghe [54] and used as input for the multi-linear elastic plastic material description which is presented in figure 4.2 and table 4.1. In order to account for local yielding during make-up and cyclic loading an isotropic hardening rule was used, as recommended by DNV-RP-C203 [24].

Material	Young's modulus [GPa]	Poisson ratio	Yield strength [MPa]	Ultimate tensile stress [MPa]
API Grade B	209.0	0.3	294.0	520.0

Table 4.1.: Material properties of API Grade B as used in FEA

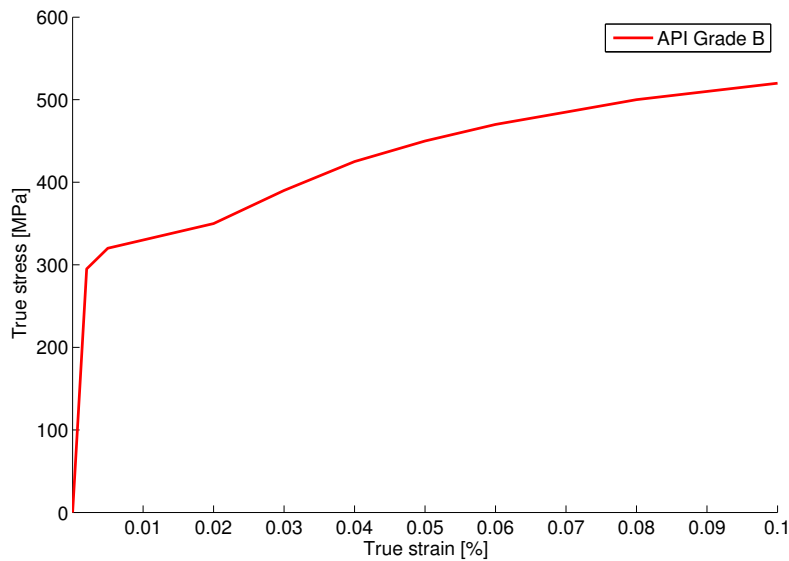


Figure 4.2.: Elastic plastic material data based on tensile test results for API Grade B steel from [54]

### 4.3.1. Mesh

Both parts of the model were meshed with biquadratic axisymmetric quadrilateral elements with reduced integration (CAX8R) [51]. The details of the 2D axisymmetric mesh, as presented in figure 4.3, can be found in table 4.2. Since the pin is the part, which is expected to fail first due to its smaller cross section, the mesh of the pin was additionally refined. For this purpose the thread roots and flanks have been modelled with single biased elements towards the roots, which

can be seen in figure 4.4. Single biased means that the size of the elements is decreasing linearly towards the specified minimum size.

Item		Specification			
Part	Detail	Elements	Maximum size [mm]	Minimum size [mm]	Biased
Pin	Global	12283	0.40	0.4	non
	Flanks	10	0.20	0.20	non
	Flanks on root of LET	37	0.10	0.01	single
	Root of LET	40	0.01	0.0003	single
	Anticipated crack growth path	200	0.10	0.0002	single
Box	Global	3113	0.50	0.50	non
	Flanks	6	0.30	0.30	non

Table 4.2.: Mesh details of 2D axisymmetric model

Additionally, the thread root of the LET (see figure 4.4) has been even more refined, since the stress field at this position is of particular interest for fatigue assessment. In total 15396 elements were used to describe the model with 12283 elements for the pin, 3113 for the box and 1173 for the contact surfaces.

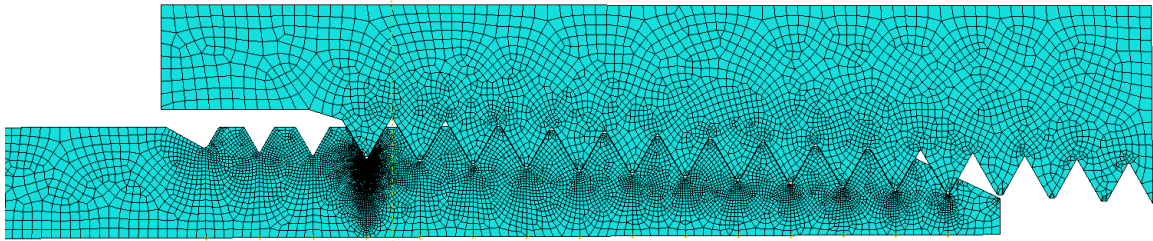


Figure 4.3.: Mesh of the 2D axisymmetric model of the API Line Pipe connection

### 4.3.2. Loading Condition

The actual load situation for offshore equipment is in general non-linear and in service risers are prone to high bending loads. Since it is not possible to apply bending loads in basic axisymmetric models an equivalent tension load according to eq. 3.1 is applied to the free end of the pin. At the other end of the connection is the box clamped to simulate symmetry.

Before the results of the 2D axisymmetric model will be discussed and compared with van Wittenberghes simulations, the simulation of make-up processes in 2D axisymmetric model will be introduced and then applied to the 1" API Line Pipe connection in the subsequent sections.

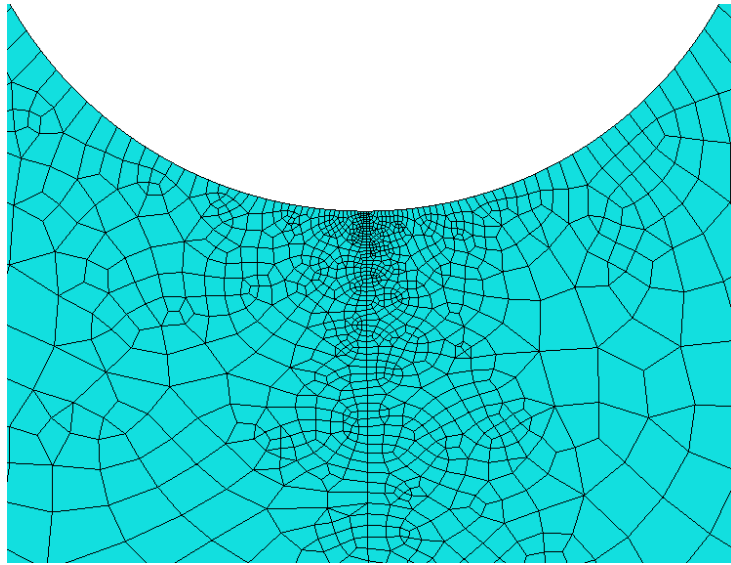


Figure 4.4.: Mesh at the root of the LET of the 2D axisymmetric model

### 4.3.3. Simulation of Make-up Processes

As mentioned earlier in section 4.3, it is common to apply 2D axisymmetric models for FEA of TRCs. However, it is not possible to simulate the make-up turns in a 2D model by rotation. In this section a sophisticated method will be introduced, which allows to simulate the make-up process of TRC in 2D axisymmetric models. First the theory of this method will be introduced, before it is applied to the previously introduced 2D axisymmetric model to simulate the make-up process.

Different ways of modelling make-up processes were developed over the last 20 years. With the development of more advanced FE software also more accurate ways of modelling make-up processes were proposed. Earlier methods were based on applying thermo loads to a strip of thermo-elements [10, 11], pre-tension sections [43], and gap-elements [44]. Recently, a new method was developed for modelling of the assembly process of drilling riser made of aluminium and steel by Santus et al. [44].

During the assembly a torque is imposed to the connection, even after the mating surfaces are already in contact. Since the surfaces are not able to penetrate each other contact pressures arise. By interference the amount of penetration is meant, that would be caused, if the mating surfaces would not block each other. According to Santus et al. [44] two kinds of interference are caused between the male and female part of the connection during assembly of pin and box of drilling riser. Those interferences are:

- a radial interference at the thread root  $I_r$ , thread flanks, and the conical thread-free portion  $I_c$ ;
- an axial interference at the shoulder stop face obtained by imposed rotation during assembly after initial contact at the shoulder stop face  $I_s$ ;



and can be seen in figure 4.5. The radial interference is controlled by geometrical tolerances, which are prescribed in standards for the respective connection type. During assembly, the radial interference changes by imposing an extra rotation after the so-called hand-tight situation is achieved. This is due to the conical shape of the connection [44]. In the literature this effected is often compared with two wedges being forces into each other [54]. Contrary to drilling riser (as seen in figure 4.5), the line pipe connection, used in this thesis, does not include contact shoulders, which simplifies the make-up process significantly, since there will be no axial interference.

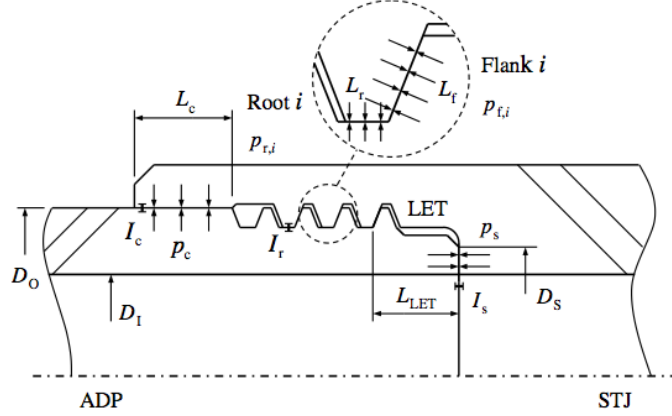


Figure 4.5.: Sketch of a drilling riser connection with interferences and contact pressures taken from Santus et al. [44]

In order to ensure contact at the mating surfaces when the connection is cyclically loaded, a certain torsional strength  $T_s$  of the connection is needed. During assembly, the interference between the mating surfaces cause a contact pressure, which generates a force normal to the contact surfaces. Since the normal forces are applied away from the connection symmetry axis, a torque moment is generated. By integration of all torque contributions the connection torsional strength is obtained from the friction term's contribution and a negative helix term  $T_h$ , which does not need to be considered in this case.

$$T_s = f_s T_1 - T_h \quad , \quad (4.1)$$

where  $T_1$  is defined as the friction torque corresponding to a coefficient of friction  $f_s$  of 1. In order to calculate  $T_1$  the individual torque contributions at all contact surfaces are summed up. For this purpose are the contact pressures at the locations of interference integrated over the contact surfaces ( $p_c$ ,  $p_{r,i}$ ,  $p_{f,i}$ ,  $p_s$ ).

$$T_1 = p_c \pi D_o L_c \frac{D_o}{2} + p_s \frac{\pi}{4} (D_s^2 - D_I^2) \frac{D_s + D_I}{2} + \sum_{i=1}^{n_r} p_{r,i} \pi D_o L_r \frac{D_o}{2} + \sum_{i=1}^{n_f} p_{f,i} \pi D_o L_f \frac{D_o}{2} \quad , \quad (4.2)$$

with  $p_c$  as the contact pressure at the conical thread-free portion,  $p_{r,i}$  as the contact pressure at thread root  $i$ ,  $p_{f,i}$  as the contact pressure at thread flank  $i$ ,  $p_s$  as the contact pressure at the shoulder stop face,  $D_o$  as outer diameter of the male part,  $D_i$  as inner diameter of the male part,

$D_S$  as the outer diameter at the end of the shoulder stop face,  $L_c$  as the contact length at the conical thread-free portion,  $L_r$  as the contact length at the thread roots,  $L_f$  as the contact length at the thread flanks,  $n_r$  as the number of engaged thread root sections, and  $n_f$  as the number of engaged thread flanks. This formulae has been established for riser connection without a taper, such as the one presented in figure 4.5. For other connections with taper, lengths and diameters at the respective thread should be used.

Since the API line pipe connection analysed in this paper has truncated threads, there is no interference at the thread roots. Moreover, due to the in API 5B prescribed clearance between the male and female part along the thread-free surfaces the equation is further simplified. The terms related to the contact pressure at the conical thread-free portion  $p_c$  and the contact pressure at the shoulders  $p_s$  can therefore be neglected. With 24 thread flanks being in the contact the equation is in the present case reduced to.

$$T_1 = \sum_{i=1}^{24} p_{f,i} \pi D_o L_f \frac{D_o}{2} \quad (4.3)$$

Once the friction torque corresponding to a coefficient of friction of 1  $T_1$  is found, the actual torsional strength  $T_s$  can be calculated according to equation 4.1 for a given coefficient of friction  $f_s$ . The advantage of this method is, that the torsional strength  $T_s$  is via equation 4.1 and 4.2 linearly related to the interferences at the contact surfaces. This allows to simulate the connections make-up torque by iteratively increasing the interferences until the torsional strength  $T_s$  equals the aimed make-up torque  $M_{up}$ .

#### 4.3.4. Make-up Process of the 1" API Line Pipe Connection

In this section the previously introduced method shall be applied to simulate the make-up process of the 2D axisymmetric FE model of the 1" API Line Pipe connection. In order to find the friction torque corresponding to a coefficient of friction  $f_s$  of 1 for the 1" API Line Pipe connection, an initial interference in radial direction of pin and box of 0.01 mm, similar to the final interference in figure 4.6, was introduced in the 2D FE model. The contact surfaces are then brought into contact by using the interference fit option of Abaqus, which gradually removes the penetration of mating nodes on the contact surfaces, before the analysis is started. This introduces contact pressure along the 6 elements of each thread flank. Subsequently, a first estimate for the friction torque corresponding to a coefficient of friction of 1  $T_1$  is obtained by integration of the averaged contact pressure distribution according to equation 4.3.

According to Santus et al. the linearity between interferences and contact pressure only holds as long as the local stress does not exceed the yield limit of the material anywhere in the structure, and all mating surfaces remain closed after imposing the inference [44]. From the FE results it follows that for such a small interference this assumption holds well, since there is only a small plastic zone at the thread root of the LET. It is hence possible to relate the friction torque corresponding to a coefficient of friction of 1  $T_1$  directly to the applied interference in radial direction  $I_c$  by the following equation.

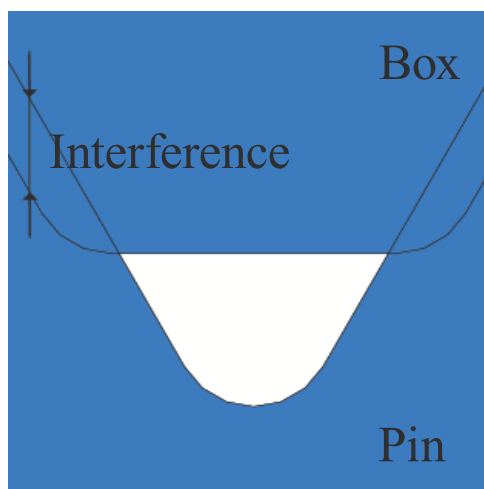


Figure 4.6.: Interference of the contact surfaces for the final configuration

$$T_1 = C_1 I_c \quad , \quad (4.4)$$

where  $C_1$  is a correction factor that can be found by imposing a chosen interference and calculating the friction torque corresponding to a coefficient of friction of 1  $T_1$  from the FE results. Originally,  $I_c$  was defined as the interference at the conical thread-free portion by Santus et al. and is also shown in figure 4.5. However, since there is no interference in the thread-free portion it is used as radial interference in this thesis.

By applying an initial interference in radial direction of pin and box of 0.01 mm, a friction torque corresponding to a coefficient of friction of 1  $T_1$  of 0.3546 kNm was found from the FE results. From 4.4 a correction factor in radial direction  $C_1$  of 35.46 kNm/mm is obtained.

During assembly, a certain make-up torque  $M_{up}$  is applied, which has to be balanced by the torsional strength of the connection  $T_s$ . Based on tabulated values of  $M_{up}$  for the 1" API Line Pipe connection it is hence possible to calculate the interference in radial direction  $I_c$  from equation 4.1 and 4.4 with the previously obtained correction factor  $C_1$ . The interference corresponding to the aimed make-up torque  $M_{up}$  is then implemented in the FE model.

$$M_{up} = T_s \quad (4.5)$$

$$M_{up} = f_s T_1 \quad (4.6)$$

$$M_{up} = f_s C_1 I_c \quad (4.7)$$

API RP 5C1 - Recommended Practice for Care and Use of Casing and Tubing [4] specifies a maximum make-up torque of 190 Nm and an optimal make-up torque of 152 Nm for the 1" API line pipe connection. In order to find the required friction torque corresponding to a coefficient of friction of 1  $T_1$  different sources have been checked for published coefficients of friction  $f_s$  on mating threads. All found papers stated a value of 0.08 [10, 11, 26].

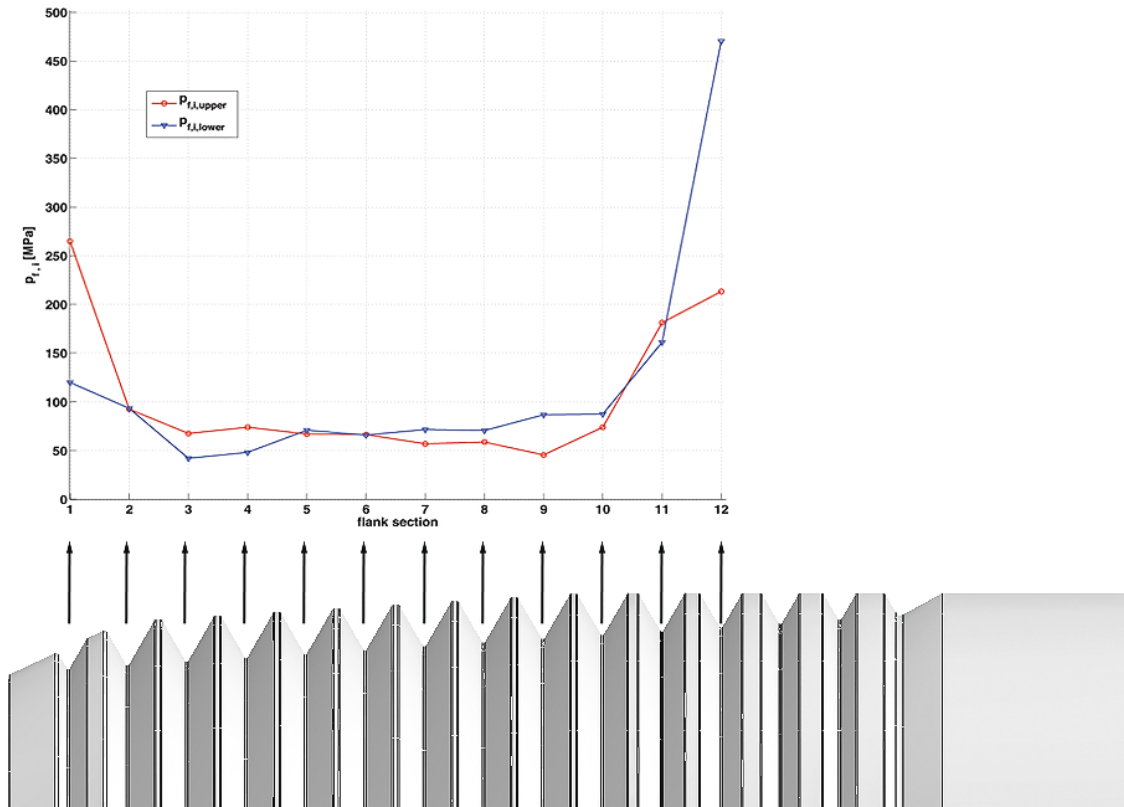


Figure 4.7.: Pressure distribution along the thread flanks

Based on the optimal make-up moment  $M_{up}$  of 152 Nm, the coefficient of friction  $f_s$  of 0.08, and the first estimate of the correction factor  $C_1$  a required interference of 0.054 mm was calculated and implemented in the model. After a second simulation the contact pressure distribution was extracted again, averaged (see figure 4.7) and integrated over the thread flanks.

From equation 4.3 a friction torque corresponding to a coefficient of friction of 1  $T_1$  of 1.69 kNm was calculated, which corresponds to a make-up moment  $M_{up}$  of 135 Nm. This is in fact a bit lower than the aimed make-up moment of 152 Nm. The reason for the deviation from the aimed make-up moment is the severe plasticity at the thread roots. Consequently the linear relation does not hold anymore. This does not imply that an error was made in the computation. Only the relation between the friction torque corresponding to a coefficient of friction of 1  $T_1$  and the applied interference in radial direction  $I_c$  is not linear anymore. It is therefore assumed that the achieved make-up moment is within the specified make-up moment interval for the 1" API line pipe connection.

#### 4.3.5. Results of Model with Elastic-Plastic Material Model

Since the fatigue assessment methods, that will be introduced in chapter 5, require different material models, the simulations of the 2D axisymmetric model have been performed twice. Once with a linear elastic material model for the FCG methods and a second time with a elastic-

plastic material model.

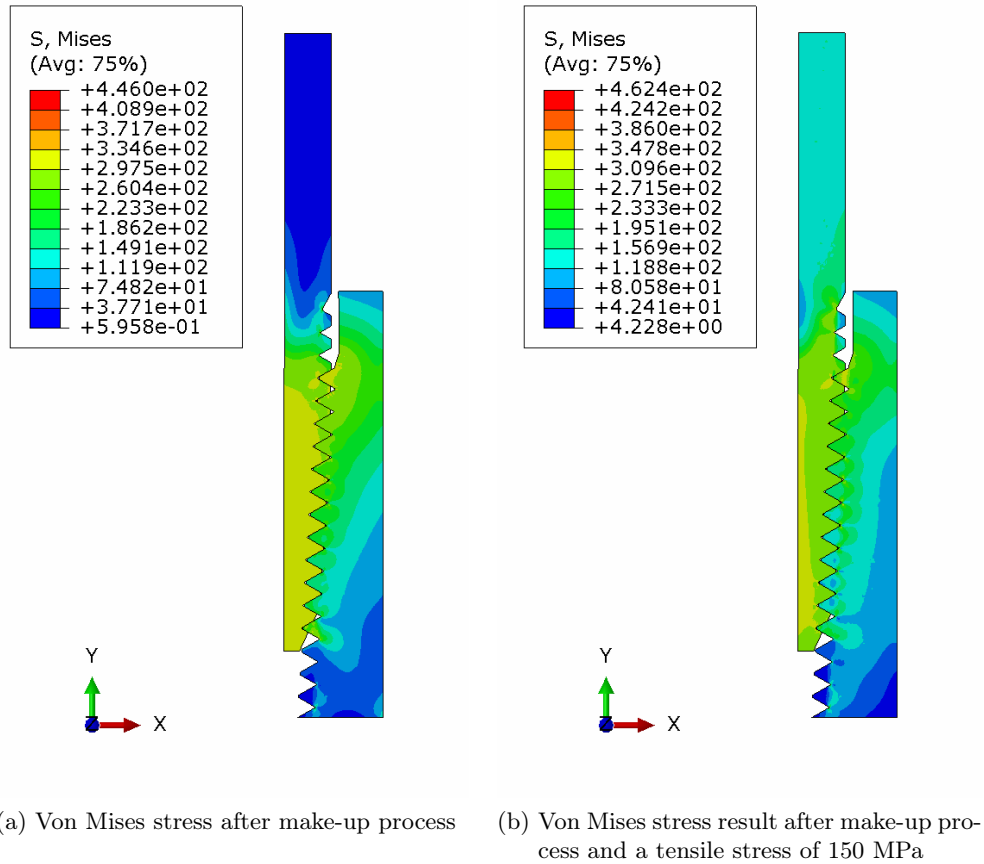


Figure 4.8.: Von Mises stress results of the full 2D axisymmetric model of the 1" API Line Pipe connection with elastic-plastic material model

Due to the different material models used in the simulations, it is practical to divide the result section in two parts. First the results of 2D axisymmetric elastic-plastic model will be compared with the results of van Wittenberghe's FE model. Afterwards the results of the 2D axisymmetric elastic model will shortly be introduced in the subsequent section, before they are discussed and compared with those of the 3D model in detail in section 4.4.2.

The simulations have been performed for different nominal stress amplitudes from  $S_a = 10$  MPa to  $S_a = 80$  with a constant stress ratio  $R = 0.1$ . However, in this section only the stress and strain results for the status after the make-up process and for the status after make-up process and an applied nominal tensile stress of 150 MPa will be presented. The reason is, that only for those stages information from van Wittenberghe are available for comparison. The quantities he mentioned are von Mises stress, axial stress and equivalent plastic strain [54]. The results of the cyclic load cases are not further discussed in this section, but will later be used for fatigue assessment in chapter 5.

As expected the maximum stress response can be found at the root of the LET. The von Mises and axial stress reach 446 MPa and 618 MPa respectively already after the make-up process. Since the yield stress of 294 MPa is exceeded significantly, a distinct plastic zone, with a maximum

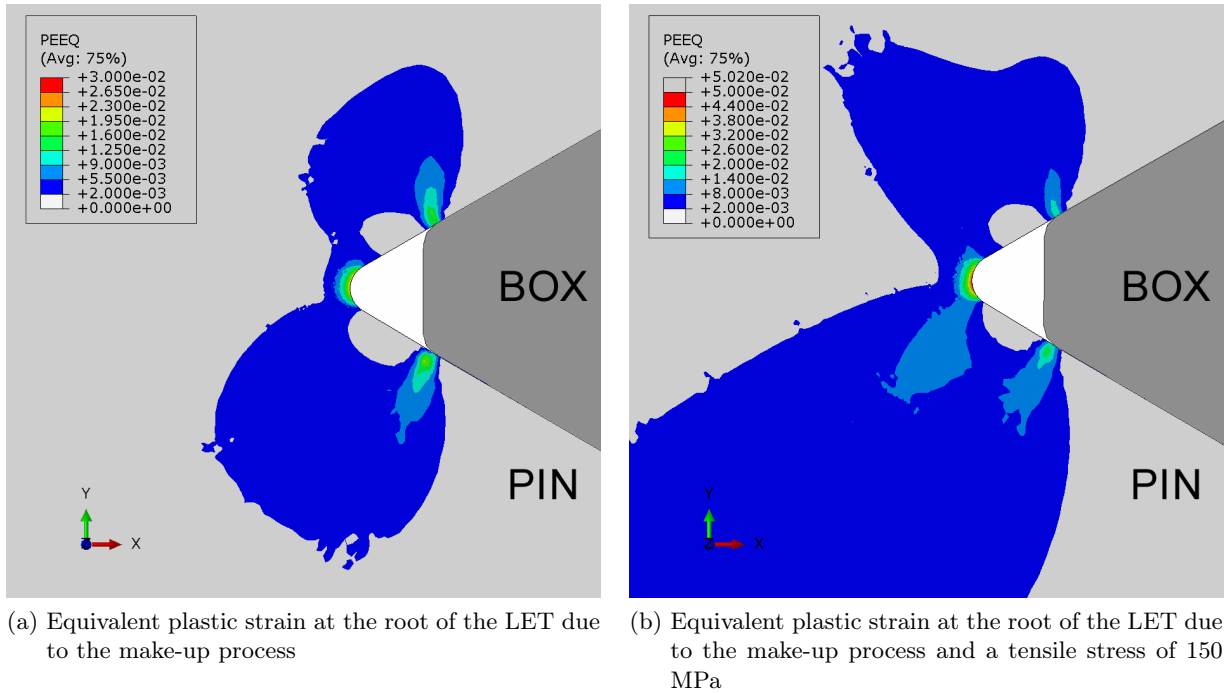


Figure 4.9.: Equivalent plastic strain at the root of the LET of the 2D axisymmetric model of the 1" API Line Pipe connection made of API Grade B steel

equivalent plastic strain of 2.74%, is introduced at the root of the LET. This value rises to approximately 5.02% by applying a nominal tensile stress of 150 MPa, after the make-up process was finished. Both strain fields are presented in figure 4.9a and 4.9b. The equivalent plastic strain is about 50% lower after make-up process and applied tensile stress than in van Wittenberghe's case. However, higher von Mises stresses as well as axial stresses were obtained after make-up process and the additional tensile stress of 150 MPa. This might be due to differences in the material definition in Abaqus.

Compared to the 2D axisymmetric elastic-plastic model from the project thesis and van Wittenberghe's FE model, no separation of the mating surfaces occurred. Both the model from the project thesis as well as van Wittenberghe's model showed a rapid increase of separation for nominal tensile stresses exceeding 100 MPa. However, no gap, between pin and box of the new 2D axisymmetric model, could be detected even for nominal tensile stresses up to 150 MPa. It can therefore be assumed, that modelling the connection with a taper prevents separation of the mating surfaces.

The results are summarized in table 4.3. The complete axial stress and equivalent plastic strain distribution along the anticipated crack growth path after make-up process and a tensile stress of 150 MPa are presented in figure A.1 and A.2 in appendix A.1.

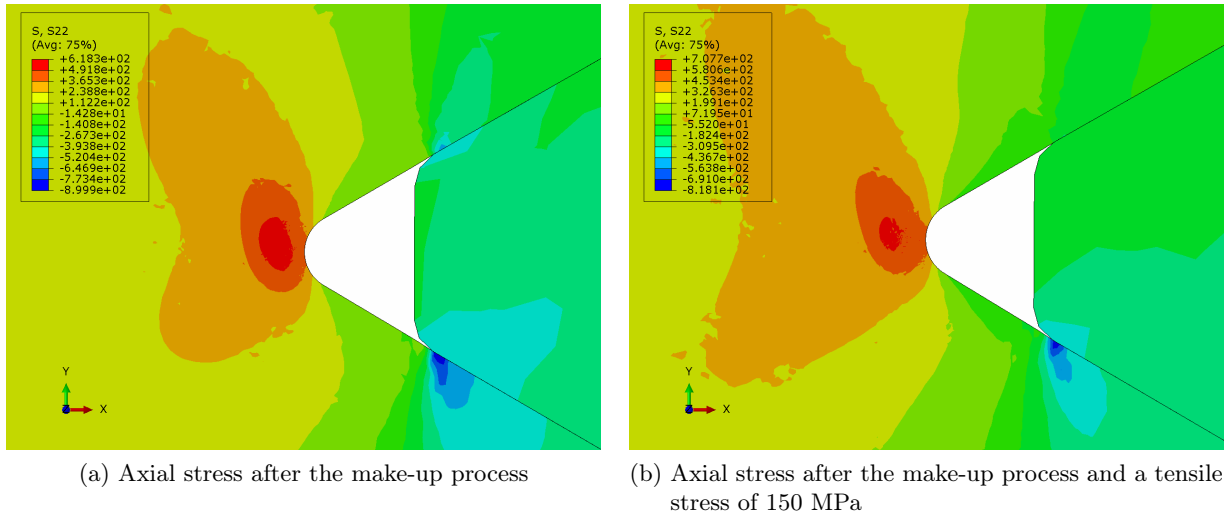


Figure 4.10.: Axial stress results of the 2D axisymmetric elastic-plastic model of the 1" API Line Pipe connection

Quantity	Item		Value		Unit
	after	this thesis	van Wittenberghe		
von Mises stress	make-up	446	-	MPa	
	make-up + 150 MPa	462	425	MPa	
Axial stress	make-up	618	-	MPa	
	make-up + 150 MPa	707	596	MPa	
Equivalent plastic strain	make-up	2.74	0.70	%	
	make-up + 150 MPa	5.02	9.70	%	

Table 4.3.: Comparison of results at the root of the LET from 2D axisymmetric elastic-plastic model with the results of van Wittenberghe

#### 4.3.6. Results of Model with Linear Elastic Material Model

The second model with linear elastic material model was created for the FCG-based methods. Again, simulations have been performed for different stress amplitudes from  $S_a = 10$  MPa to  $S_a = 80$  with a constant stress ratio  $R = 0.1$ , but in this result section only the von Mises and axial stress results for the status after the make-up process and for the status after make-up process and an applied tensile stress of 44.4 MPa will be presented. The later corresponds to the maximum load of a cycle with nominal stress amplitude of  $S_a = 20$  MPa. The results will be discussed in detail in section 4.4.2 when compared to the results of the 3D model.

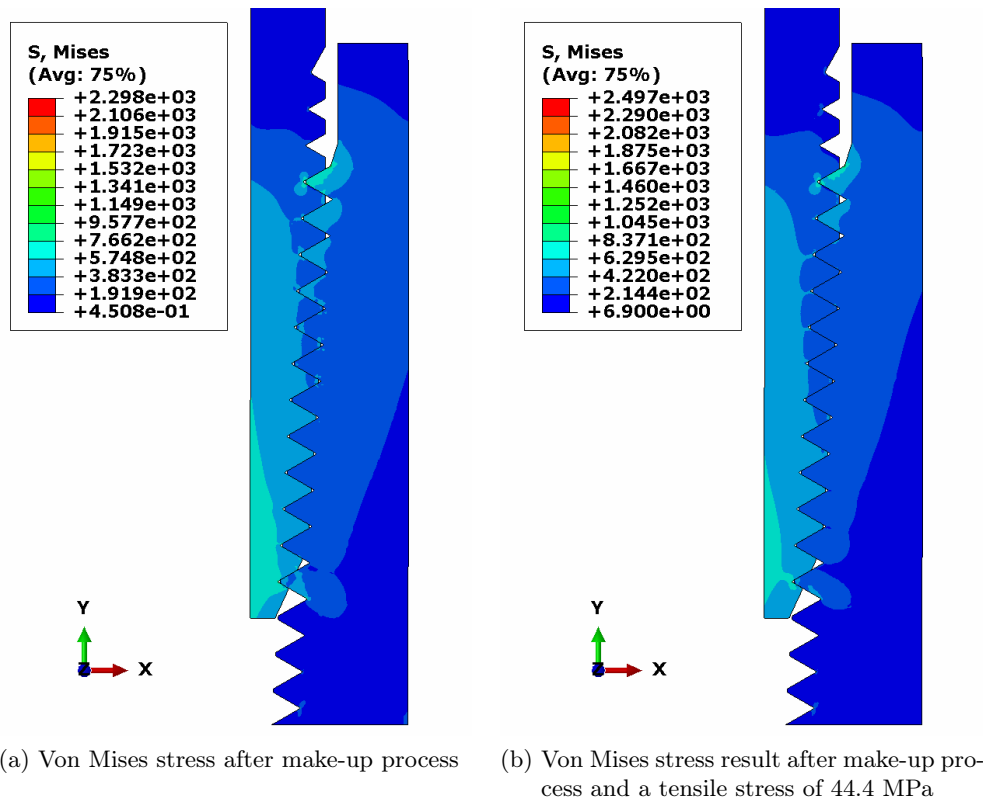


Figure 4.11.: Von Mises stress results of the full 2D axisymmetric elastic model of the 1" API Line Pipe connection

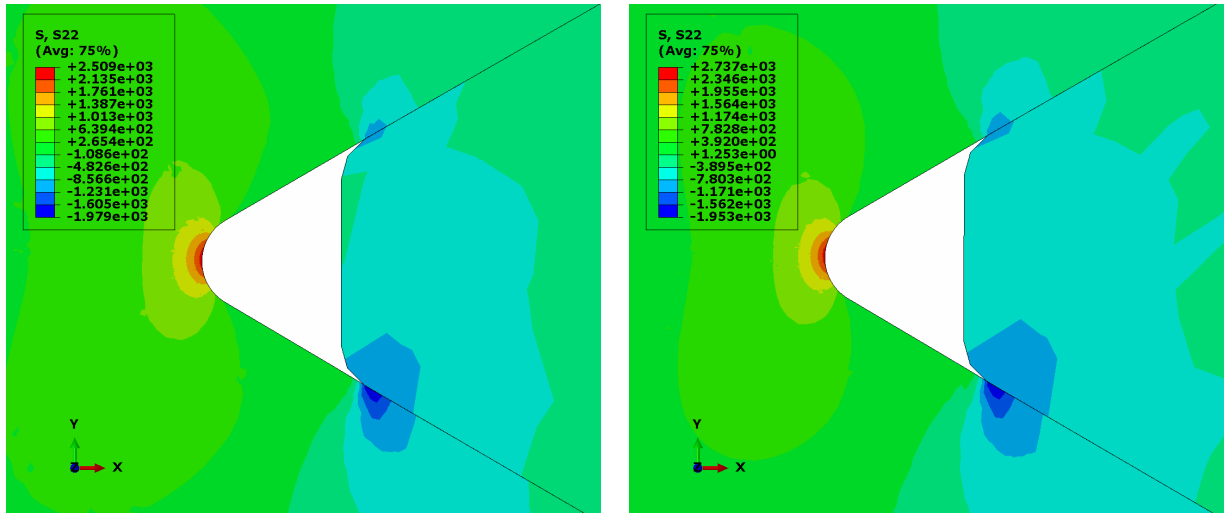
#### 4.4. 3D Model

As earlier mentioned in section 4.3, 2D axisymmetric models are usually used for fatigue assessment of TRCs. For assessment methods such as peak stress methods for example, the shorter calculation and generation time of the model outweighs the better accuracy in many cases. However, some fatigue analysis like the single defect module of the later introduced FE post-processor LINKpfat require 3D models.

Due to the complexity of modelling a full 3D model including the helix angle, it was necessary to simplify the model slightly. For this purpose the generated 3D model neglects the helix angle. Chen and Shih showed that neglecting the helix angle yields a reasonable error of about 10% of the stress distribution with respect to a full 3D model including the helix angle [22]. The 3D model, as presented in figure 4.13a, was constructed by revolving the sketch, which was used for the 2D axisymmetric model, around the symmetry axis to a half model. In order to keep consistent simulations, the same method as introduced in section 4.3.3 was chosen to model the make-up process of the 3D model. For the analysis a linear elastic material model has been used with the Young's modulus and Poisson ratio of table 4.1.

In general, 3D models require more elements than a 2D axisymmetric model to achieve a similar mesh refinement. For this purpose 2 submodels have been established based on the in figure 4.13a





(a) Axial stress after the make-up process

(b) Axial stress after the make-up process and a tensile stress of 44.4 MPa

Figure 4.12.: Axial stress results of the 2D axisymmetric elastic model of the 1" API Line Pipe connection

presented global model. The global model is used to calculate the overall structural response of the connection from simulating a complete load cycle. Timeseries of stress components and displacements for every node along the boundaries of the first submodel are stored and used as input for the first submodel. The first submodel includes the last two threads of the pin and the box and is then used to calculate the stress components and displacements along the boundaries to the last submodel. Due to the decreasing size of the models, the mesh refinement of the models is increased after each step to achieve a mesh for the second submodel that is suitable for fatigue assessment.

In the subsequent section, the 3D FE models will be presented by introducing their meshes, and presenting the achieved results for the same load case as for the 2D axisymmetric elastic model. Finally, the results of both models are compared and the FE post-processor LINKpfat, for which the 3D model was established, will be introduced.

#### 4.4.1. Mesh

The mesh of the 3D model (see figure 4.13b) is very similar to the mesh of the 2D axisymmetric model. Again, smaller elements were used for the pin, but the difference towards the box is less pronounced. The mesh details listed in table 4.4 describe the sketch of the mesh. It is important to mention, that the element length in circumferential direction is constant for all details, since it is specified by the global seed size of the mesh. Since the global model is only used to calculate the overall structural response of the connection a more coarse mesh, compared to the 2D model is appropriate. Moreover, no mesh refinement was applied to the thread roots. However, to improve contact modelling, smaller elements were used for the thread flanks of both parts of the connection.

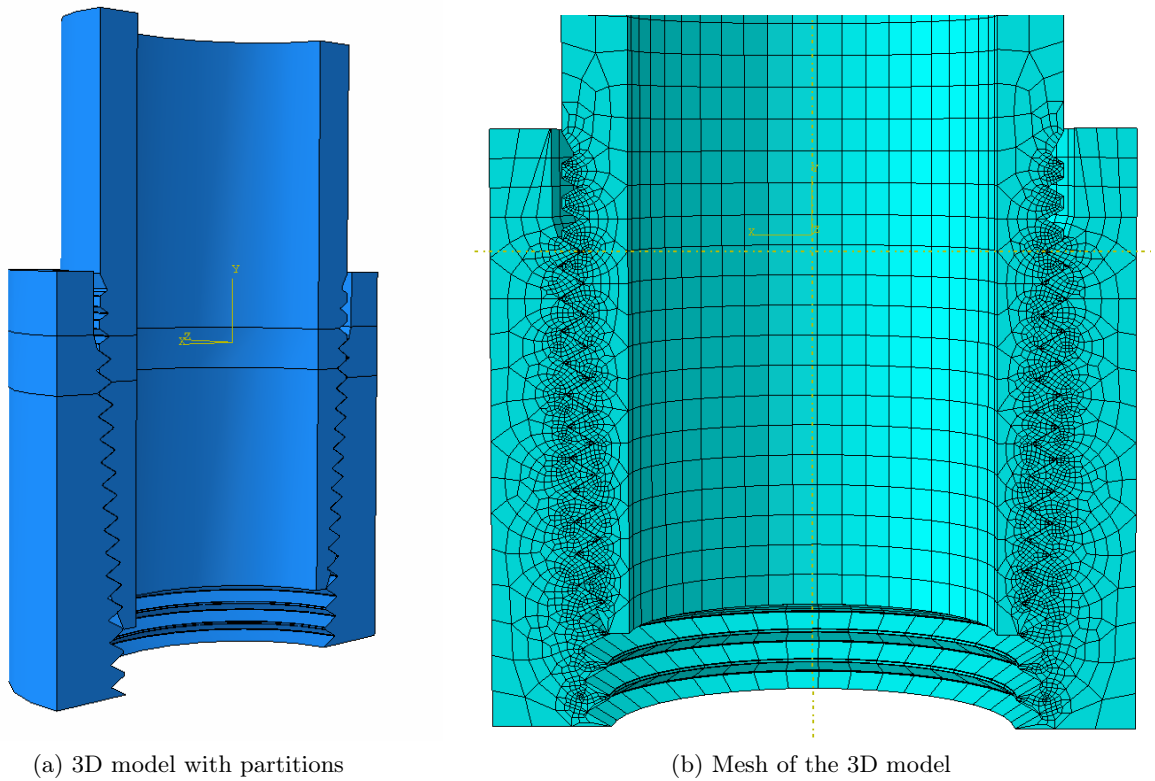


Figure 4.13.: 3D model of the 1" API Line Pipe connection

In order to achieve a sufficient mesh refinement in the crack growth plane, 2 submodels (see figures 4.14 and 4.15) have been generated from the global model. For this purpose both parts of the global model were partitioned into 3 sections, which can also be seen in figure 4.13a. This enables a better transfer of boundary conditions from the global model to the submodel. Since the elements of each section end exactly at the defined partition boundaries, which will also be the boundaries of the submodel, it is easier for the FE software to transfer boundary conditions, since the tolerance between corresponding nodes in both models is very small.

In total the global 3D model consists of 50408 elements, which are divided in 18348 elements for the pin, 19300 elements for the box and 12760 elements for the contact surfaces. Although, the global seed size is bigger for the box, it consists of more elements, due to the larger volume as outer part of the connection.

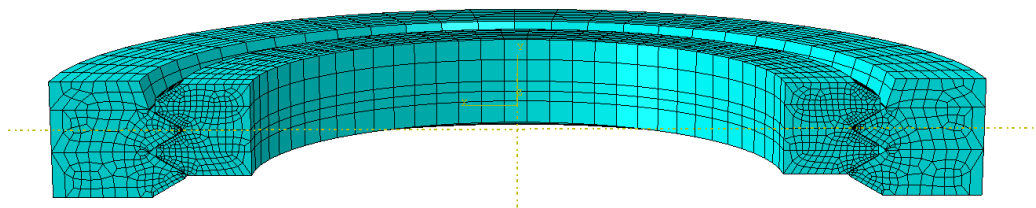


Figure 4.14.: Mesh of the first submodel

Item		Specification			
Part	Detail	Elements	Maximum size [mm]	Minimum size [mm]	Biased
Pin	Global	18348	2.20	2.20	non
	Flanks	5	0.17	0.17	non
	Submodel cut	5	0.67	0.67	non
Box	Global	19300	2.50	2.50	non
	Flanks	4	0.48	0.48	non
	Submodel cut	4	1.19	1.19	non

Table 4.4.: Mesh details of global 3D model

The first submodel as presented in figure 4.14, was then generated by cutting the global models at the specified partition boundaries. It includes the last two threads of the pin and the box. The same principle has then been used for the second submodel (see figures 4.15), which will later be used for fatigue assessment. It is hard to say how many submodels are suitable to achieve a mesh that is fine enough to be used for crack growth analysis. Moreover, it was not clear if the used post-processor LINKpfat, that will be introduced in section 4.5, would be able to handle an even thinner submodel. The decision for two submodels was therefore a trade-off between computation time and accuracy in terms of mesh refinement. By using more than one submodel a severe change in mesh size could be avoided in this case.

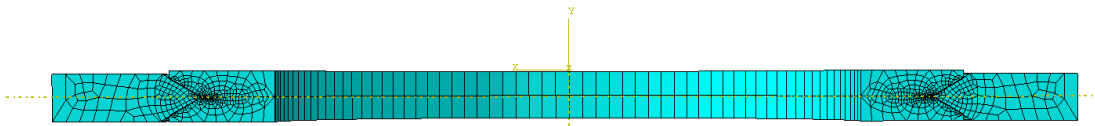


Figure 4.15.: Mesh of the second submodel

Item		Specification			
Part	Detail	Elements	Maximum size [mm]	Minimum size [mm]	Biased
Pin	Global	9438	1.5	1.5	non
	Flanks	10	0.15	0.15	non
	Submodel cut	15	0.30	0.30	non
Box	Global	6440	2.50	2.50	non
	Flanks	6	0.28	0.28	non
	Submodel cut	8	0.59	0.59	non

Table 4.5.: Mesh details of global 1st 3D submodel

Since the first submodel is only an intermediate step towards the final submodel no further mesh refinement was performed. However, the mesh of the second submodel is significantly refined

for the fatigue assessment purpose. The mesh details of the both submodels are summarized in table 4.5 and table 4.6.

Item		Specification			
Part	Detail	Elements	Maximum size [mm]	Minimum size [mm]	Biased
Pin	Global	19220	0.80	0.80	non
	Flanks on root of LET	12	0.12	0.12	non
	Root of LET	8	0.012	0.0025	single
	Anticipated crack growth path	40	0.25	0.012	single
Box	Global	2856	2.00	2.00	non
	Flanks	8	0.21	0.21	non

Table 4.6.: Mesh details of global 2nd 3D submodel

#### 4.4.2. Results of 3D Model

As mentioned earlier in the introduction of the FE models, the 3D model and the 2D axisymmetric elastic model were both built for fatigue assessment based on FCG methods. This section is therefore meant to discuss the results of the 3D model briefly, but also to compare the results of the 3D model and the 2D axisymmetric elastic model. Since the global 3D model and the 1st submodel are the basis for the 2nd submodel, which will be used for fatigue assessment, the results of those two models are not discussed at this point. However, the von Mises stress results can be found in appendix A.2. In figure 4.16 and figure 4.17 are the von Mises and axial stress results of the 2nd submodel presented.

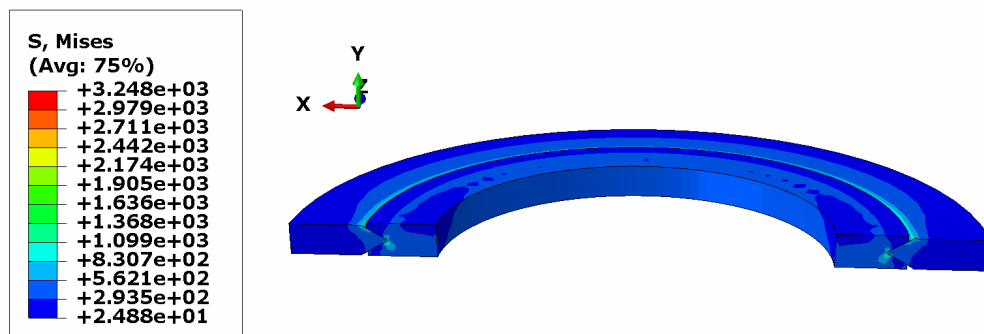


Figure 4.16.: Von Mises stress result after the make-up process and a tensile stress of 44.4 MPa of the 2nd 3D submodel of the 1" API Line Pipe connection with linear elastic material model

After the results of the 2D axisymmetric elastic model have already been briefly presented in chapter 4.3.6, the result of the 2D axisymmetric elastic model and the results of the 2nd 3D submodel will be compared now. For this purpose the maximum stress results of both models

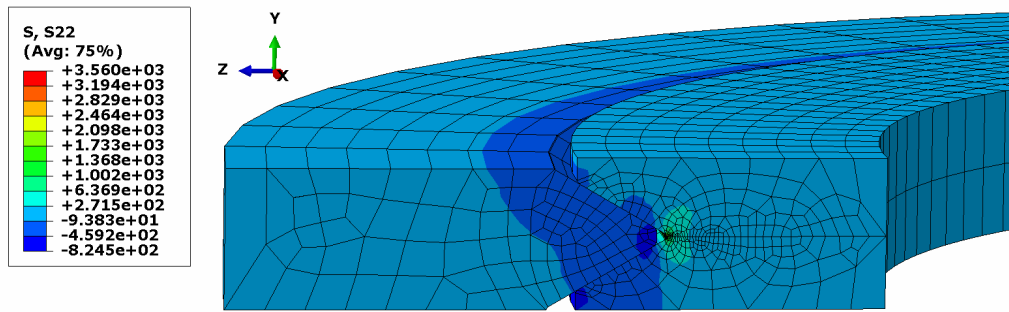


Figure 4.17.: Axial stress result after the make-up process and a tensile stress of 44.4 MPa of the 2nd 3D submodel of the 1" API Line Pipe connection with linear elastic material model

are summarized in table 4.7. The stress results of the 2nd 3D submodel exceed the results of the 2D axisymmetric elastic model after both stages significantly.

However, comparing the maximum values is misleading, since the maximum values of the half model are found at the symmetry plane and not where the crack will later be placed. The reason for the higher stresses along the symmetry plane are the applied boundary conditions along the free surface.

The best way to compare both stress fields is therefore to cut the model into two identical pieces and to inspect the stress results along the cutting plane. This will also be the place where the crack is later placed for the 3D FCG analysis.

		Value		
	Item	2D	3D	Unit
Quantity	after			
von Mises stress	make-up	2298	3048	MPa
	make-up + 44.4 MPa	2497	3248	MPa
Axial stress	make-up	2509	3322	MPa
	make-up + 44.4 MPa	2737	3560	MPa

Table 4.7.: Comparison of results from 2D axisymmetric elastic model with the results of the 2nd 3D submodel

For the comparison it is beneficial to look at the stress field along the anticipated crack growth path of the 2D and 3D model, since the weight function method is based on the integration of the stress field and the weight function along this path. The stress fields of both models have therefore been extracted from the Abaqus output files and partly plotted in figure 4.18. As mentioned earlier, the stresses are highest around the thread roots and since cracks start to grow from there, the axial stress field is only compared up to a distance  $x$  from the thread root of 0.12 mm.

One can notice, that the axial stress field is significantly higher in the 3D case than in the 2D case for the plotted distance. However, already at the end of the plotted interval, the graph of

the 3D axial stress field approaches the one of the 2D case.

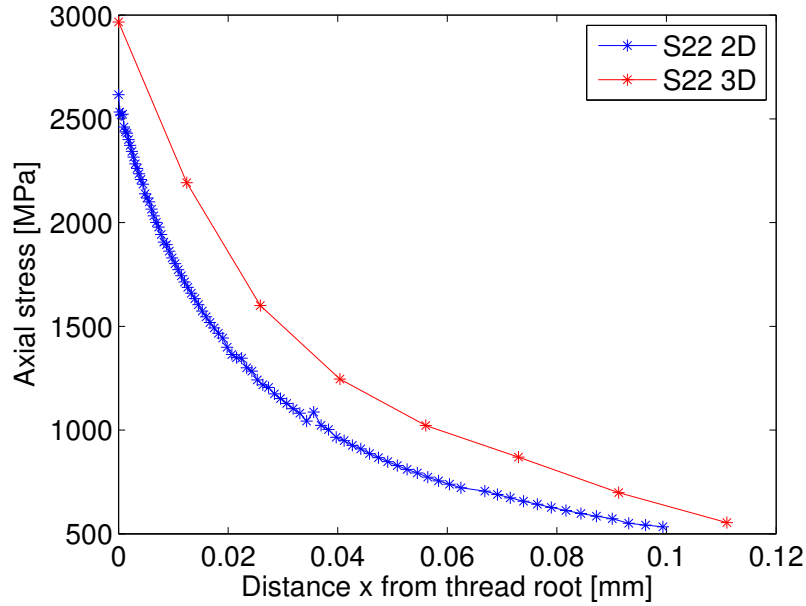


Figure 4.18.: Comparison of 2D and 3D stress field along the anticipated crack growth path for a tensile load of 44.4 MPa and a linear elastic material model

By comparison of the maximum stress result of figure 4.18 and table 4.7 it was found that the node with the maximum stress result does not lie on the anticipated through-thickness crack growth path. This result was expected of the 3D submodel, since the maximum values are found at the symmetry plane of the half model as mentioned before, but not for the 2D axisymmetric model. However, it can be assumed, that the node of maximum stress is one of the nodes surrounding the node at the thread root of the LET, since the axial stress is clearly highest around the thread root of the LET, as can be seen in figure 4.17. Why the through-thickness stress distribution was used will be discussed in detail in chapter 5.4.2.

## 4.5. Finite Element Post-Processor LINKpfat

In this chapter the FE post-processor LINKpfat that will be used for fatigue assessment of TRCs will be introduced. It is capable of performing deterministic as well as probabilistic fatigue assessment based on both stress-based and fracture mechanics methods. An overview of the different modules is given in table 4.8.

Approaches to Fatigue Analysis	Deterministic	Probabilistic
Stress-Based	Local stress	Weakest-Link
Fracture mechanics	Single Defect	Random Defect

Table 4.8.: LINKpfat modules taken from [58]

LINKpfat is capable of handling various types of finite elements from a range of FE programs

like Abaqus, Ansys, or Nastran. From the output files of those FE programs the geometry and stresses are extracted and imported in LINKpfat. It is well suited for fatigue life predictions of notched components containing defects. [58] For further information see the user manual [31] or Wormsen et al. [58]. As earlier mentioned, a validation test of LINKpfat was included in the project thesis precedent to this master thesis [14]. The test will therefore not be repeated at this point. For further information the reader is referred to [14].

# 5. Fatigue Assessment of Threaded Riser Connections

## 5.1. Introduction

In this chapter a number of fatigue assessment methods based on local stress and fracture mechanics methods will be used for fatigue assessment of TRCs. For this purpose an overview of the relevant standards for fatigue assessment of TRCs will first be given, before the selected fatigue assessment methods will be introduced and used to assess the 1" API Line Pipe connection. The last part of this chapter will be a discussion of the results of the selected fatigue assessment methods and a comparison with each other, the available test data from van Wittenberghe, and given design curves.

## 5.2. Overview of relevant standards and criteria

TRCs among other subsea systems are classified in design and operation of subsea production systems - part 7: completion/ workover riser systems of ISO 13628-7 [34], which is identical to API RP 17G [1]. This standard specifies all requirements for the design, analysis, materials, fabrication, testing and operation of subsea completion/ workover (C/WO) riser systems run from a floating vessel. However, only the relevant requirements for fatigue assessment of C/WO riser systems in annex C of ISO 13628-7/ API RP 17G will be presented in this thesis.

In general, fatigue assessment shall be performed at all locations where there is a risk of fatigue crack initiation. The following fatigue assessment methods are permitted by ISO 13628-7/ API RP 17G:

- methods based upon fatigue tests (S-N curves for normally sound connections) and estimation of cumulative damage (Palmgren-Miner rule);
- methods based upon fracture mechanics (fatigue crack growth predictions of flawed components);
- direct experimental approach by fatigue testing of components.

In annex C of ISO 13628-7/ API RP 17G it is specified that fatigue assessment should generally be based upon S-N data, determined by fatigue testing of a representative component and the linear damage hypothesis [34]. For this purpose it is referred to DNV-RP-C203 [24] for fatigue



assessment based on a S-N approach. The fatigue assessment guidelines of DNV-RP-C203 are based on S-N design obtained from experimental test results. Those design curves are obtained by correcting the mean test curve for two-standard-deviations [24], which corresponds to a probability of survival of 97.7%. For unwelded structures like TRCs, DNV S-N curve B1 should be applied [34].

In general, cumulative fatigue damage calculation plays an important role in fatigue design of offshore structures like TRCs. However, since it is not the aim of this thesis to calculate the fatigue damage for a given load spectrum, guidelines for cumulative fatigue damage calculation will not be discussed in this thesis. Instead an overview over the permitted fatigue assessment methods will be given in this section. Since the comparison of the selected methods will later be based purely on established S-N design curves, it is not necessary to look into load analysis.

According to ISO 13628-7/ API RP 17G, fatigue assessment based on fracture mechanics is meant as supplement to S-N data. It is recommended for use in assessment of acceptable defects, evaluation of acceptance criteria for fabrication, and for planning of in-service inspection for fatigue cracks [34]. For guidance regarding fatigue crack analysis, i.e. crack propagation equations, crack growth parameters, crack growth threshold range, stress intensity factor range calculation, etc. API RP 17G [2] refers to BS 7910 [18], API RP 579 [2] and other recognized codes.

The first fatigue assessment method to be considered in this thesis is the peak stress or S-N approach according to DNV-RP-C203 [24]. Thereafter two different FCG-based fatigue assessment from ASME BPVC VIII-3-App. D [6] will be applied to assess the 1" API Line Pipe connection.

### 5.3. Peak Stress Approach

As earlier mentioned, the peak stress is one of the most common methods and prescribed in many standards, due to its simplicity and close relation to experimental testing [54]. In this thesis it will be used in the form described in DNV-RP-C203 [24]. For fatigue assessment of TRCs it is recommended to establish a finite element model with contact surfaces on the threads including non-linear material characteristics, where local yielding during make-up and the first load cycle is accounted for by using an isotropic hardening rule [24].

From the resulting stress range at the root of the LET during the first load cycle the fatigue damage can be calculated by using DNV design curve B1. Since the material surrounding the thread roots undergo local yielding during make-up and loading, it is not possible to calculate the elastic stress concentration factor  $K_t$  by the fraction of the peak stress  $\sigma_{max}$  and the nominal stress  $S$  applied as stated in chapter 2.2.2. Instead load cycles are performed until an elastic shakedown state is achieved, before the axial stress range is measured at the node of maximum stress response. Alternatively, it is permitted to perform linear elastic finite element analysis. However, for this thesis the approach with elastic-plastic material model has been selected.

In figure 5.2 it can be seen, that after pre-stressing due to make-up process and loading up to the maximum nominal stress, unloading happens in elastic regime. Due to problems with the Abaqus output file it was only possible to plot the stress-strain curve for a load cycle with

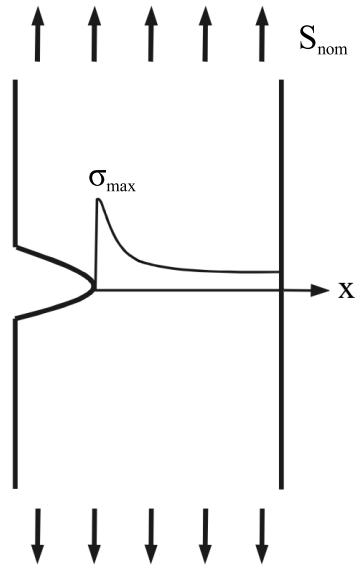


Figure 5.1.: Stress gradient from a notch including peak stress based on [54]

nominal stress amplitude  $S_a = 10$  MPa, since Abaqus exported for several time increments 2 stress and strain values for the node at the root of the LET. It was therefore not possible to check the obtained stress concentration factor for higher nominal stress amplitude  $S_a$ , where an elastic shakedown might occur. The elastic stress concentration factor was therefore found from fraction of maximum stress range  $\Delta\sigma$  at the root of the LET and the applied nominal stress range  $\Delta S = 20$  MPa. From the cyclic stress-strain results a maximum stress range  $\Delta\sigma$  of 103 MPa was obtained, which yields an elastic stress concentration factor  $K_t$  of 5.15.

$$K_t = \frac{\Delta\sigma}{\Delta S}$$

$$K_t = \frac{103}{20}$$

$$K_t = 5.15$$

(5.1)

Unfortunately, reference data for stress concentration factor is rare and the data found, was mainly obtained from FE models with linear elastic material models. Bahai [8] for example found values higher than 30 for an API drillstring connection with similar thread geometry. Unfortunately, the exact value was not given in his paper. Moreover, it is not possible to compare the obtained stress concentration factor to the result from van Wittenberghe, since he calculated  $K_t$  by the fraction of the peak stress  $\sigma_{max}$  and the nominal stress  $S$  only, which yields smaller values of  $K_t$ . However, good overall agreement was achieved with the result of Fjeldstad et al. [27] and Ferjani et al. [26]. Fjeldstad et al. obtained a value of 5.47 for an ACME threaded component made of AISI 8630 steel with the same root radius, but different thread shape [27] and Ferjani et al. obtained a value of 5.6 for and API Drill pipe connection with same thread type, but larger root radius [26].

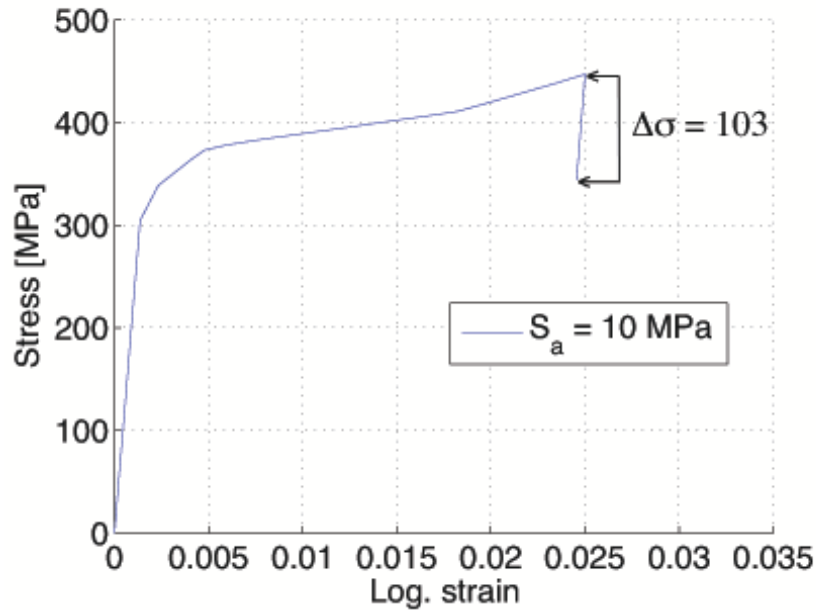


Figure 5.2.: Cyclic stress-strain results at the root of the LET for  $S_a = 10$  MPa and  $R=0.1$

## 5.4. Fracture Mechanics Methods

From the variety of FCG methods that exist nowadays, two methods have been selected to be used for fatigue assessment of TRCs in this thesis. The major criteria for the selection were permission for fatigue assessment of TRCs and that the methods have already been applied for fatigue assessment of TRCs by other authors. Within the scope of this thesis, it would have been interesting to include newer methods like virtual crack closure technique, but this would have required intensive preliminary testing on reference cases. It was therefore focused on methods, which have proven their applicability before.

The two selected methods are both listed as alternative fatigue assessment methods in ASME BPVC VIII-3-App. D [6]. According to the Companion Guide to the ASME Boiler & Pressure Vessel Code, both methods are non-mandatory due to the variety of available FCG-based fatigue assessment methods [35]. The designer is therefore permitted to use alternative methods and stress intensity factor solutions as appropriate [35].

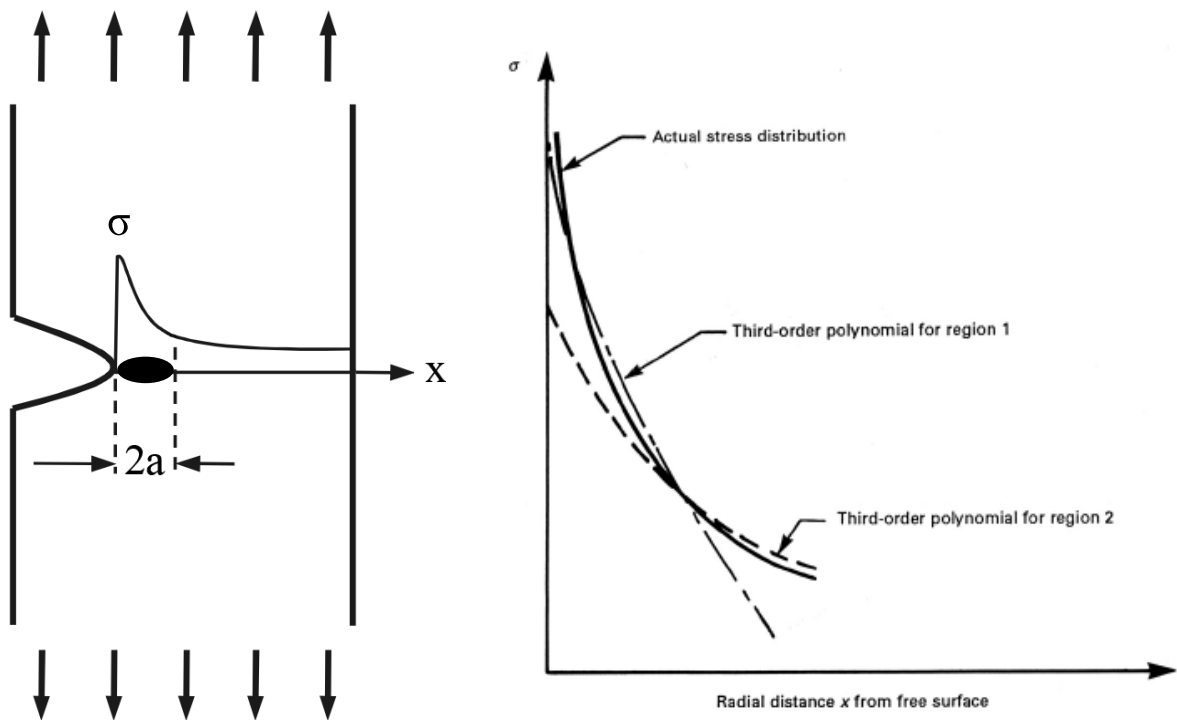
The first method has already been used in the project thesis and is rather straight forward. It was used again, since it yielded promising results. However, due to including the taper of the connection geometry, it was necessary to repeat the calculations for the new FE model. Moreover, the method was extended to include the fatigue crack growth threshold in order to estimate the fatigue limit. The second method is based on the in chapter 2.3.2 introduced weight function theory. However, in ASME BPVC VIII-3-App. D is no specific weight-function solution prescribed. From the available weight function solutions, two different approaches have therefore been selected for fatigue assessment of the 1" API Line Pipe connection. An own Matlab script was written to perform FCG analysis based on weight function theory and a 3D crack growth simulation by means of the FE post-processor LINKpfat has been performed.

The single defect module of LINKpfat has so far not been used for fatigue assessment of TRCs by means of FCG analysis. However, the underlying weight function theory is the same as for the Matlab script and has been applied by different authors before. In the respective section previous projects will be discussed.

First, the three FCG-based approaches will be introduced in this chapter and then the necessary crack growth data and mean stress correction will be discussed in section 5.4.4.

### 5.4.1. ASME Crack Growth Method

The first FCG method, that has already been used in the project thesis [14], is an alternative method prescribed in ASME BPVC VIII-3-App. D [6] for pressure vessels and threaded connections such as in TRC. It assumes an annular flaw at the root of a thread, that will give rise to fatigue crack growth. This method has also been used by van Wittenberghe to confirm observed crack growth rates in 1" API Line Pipe connections [55].



(a) Initial flaw beneath the thread root (b) Polynomial representation of stress distribution taken from [6] based on [54]

Figure 5.3.: Basis of ASME crack growth method

In ASME BPVC VIII-3-App. D [6], the Buchalet-Bamford method [19] is recommended to describe the linear elastic stress distribution, normal to the plane containing the annular flaw, by a third order polynomial. The coefficients  $A_0$ ,  $A_1$ ,  $A_2$ , and  $A_3$  can then be found by a least square fit with  $x$  as the radial distance from the thread root surface.

$$\sigma = A_0 + A_1x + A_2x^2 + A_3x^3 \quad (5.2)$$

The stress intensity factor  $K_I$  corresponding to the stress gradient for one load case is then calculated by

$$K_I = F\sqrt{\pi a} \quad , \quad (5.3)$$

where  $F$  is a modified form function, which combines the stress field via the coefficients of the polynomial fit and 4 magnification factors ( $F_1 - F_4$ ), which describe the crack shape.

$$F = A_0F_1 + \frac{2aA_1xF_2}{\pi} + \frac{a^2A_2xF_3}{2} - \frac{4a^3A_3xF_4}{3\pi} \quad (5.4)$$

It is worth mentioning that in case a single 3rd-order polynomial is not enough to achieve a sufficient fit of the stress field, it is permitted to split the region into several parts for which separated polynomial fits are produced [6]. An example of such a division into two different fits is given in figure 5.3b. For both polynomial fits the stress intensity factor is calculated based on equation 5.3 and to compensate the difference between both stress intensity factors, where the regions join, the difference between them is added to all subsequent values of  $K_I$ . To illustrate this lets assume, that 2 polynomial fits are used, the same way as presented in figure 5.3b. For the first region, the actual stress intensity factor  $K_I(x)$  is based on the fit for the first region. From the point  $p$  on, where both regions join, the stress intensity factor  $K_{I,region2}$  for the second region will be used, but the difference  $\Delta K_{1,2}$  at the joining point will be added. This procedure is also presented in figure 5.4.

$$\begin{aligned} K_I(x) &= K_{I,region1} && \text{for } 0 \leq x < p \\ K_I(x) &= K_{I,region2} + \Delta K_{1,2} && \text{for } x \geq p \end{aligned} \quad (5.5)$$

Based on this procedure the number of cycles to failure has been calculated for 8 combinations of  $S_{max}$  and  $S_{min}$  with a constant stress ratio of  $R = 0.1$  using the 2D axisymmetric model of section 4.3 with 2 sets of polynomials in each case. The first polynomial is fitted to the interval  $0 < x < 0.1$  mm and the 2nd to the rest of the stress field. An example of an insufficient fit of the stress gradient by one polynomial and the improvement by dividing the gradient into two regions is enclosed in the appendix B. The source code, which has been used to find the coefficients of the polynomial fit is enclosed in appendix C.

The corresponding fatigue crack growth has then be calculated using Paris Law for different initial defect sizes  $2a_i$  from 0.01 mm to 0.1 mm at the root of the LET. Those defect sizes are chosen to cover the range of typical flaws in steel pipes, as found in tests by Zhang et al.

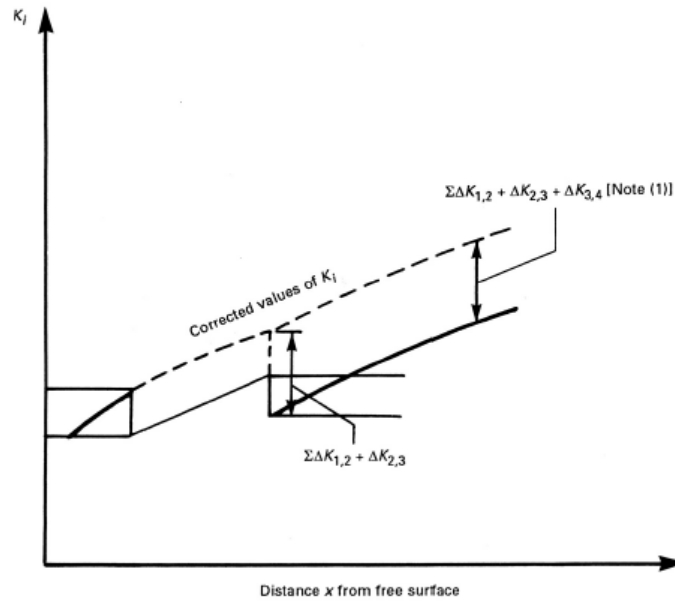


Figure 5.4.: Illustration of the method for correcting  $K_I$  if several polynomial fits are used to describe the stress field taken from [6]

[59]. Additionally, according to Liu et al. [37] a maximum inclusion size of 100 microns seems reasonable.

By numerical integration of Paris Law it is possible to find the number of cycles needed for a crack to grow from the stated initial defect sizes to a through-crack, which is considered as failure of the connection in this case, since the experimental tests of van Wittenberghe were stopped after a leak was detected. In section 5.5.1 S-N curves obtained for different initial defect sizes will be compared to the mean S-N curve from van Wittenberghe for the same connection type, that was established by testing 14 connections under pulsating tension.

#### 5.4.2. Weight Function Method

The second FCG method prescribed in ASME BPVC VIII-3-App. D [6] is based on the universal weight function method, which was introduced in chapter 2.3.2. It can be used for all types of cracks and is therefore suitable for analysing cracks, which originate at the root of threads. Contrary to the weight function form of equation 2.9, the example given in ASME BPVC VIII-3-App. D prescribes a weight function based on the surface opening displacement for assessment of ring-like cracks. No other crack types are mentioned, but it is referred to Bueckner [20] for the universal weight function definition.

Fracture-surface investigation, as seen in figure 5.5, revealed that cracks, which initiate at the roots of threads, grow faster around the circumference than in through-thickness direction. For such complex crack geometries no weight-function has been developed so far. However, different authors have shown, that weight functions for crack geometries like semi-elliptical surface crack yield good results. This is a reasonable assumption, since the crack has the shape of a semi-

elliptical surface crack in the beginning of the crack growth stage [9].

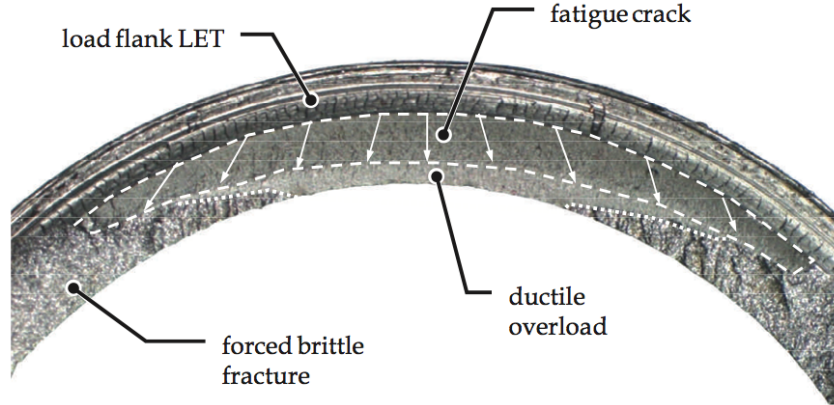


Figure 5.5.: Fracture surface of a fatigue crack in a 1" API Line Pipe connection specimen taken from [54]

The weight function for semi-elliptical surface crack was established by Shen and Glinka in 1991 [46] and later modified by Wang et al. [57] for shallow semi-elliptical surface crack with crack aspect ratio  $(a/c) < 1$ . In the 1990s a series of papers were published about fatigue assessment of TRCs based on fracture mechanics methods. Zhao et al. [60], and Brennan et al. [16] were the first, who used weight function methods for fatigue assessment of TRCs. However, their work was based on older weight function versions, but Bahai [9] was the first to use a weight function in its generalized form.

Based on the general weight function as given in equation 2.9, it is possible to derive weight function solutions for the deepest and the surface point of a semi-elliptical surface crack, since those points are usually associated with the highest and lowest value of the stress intensity factor along the crack front [28].

- Deepest point A

$$m_a(x, a, a/c, a/t) = \frac{2}{\sqrt{2\pi(a-x)}} \left[ 1 + M_{1A} \left(1 - \frac{x}{a}\right)^{\frac{1}{2}} + M_{2A} \left(1 - \frac{x}{a}\right) + M_{3A} \left(1 - \frac{x}{a}\right)^{\frac{3}{2}} \right] \quad (5.6)$$

- Surface point B

$$m_b(x, a, a/c, a/t) = \frac{2}{\sqrt{\pi x}} \left[ 1 + M_{1B} \left(1 - \frac{x}{a}\right)^{\frac{1}{2}} + M_{2B} \left(1 - \frac{x}{a}\right) + M_{3B} \left(1 - \frac{x}{a}\right)^{\frac{3}{2}} \right] \quad (5.7)$$

In order to describe the crack shape by the weight function in depth direction  $m_a$  and along the surface  $m_b$ , it is necessary to find the weight function factors  $M_{1A}$  to  $M_{3B}$  from three reference stress intensity factors solutions for three different stress distributions [28]. This has been done for a number of crack shapes by different authors. For shallow semi-elliptical surface crack with crack aspect ratio  $(a/c) < 1$  Wang et al. [57] found an empirical solution to derived the factors

$M_{1A}$  to  $M_{3B}$  from reference data of Shiratori [47], Gross [30], and Newman and Raju [40]. According to Glinka [28] this solution is better than 3 % when compared with FE data.

For the case of TRCs, the weight function should be used in conjunction with the through-thickness stress distribution at the critical location [9]. Since no exact solution for the stress distribution in a TRC exist, it was further recommended by [46] to approximate the stress field by a series of linear segments, which are fitted to FE results. The analytical solution for the integration of the partial integration for the deepest and the surface point is quite lengthy and will therefore not be stated here. However, it can be found in [28] or [36].

Based on a Matlab script, that was developed for the weight function method, the number of cycles to failure has been calculated for the same 8 combinations of  $S_{max}$  and  $S_{min}$  with a constant stress ratio of  $R = 0.1$  using the stress field that was extracted from the 2D axisymmetric elastic model of section 4.3. The complete source code can be found in appendix C.

Since the ASME FCG method assumes crack growth from an internal flaw beneath the surface with maximum crack size  $2a_i = 0.1$  mm, a semi-elliptical surface crack, that reaches the same depth ( $a_i = 0.1$  mm), was assumed for the weight function method. However, for the actual calculation an effective crack depth  $a_{eff}$ , that includes the depth of the notch  $l$  from which the crack grows, was used according to the recommendation by Kiciak et al. [36].

$$a_{eff} = a + l \quad (5.8)$$

In order to calculate the number of cycles to failure from an initial semi-elliptical surface crack, the following steps are performed by the written Matlab script:

1. Linearization of the through-thickness stress field
2. Calculation of weight function parameter according to formulas from Glinka et al. [28]
3. Calculation of weight function distribution over crack body
4. Calculation of local  $R$ -ratio at deepest and surface point by averaging the  $R$ -ratio over a few increments around the points of interest
5. Integration of product of weight function and linearized stress field in order to calculate stress intensity factor at deepest and surface point for minimum and maximum loading
6. Calculation of stress intensity factor range and mean-stress correction in order to find effective stress intensity factor range
7. Calculation of  $da/dn$  for the crack growth increment
8. Integration of Paris law to find the elapsed number of cycles for the crack growth increment
9. Calculation of crack growth along surface from  $N$  and  $dc/dn$



## 10. Repetition until crack depth reaches wall thickness

Since the local  $R$ -ratio changes during crack growth, it was necessary to implement a mean stress correction to find the effective stress intensity factor range  $\Delta K_{eff}$  for a  $R$ -ratio of 0 by means of Walker's equation [56]. Since no information about the mean-stress sensitivity of the material was found the Walker exponent  $\gamma$  recommended by Dowling has been used [25]. According to him the constant  $\gamma$  for various metals are typically around 0.5 if the  $R$ -ratio for which the stress intensity factor range  $\Delta K$  was calculated is larger than 0.

$$\Delta K_{eff} = \frac{\Delta K}{(1 - R)^{1-\gamma}}, \quad \text{for } R \geq 0 \quad (5.9)$$

For this purpose the local  $R$ -ratio was calculated by averaging the fraction of minimum and maximum local stress around the deepest point of the crack. Since the weight function was developed for a flat plate it is not possible to account for the curved surface. It was therefore necessary to assume, that the thread root acts like a notch in a flat plate. This also means, that the stress field is constant in transverse direction and that the surface point moves in this direction. Consequently, the local  $R$ -ratio at the surface point remains constant throughout the crack growth.

### 5.4.3. LINKpfat Simulations

The third FCG-based method that will be used in this thesis, is based on the in chapter 4.5 introduced FE-postprocessor LINKpfat. For this purpose the single-defect module will be used to simulate crack growth from a semi-elliptical surface crack with the same dimensions, which were used for the previously introduced weight function script. While the weight function script is able to use the stress field of the 2D axisymmetric model directly, a 3D model was required for LINKpfat.

The single-defect module of LINKpfat is based on weight functions as well, but a different one is implemented for semi-elliptical surface crack than the one used by the script of the previous section. However, the process of calculating the crack growth, by means of integrating the product of the stress field in depth direction and the weight function for the respective direction, is similar. For this purpose a local coordinate system is introduced at the origin of the crack [58], which is updated for each crack growth increment, since crack grows in many cases along uneven surface. The line from the crack origin to the deepest point is then meshed with two-noded line elements and the integral of equation 2.9 is solved numerically by means of Gauss-Legendre quadrature [58]. More details about the single defect module can be found in the LINKpfat user manual [31] or Wormsen et al. [58].

For the fatigue assessment the same crack dimensions were used as for the weight function Matlab script. The centre of the initial crack was placed at the intersection of the thread root of the 2nd submodel and the cutting plane, that was used for comparison of the 3D and 3D stress field in section 4.4.2. The orientation of the semi-elliptical surface crack is then found by LINKpfat automatically. An example of the initial crack in the 2nd submodel and the stress distribution

for a nominal tensile stress of 44.4 MPa can be seen in figure 5.6. Since it is very time consuming to perform FEA of the global model, the two submodels and post-processing in LINKpfat only 4 stress amplitudes  $S_a$  from 20 MPa to 80 MPa in 20 MPa steps have been simulated.

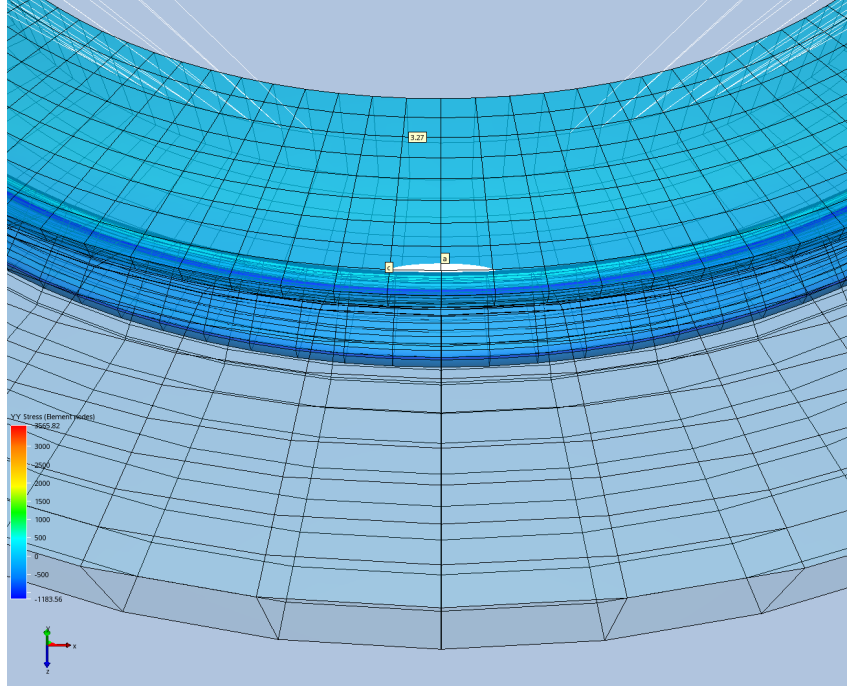


Figure 5.6.: Initial crack at the thread root of the LET in LINKpfat with the axial stress results for a nominal tensile stress of 44.4 MPa

#### 5.4.4. Fatigue Crack Growth Data and Fatigue Limit

In order to be able to perform FCG-based fatigue assessment a number of material parameter are required. These parameter will be introduced in this section. For the crack growth analysis by means of numerical integration of Paris law according to equation 2.7 the crack growth parameter for API Grade B steel are required. Both crack growth parameter  $C$  for  $R = 0.1$  in  $[(\text{mm}/\text{cycle})/(\text{MPa}\sqrt{\text{m}})^m]$  and  $m$  have been adopted from Dale [23] and are summarized in table 5.1. For FCG analysis the parameter  $C$  was mean stress corrected to  $R = 0$  by using Walker's equation [56].

$$C(R = 0) = C(1 - R_C)^{m - m\gamma}, \quad \text{for } R_C \geq 0 \quad (5.10)$$

where  $R_C$  is the stress ratio for which  $C$  was given.

Material	C	m
API Grade B	1.15e-9	2.68

Table 5.1.: Fatigue crack growth parameter based on test results by Dale [23]

For low stress amplitudes, the stress intensity factor approaches a threshold value, below which no crack growth takes place. Unfortunately, no data was found for the fatigue crack growth threshold  $\Delta K_{th}$  of API Grade B steel. A value for the fatigue crack growth threshold was therefore adopted from BS7910 [18], which includes crack growth parameter recommendations for various steel types. In general fatigue crack growth threshold values are highly dependent on environment and  $R$ -ratio. Usually,  $\Delta K_{th}$  is found to increase with decreasing  $R$ -ratio [18]. For unwelded steel components this is taken into account in BS7910 by:

$$\begin{aligned}\Delta K_{th} &= 63 && \text{for } R \geq 0.5 \\ \Delta K_{th} &= 170 - 214R && \text{for } 0 \leq R < 0.5\end{aligned}\tag{5.11}$$

However, the value used in fatigue crack growth analysis should not exceed  $63 \text{ MPa}\sqrt{\text{mm}}$  for assessments of surface-breaking flaws less than 1 mm deep [18]. From literature it is known that fatigue failure of TRCs are usually caused by cracks, which originated at the root of the LET or from surface-breaking flaws beneath the root of the LET [54]. The stress intensity factor threshold  $\Delta K_{th}$  was therefore set to  $63 \text{ MPa}\sqrt{\text{mm}}$  for all fatigue crack growth methods used in this thesis. Moreover, the local  $R$ -ratio close to the crack tip is in case of linear elastic material models higher than 0.5 for all analysed initial cracks.

Based on the stress intensity factor threshold  $\Delta K_{th}$  it is possible to calculate the fatigue limit  $S_A$  for the different FCG-based methods and the given initial defect sizes  $a_i$ . For this purpose the geometry factor  $F$  is calculated from the effective stress intensity factor range  $\Delta K_{eff}$  for a given nominal tensile stress range  $\Delta S$  and the initial crack depth  $a_i$ . In order to obtain the number of cycles  $N$  at which the fatigue limit begins it is then interpolated between the S-N results.

$$F = \frac{\Delta K_{eff}}{\Delta S \sqrt{\pi a_i}}\tag{5.12}$$

$$S_A = \frac{\Delta K_{th}}{2F \sqrt{\pi a_i}}\tag{5.13}$$

## 5.5. Results of Fracture Mechanics Methods

Since the results of the peak stress method have already been discussed, only the results of the three FCG-based methods are presented in this section. The results of the FCG-based methods will be discussed in the same order as the methods have been introduced. Moreover, the results of all methods will afterwards be compared to van Wittenberghe's test results and available design curves.

### 5.5.1. Results of ASME Crack Growth Method

The first FCG-based method that will be discussed is the ASME crack growth method from ASME BPVC VIII-3-App. D [6] for pressure vessels and threaded connections, which was introduced in section 5.4.1. It assumes an annular flaw at the root of a thread, that will give rise to fatigue crack growth.

The fatigue crack growth analysis revealed that the relation between the applied stress amplitude and the number of cycles to failure follows a linear trend in a double-logarithmic diagram. The simulated nominal stress amplitudes  $S_a$  were chosen to cover a wide range of stress amplitudes without reaching into the regions that are governed by separation of the threads and such where the stress amplitude results in axial stresses that are small compared to the stresses introduced by the make-up process.

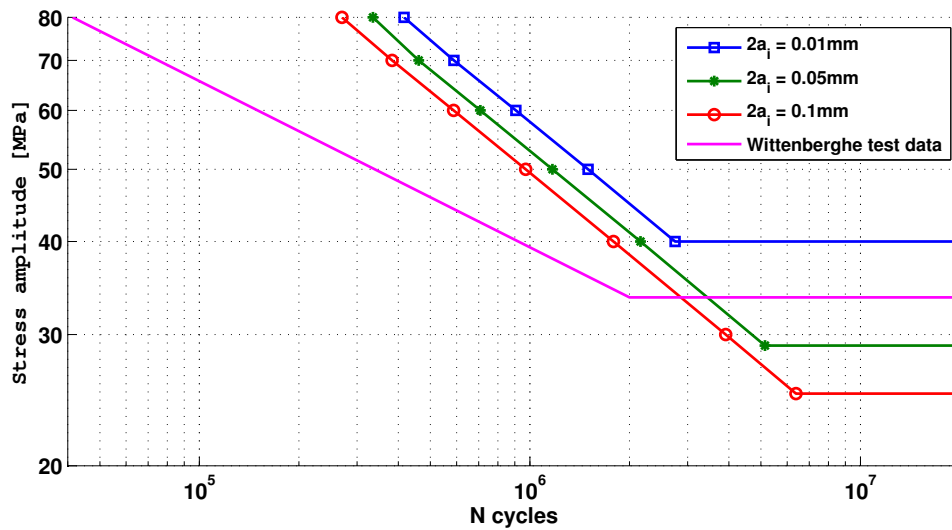


Figure 5.7.: S-N curve for the 1" API Line Pipe connection made of API Grade B steel based on ASME FCG method for 3 different initial crack sizes and  $R=0.1$

As earlier mentioned, the number of cycles to failure has been calculated for 8 combinations of  $S_{max}$  and  $S_{min}$  with a constant stress ratio of  $R = 0.1$  using the 2D axisymmetric model of section 4.3 for three different initial defect sizes  $2a_i$  from 0.01 mm to 0.1 mm at the root of the LET.

For every FCG-based method failure was defined as the occurrence of a through-crack, since the experimental tests by van Wittenberghe were stopped after a leak was detected. The S-N curves, for 1" API Line Pipe connection made of API Grade B steel, that have been obtained for the three different initial defect sizes and the mean S-N curve from van Wittenberghe for the same connection type are presented in figure 5.7. Van Wittenberghe's mean S-N curve is based on testing 14 connections under pulsating tension with a constant stress ratio of  $R = 0.1$ .

All three curves in figure 5.7 fall above the mean curve by van Wittenberghe for the same material and connection type. For a method that shall provide a sufficient level of structural reliability it would have been expected, that the curves fall below the mean curve of van Wittenberghe.

By comparing the new results of the ASME crack growth method with those obtained during the project thesis it becomes obvious, that the difference in connection geometry of van Wittenberghe’s specimen and the geometry as specified in API 5B - Specification for Threading, Gauging and Thread Inspection of Casing, Tubing, and Line Pipe Threads [5], has a significant effect on the predicted lifetime.

A comparison between the new results of the ASME crack growth method with those obtained during the project thesis can be found in figure 5.8. Since a maximum nominal tensile stress of 100 MPa already caused a separation of the mating surfaces in the FE model used in the project thesis, the intervals of nominal tensile stress differ in both cases.

A small deviation from the linear trend of the S-N curves from the project thesis can already be noticed for the highest applied nominal tensile stress amplitude. For nominal tensile stresses exciding 100 MPa separation of the contact surface influences the stress results significantly. Moreover, during the project thesis no fatigue limit was calculated for the ASME method and unfortunately only the S-N results have been stored. It is therefore not possible to compare the estimated fatigue limits of both FE models.

The initial defect has again been placed exactly beneath the thread root of the LET. However, it is still questionable where to place the crack exactly, since this is not mentioned in ASME BPVC VIII-3-App. D [6].

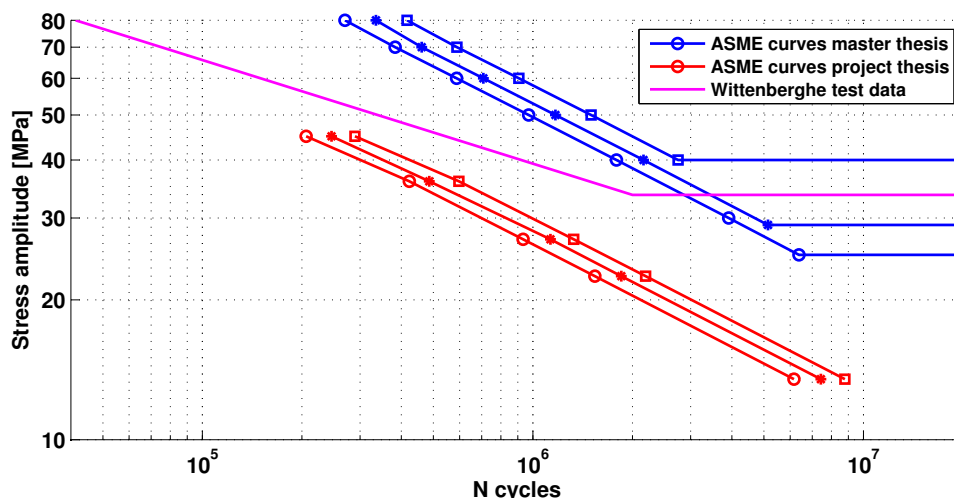


Figure 5.8.: Comparison of the S-N curve for the 1" API Line Pipe connection models from project and master thesis based on the ASME method for 3 different initial crack sizes and R=0.1

From the comparison of the FE model in the project thesis and van Wittenberghe’s FE model with the FE model of the master thesis, it was found that the wall thickness at the root of the LET of the master thesis model is approximately twice as thick as those of the other two models. Since the empirical magnification factors ( $F_1$  to  $F_4$ ) of the ASME crack growth method from ASME BPVC VIII-3-App. D [6] are mainly based on the relative crack depth  $a/t$ , the resulting form function  $F$  is much smaller in case of the master thesis model. The calculated stress intensity factors are consequently smaller for the same defect size in case of the model used in this master thesis. The crack growth is consequently slower in the later model.

The fatigue limit of van Wittenberghe's test specimen was however surprisingly well estimated by the ASME crack growth method. Assuming that the size of the initial defect at the root of the LET, that might cause fatigue failure, lies within the used interval boundaries the corresponding fatigue limit  $S_A$  will vary between 25 MPa and 40 MPa.

### 5.5.2. Results of Weight Function Method

The second FCG-based method that will be discussed is the weight function method as described in ASME BPVC VIII-3-App. D [6] for FCG-based fatigue assessment of pressure vessels and threaded connections. For this method it was assumed that an initial semi-elliptical surface crack e.g. from a machining mark, will give rise to fatigue crack growth at the root of the LET.

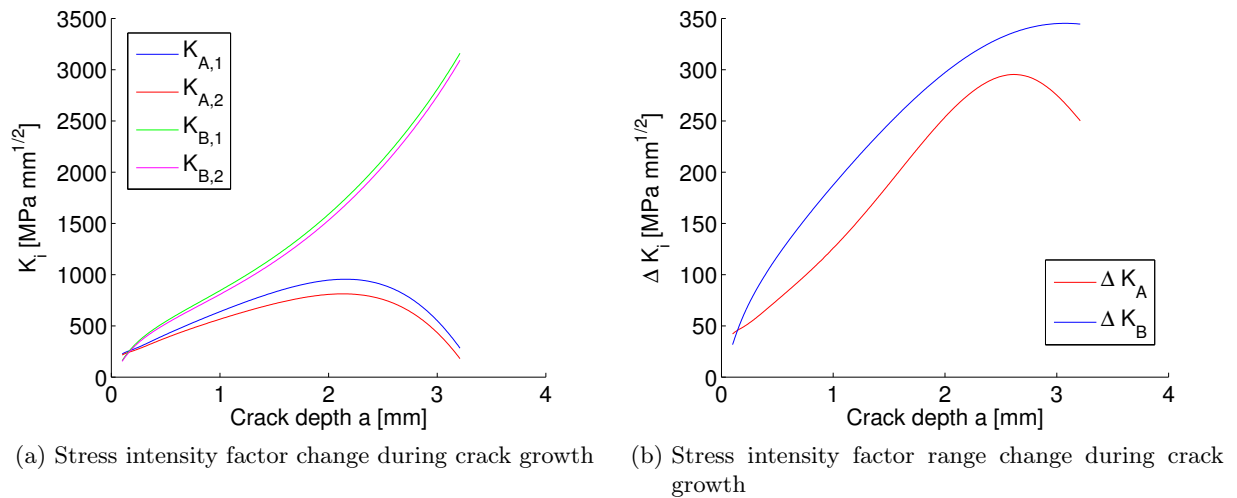


Figure 5.9.: Change of stress intensity factors and stress intensity factor ranges during crack growth from an initial crack with depth  $a_i = 0.1$  mm and nominal tensile stress amplitude  $S_a = 10$  MPa

In order to be able to compare the different fatigue assessment methods later, the same nominal stress amplitudes  $S_a$  from 10 MPa to 80 MPa were chosen for this method. However, only one crack size with initial depth  $a = 0.1$  mm and width  $c = 0.5$  mm was used this time. From plotting the S-N results (see figure 5.13) of the Matlab weight function script it was found that the relation between the applied stress amplitude and the number of cycles to failure follows a nearly linear trend in a double-logarithmic diagram.

In appendix B.2 a summary of important crack growth parameter plotted for 3 different crack growth stages and a nominal tensile stress of 10 MPa can be found. In order to cover different crack growth stages, the results were plotted for  $a = 0.3$  mm (see figure B.4), after reaching a depth of  $a = 1.0$  mm (see figure B.5) and at the end of the crack growth when the crack has grown through the thickness (see figure B.6).

From the subplot of the incremental stress intensity factor of figure B.6, which can also be found in figure 5.9a, a distinct drop of stress intensity factors at the deepest point A can be seen.

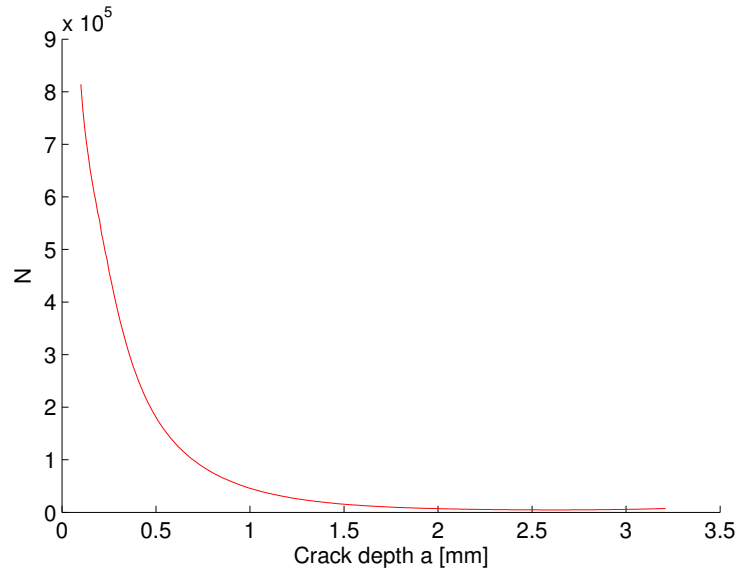


Figure 5.10.: Number of elapsed cycles per crack growth increment of a crack with initial crack depth  $a_i = 0.1$  mm and nominal tensile stress amplitude  $S_a = 10$  MPa

Usually, stress intensity factors increase exponentially with increasing crack depth  $a$ . However, the validity of the applied weight function is limited to  $a/t < 0.8$ . The stress intensity factor ranges (see figure 5.9b) at the deepest point A are therefore underestimated during the late crack growth. But as can be seen from the plot of elapsed number of cycles per increment of figure 5.10, this behaviour is not relevant for the estimated lifetime, since most of the lifetime is spend in the early stage of crack growth.

The shape of the semi-elliptical surface crack plotted after crack growth increment of  $a_{inc} = 0.1$  mm can be found in figure 5.11 and the obtained S-N curve in figure 5.13 together with the results of the LINKpfat simulations and van Wittenberghe's test results.

### 5.5.3. Results of LINKpfat Simulations

Finally, the results of the last FCG-based method will be discussed in this section. While the previous two FCG-based fatigue assessment methods were performed by own scripts, a FE post-processor was used for this part. As has been mentioned earlier, the single-defect module of the FE post-processor LINKpfat is based on a similar weight function approach as the Matlab script of the previous section. The results of both methods will therefore be compared in this section, before a final comparison of all FCG-based methods with the peak stress approach and given design curves will follow in the last section of this chapter.

Again, an initial semi-elliptical surface crack at the root of the LET was assumed for fatigue assessment of the 1" API Line Pipe connection. Since it is very time consuming to perform 3D FEA, only 4 stress amplitudes  $S_a$  ranging from 20 MPa to 80 MPa in 20 MPa steps have been assessed with LINKpfat. Moreover, only one crack size, which was shown in figure 5.6, with initial depth  $a_i = 0.1$  mm and width  $c = 0.5$  mm was used. The final crack shape after fatigue

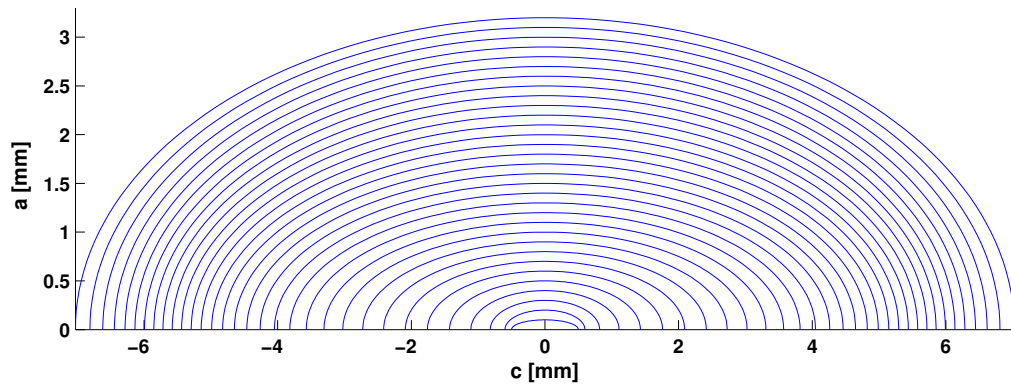


Figure 5.11.: Crack growth stages of a crack with aspect ratio  $a/c = 0.2$  from an initial crack with depth  $a_i = 0.1$  mm and nominal tensile stress amplitude  $S_a = 10$  MPa plotted after crack growth increments  $a_{inc} = 0.1$  mm

crack growth can be seen in figure 5.12.

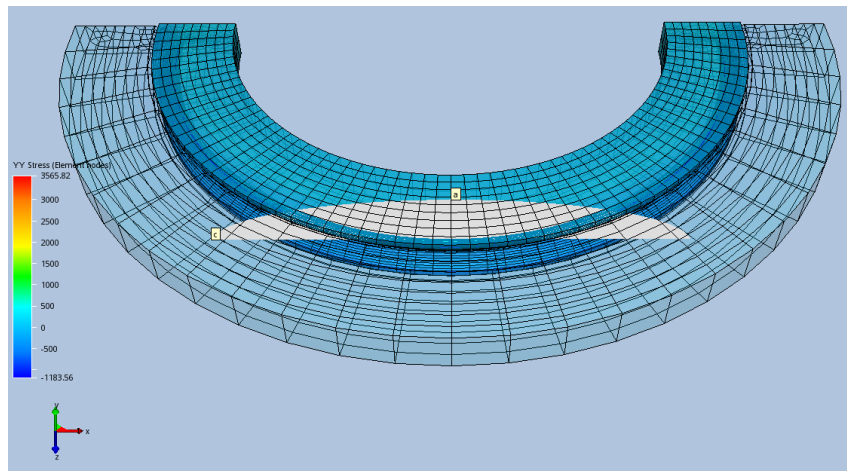


Figure 5.12.: Final crack at the thread root of the LET in LINKpfat with the axial stress results for a nominal tensile stress of 44.4 MPa

From plotting the S-N results it was found that the relation between the applied stress amplitude and the number of cycles to failure follows a nearly linear trend in a double-logarithmic diagram as for the other FCG-based methods. Moreover, the trend of the S-N curve is similar to those obtained from the weight function Matlab script. Both S-N curves are plotted in figure 5.13. The slope of both curves differ significantly from the S-N curve obtained by van Wittenberghe. Moreover, both methods estimate a lower fatigue limit.



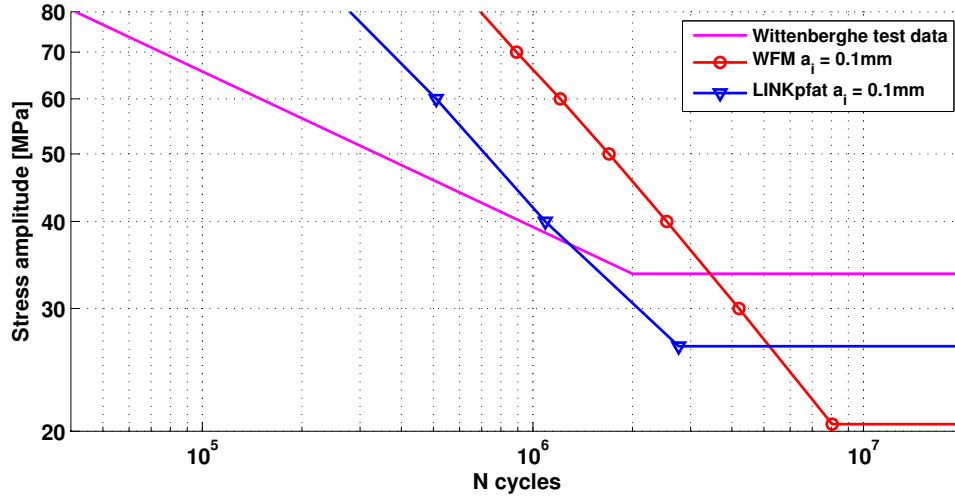


Figure 5.13.: Comparison of the S-N curve for the 1" API Line Pipe connection models based on the results from weight function method and LINKpfat for a crack with initial depth  $a_i = 0.1$  mm and width  $c = 0.5$  mm and  $R=0.1$

## 5.6. Comparison of Fatigue Assessment Methods and Test Data

In the previous sections the S-N curves obtained from the different FCG-based methods have been presented. However, it is also interesting to compare them with each other, the test data by van Wittenberghe, and other design curves like DNV B-curve [24] and ASME design curve for threaded connections [6]. This final section of the fatigue assessment chapter will include a comparison of all obtained S-N curves with the test data. Afterwards the thesis is summarized and conclusions are made.

Since both curves from DNV and ASME are given for fully reversed loading it was necessary to transform the obtained curve for a stress ratio of  $R = 0.1$ . This has been done by means of Smith-Watson-Topper mean stress correction [49], which is a special case of the Walker equation [56] for  $\gamma = 0.5$ , as given below.

$$\begin{aligned}\sigma_{ar} &= \sigma_{max}^{1-\gamma} \sigma_a^\gamma \\ \sigma_{ar} &= \sqrt{\sigma_{max} \sigma_a},\end{aligned}\tag{5.14}$$

with  $\sigma_{ar}$  as equivalent fully-reversed stress amplitude. Unfortunately, no data was found for the given material and connection type regarding mean stress effects. It might therefore be, that other mean stress corrections would yield more accurate results.

For the comparison of the fatigue assessment methods with the test data by van Wittenberghe, it is important to keep in mind, that the FE-models in this thesis do not correspond to the

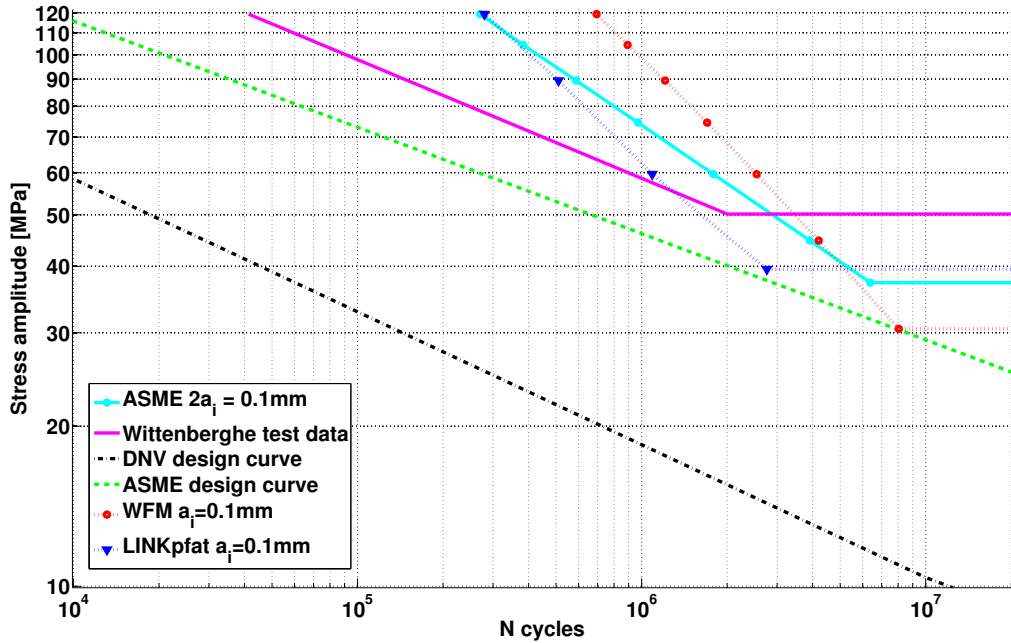


Figure 5.14.: S-N curves for the 1" API Line Pipe connection based on different fatigue assessment methods for  $R = -1$

test specimen used by van Wittenberghe. As has been shown earlier, including the taper in the connection geometry has a significant effect on the structural response and therefore also on the fatigue assessment results.

For lower nominal stress amplitudes, the FCG-based S-N curves are close to the test results and the ASME design curve. This means that both ASME approaches agree well for loads close to the fatigue limit, but also that the FCG-based methods become more unconservative towards higher stress amplitudes. It is interesting to see, that all FCG-based S-N curves yield similar results, compared to the ASME and DNV B1 design curves and the test data. In fact, both curves are considered to give conservative results for structures with step stress gradients such as at the root of a TRC [27]. This result is also supported by van Wittenberghe who came to the conclusion that the ASME design curve is overly conservative [54].

Source	Curve	Stress ratio	Source
DNV-B1 curve for $N < 10^7$	$\log(N) = 15.117 - 4\log(\Delta S)$	-1	[24]
DNV-B1 curve for $N > 10^7$	$\log(N) = 17.146 - 5\log(\Delta S)$	-1	[24]
ASME design curve	$S_a = \frac{1680}{i} N^{-0.2}$	-1	[42]
van Wittenberghe's mean curve	$S_a = 859 N^{-0.2233}$	0.1	[54]

Table 5.2.: S-N curves used for comparison

The plotted DNV design curve was obtained by correcting the B1 design curve from DNV-RP-C203 [24], for the stress concentration factor of 5.15 calculated from FEA of the 2D elastic-plastic model. Another design curve, which is based on test results by Markl in the 1950s for various structures [38], is provided by the ASME codes [42]. For threaded pipe joints a correction factor

$i$  of 2.3 was found, which was later adopted by the ASME B31.3 code for pressure piping [7]. This curve does not assume a fatigue limit. All three design curves are summarized in table 5.2 in their original form including their sources. As can be seen from figure 5.14 the DNV B1 design curve is the most conservative method to assess TRCs. However, none of the applied method seems to cover the test results sufficiently.

## 6. Summary and Conclusion

Threaded connections as found in applications like rigid riser, drillstrings, and workover riser are manufactured with sharp notches. Subjected to loading during offshore operations, those notches lead to high stress concentrations, which increase the risk of fatigue crack initiation significantly. From screwed connections it is known that approximately half of the axial load is carried by the last engaged thread. Consequently, fatigue cracks develop at this location. A common connection type that has been the basis for extensive studies is the API Line Pipe connection, due to its widely availability as standardized connection type [54].

Although, threaded riser connections are studied for several decades now, it is still difficult to predict the lifetime of such components. One reason is that studies and test results are seldom published. However, test results for 1" and 4.5" API Line Pipe connection have lately been published by van Wittenberghe [54].

Fatigue assessment of threaded riser connections is commonly based on a peak stress approach. This is the prescribed method in standards and recommended practices like DNV-RP-C203 [24], BS 7608 [17] or ASME B31.3 [6]. However, it was shown in different research projects that fatigue assessment of threaded riser connections based on this method leads to overly conservative lifetime estimates. The goal of this project was to validate the applicability of other fatigue assessment methods. Methods that seem to yield reasonable results are weakest-link [21], multi-axial fatigue models [26], and fracture mechanics approaches [9, 15, 54].

In an earlier master thesis by Cetin [21], different stress-based methods as well as a weakest-link approach have been studied. To complement his results this thesis has focused mainly on fatigue assessment methods based on fracture mechanics. For this purpose alternative methods based on ASME BPVC VIII-3-App. D [6] have been applied for fatigue assessment of the 1" API Line Pipe connection. The intention was to improve fatigue assessment methods of threaded riser connections. For comparison, fatigue assessment was also performed by means of the peak stress approach.

In this thesis, different fatigue assessment methods were applied, in order to establish S-N design curves for an 1" API Line Pipe connection made of API Grade B steel. For this purpose three different finite element (FE) models were built and analysed with the FE software Abaqus and the FE post-processor LINKpfat. A 2D axisymmetric elastic-plastic model was used for fatigue assessment by means of the peak stress approach, and a 2D axisymmetric elastic model as well as a 3D elastic halfmodel for fatigue assessment by means of fracture mechanics. Unfortunately, no detailed information about the geometry of van Wittenberghe's test specimen and FE models is available. The FE models have therefore been build according to API 5B - Specification for Threading, Gauging and Thread Inspection of Casing, Tubing, and Line Pipe Threads [5].

In the project thesis precedent to this master thesis the taper of the connection was ignored

when modelling the threaded connection, due to van Wittenberghe's findings that the change of taper has a relatively limited effect on the relative thread load at the last engaged thread, but a noticeable one on the thread separation [54]. This finding was supported in this master thesis by applying nominal tensile stress amplitudes that were twice as high as in the project thesis, without a separation of the mating surfaces. Moreover, the cross-section at the last engaged thread is significantly reduced by ignoring the taper and it was proven, that this has caused a more severe stress field in the simplified model. The S-N results of the model used in the project thesis were consequently more conservative.

In general it can be stated that the FE models seem to cover the overall response of the connection well. However, including the taper in the FE models of this thesis, lead to significantly changed stress and strain results at the critical location. Moreover, it is important to mention that the crack took about 20% of the total number of cycles to grow from an initial crack depth of  $a_i = 10$  microns to a length of 50 microns which is equal to the radius of the thread root. The accuracy of the obtained stress field has therefore a significant effect on the estimated lifetime of the component. The mesh of the 2D axisymmetric FE model of this thesis was therefore more refined than the one used in the project thesis.

For the fatigue assessment part of this thesis relevant standards and criteria have been reviewed and a number of fatigue assessment methods have then been selected to be applied to the in chapter 4 introduced FE-models. From the relevant standards two FCG-based and one local stress method have been selected, which are permitted for fatigue assessment of TRCs and that have successfully been applied to assess TRCs before. The chosen methods are the peak stress method as prescribed by DNV-PR-C203 [24], a fracture mechanics approach based on form functions and a more advanced fracture mechanics approach based on weight functions. Both FCG-based methods are specified as alternative fatigue assessment methods in ASME BPVC VIII-3-App. D [6]. Since the method based on weight functions was of particular interest and it is implemented in the FE post-processor LINKpfat, it was applied in two different ways. Beside 3D crack growth analysis by means of the single defect module of LINKpfat, an own Matlab script was written, which calculates the crack growth from a shallow semi-elliptical surface crack.

The first method, which has been applied and compared to van Wittenberghe's test data was the peak stress method. This method is the most common fatigue assessment method for TRCs, due to its simplicity and close relation to experimental testing [54] and is therefore often used for comparison with other methods [27]. However, applied to assess TRCs it usually yields overly conservative results [21]. This expectation was supported by the results presented in section 5.6.

The second applied method, which is an extension of the early form function concept described in section 2.3.1, was the form functions method from ASME BPVC VIII-3-App. D [6]. Based on the stress field of the 2D axisymmetric elastic model, the number of cycles to failure of the male part of the connection has been calculated for three different initial defect sizes ranging from 10 to 100 microns. This has been done for 8 different nominal tensile stresses and a stress-ratio of  $R = 0.1$ . The so obtained values have been plotted in a double-logarithmic diagram of stress amplitude against number of cycles which revealed a linear trend with identical slope for all analysed initial defect sizes.

This method has already been used by van Wittenberghe, but also during the project thesis

precedent to this master thesis. Moreover, the geometry of the FE-model was improved for the master thesis and the results of the project thesis were therefore included in the discussion of the results. It was found, that simplifying the connection by excluding the taper, as done in the project thesis, has a significant effect on the estimated lifetime. As expected the results are also sensitive to the initial defect size, which agrees well with the findings of Nadot [39], who tested the effect of initial defect size on a number of example cases.

The third method is based on FCG simulations by means of weight functions. This method also belongs to the alternative fatigue assessment methods for TRCs in ASME BPVC VIII-3-App. D [6]. For this method two different approaches have been applied. As earlier mentioned, a Matlab script has been written, which is capable of performing FCG simulations based on the stress field from an 2D axisymmetric FE model. However, for the FCG simulations in LINKpfat a 3D model was required. While the Matlab script was used for 8 different nominal tensile stress amplitudes and a stress-ratio of  $R = 0.1$ , only 4 nominal tensile stress amplitudes have been simulated for the 3D model, due to the enormous computational effort of 3D FEA. Moreover, only one initial crack size has been considered, which corresponds to the maximum initial defect size of the form functions method from ASME BPVC VIII-3-App. D [6]. Since both methods are based on the same principle, it has already been expected that the results of both simulation methods coincide. The reason for the small deviation of both methods might be caused by the higher stress results around the root of the LET of the 3D FE model.

During the discussion of the fracture mechanic method in chapter 2 it was mentioned that LEFM underestimates the severity of a crack if the plastic zone size is large compared to the distance from the crack tip to any boundary of the member [25]. The second requirement for the application of LEFM is that the crack depth is large compared to the plastic zone size [13]. If one of the two requirements is violated it is recommended to either use an effective crack correction for the crack length or to apply elastic-plastic fracture mechanics [13]. From the results of the 2D axisymmetric elastic-plastic model in section 4.3.5 it was found, that the first requirement is fulfilled. The plastic zone size is small compared to the wall thickness at the root of the LET as can be seen in figure A.2. However, the same figure indicates that the initial crack depth is approximately of the same order as the plastic zone size. Since the validity range for LEFM is violated only in the beginning of the crack growth stage, I would recommend to use an effective crack correction for the crack depth. Moreover, the application of elastic-plastic fracture mechanics for design purposes is quite complex and an effective crack correction can easier be implemented in existing methods in the future.

Another important uncertainty is the effect of crack growth parameter on the estimated lifetime, it can not be ruled out, that the result might significantly be affected. During the validation of the single defect module of LINKpfat, it was found that the crack growth parameter have a significant result on the estimated lifetime. Moreover, the crack growth parameter for API Grade B steel stated by van Wittenberghe [54], were taken from a source that was not found during the work on this thesis, but the stated values differed significantly from those published by Dale [23].

Recall, that design curves from standards and regulation are usually defined for fully reversed loading ( $R = -1$ ). However, the simulations were performed for pulsating tension. The fatigue assessment results and van Wittenberghe's test data have been transformed to a  $R$ -ratio of -1. This has been done by means of Smith-Watson-Topper's equation. It was shown that the from

FCG-based methods obtained S-N curves are for higher nominal stress amplitudes all above the mean curve that van Wittenberghe obtained by testing of 14 1" API Line Pipe connections. For lower nominal stress amplitudes they cross van Wittenberghe's S-N curve and become conservative. Moreover, the on the weight function theory based methods estimated a lower fatigue limit for the maximum simulated initial defect size. However, for smaller initial defect sizes, as applied for the ASME form function method, fatigue limits have been calculated that surround the by van Wittenberghe proclaimed fatigue limit.

While the FCG-based S-N curves yield all similar results, with a steeper slope than the test results show, the slope of the ASME and DNV B1 design curves are more similar to the test results. However, both curves are more conservative than the FCG-based methods and the test results.

Regarding, the significant effect on estimated lifetime by ignoring the taper of the connection geometry it can be assumed, that a S-N design curve of the 1" API Line Pipe connection, as specified in API 5B - Specification for Threading, Gauging and Thread Inspection of Casing, Tubing, and Line Pipe Threads [5], would be shifted towards longer lifetimes. The ASME and DNV B1 design curves would therefore become even more conservative, while the FCG-based methods would probably fit the data better.

## 7. Suggestion for Future Work

For future work as part of other master thesis for example, I would recommend to validate the chosen 2D modelling procedure, the ASME fracture mechanics approach, the post-processor LINKpfat as well as the Matlab weight function script. By stopping the LINKpfat debugger during calculation it was found, that the local  $R$ -ratio and the stress intensity factor of LINKpfat and the weight function script vary considerably. Since the difference in local  $R$ -ratio has a huge influence on the mean stress correction of the stress intensity factor, this part of the LINKpfat script should be checked. Moreover, the different stress fields of the 2D and 3D model might have had a significant influence on the results of both methods. It would therefore be interesting to do a direct comparison on a number of 3D geometries. The source code of the weight function script and the script for the polynomial fit were therefore included in the appendix of this thesis.

In this thesis only the 1" API Line Pipe connection has been considered, but due to the difference of models, the comparison of the fatigue assessment results with actual test results is flawed. It might therefore be of interest to model another connection for example from FMC for which full-scale results exist.

Moreover, taking into account probabilistic defect size distributions should be considered for future work. So far defects have been considered on a purely deterministic basis, which is reasonable for the performed analysis, but in reality the size and distribution of defects will vary and so the lifetime of a component.



# Bibliography

- [1] American Petroleum Institute. *API RP 17G, Recommended Practice for Design and Operation of Completion/Workover Riser Systems*, 2nd edition, January 2006.
- [2] American Petroleum Institute. *API RP 579, Recommended practice for fitness-for-service*, 2nd edition, May 2007.
- [3] American Petroleum Institute. *API Specification 5L, Specification for Line Pipe*, 44th edition, October 2008.
- [4] American Petroleum Institute. *API RP 5C1, Recommended Practice for Care and Use of Casing and Tubing*, 8th edition, August 2010.
- [5] American Petroleum Institute. *API Specification 5B, Specification for Threading, Gauging and Thread Inspection of Casing, Tubing, and Line Pipe Threads*, 30th edition, June 2010.
- [6] American Society of Mechanical Engineers. *ASME Boiler and Pressure Vessel Code VIII.3-2010*, 2010.
- [7] ASME International. *ASME B31.3-2012 Process Piping*, 9th edition, January 2013.
- [8] H Bahai. A parametric model for axial and bending stress concentration factors in {API} drillstring threaded connectors. *International Journal of Pressure Vessels and Piping*, 78(7):495 – 505, 2001.
- [9] H. Bahai, G. Glinka, and I.I. Esat. Numerical and experimental evaluation of SIF for threaded connectors. *Engineering Fracture Mechanics*, 54(6):835 – 845, 1996.
- [10] S. Baragetti. Effects of taper variation on conical threaded connections load distribution. *Journal of Mechanical Design, Transactions of the ASME*, 124(2):320–329, 2002.
- [11] S. Baragetti and A. Terranova. Effects of over-torque on stress relief in conical threaded connections. *Journal of Mechanical Design, Transactions of the ASME*, 126(2):351–358, 2004.
- [12] O.H. Basquin. The exponential law of endurance tests. In *Proc. American Society for Testing Materials*, volume 10, pages 625–630, 1910.
- [13] S. Berge. Compendium Fatigue and Fracture Design of Marine Structures I - Fracture Design of Welded Structures. Technical Report UK-2006-93, Department of Marine Technology - NTNU Trondheim Norwegian University of Science and Technology, 2006.

- [14] M. Braun. Fatigue assessment of threaded riser connections, December 2013. Project Thesis at Norwegian University of Science and Technology, Department of Marine Technology.
- [15] F.P. Brennan. *Fatigue and Fracture Mechanics Analysis of Threaded Connections*. PhD thesis, University College London, London, Great Britain, September 1992.
- [16] F.P. Brennan and W.D. Dover. Stress intensity factors for threaded connections. *Engineering Fracture Mechanics*, 50(4):545 – 567, 1995.
- [17] British Standards Institution. *Code of practice for Fatigue Design and Assessment of Steel Structures*, BS7608:1993 edition, 1999.
- [18] British Standards Institution. *Guide to methods for assessing the acceptability of flaws in metallic structures*, BS7910:2005 edition, 2007.
- [19] C.B. Buchalet and W.H. Bamford. Stress intensity factor solutions for continuous surface flaws in reactor pressure vessels. *Mechanics of Crack Growth, ASTM STP 590*, pages 385–402, 1976.
- [20] H.F. Bueckner. A novel principle for the computation of stress intensity factor. *Zeitschrift für angewandte Mathematik*, 50:529 – 546, 1970.
- [21] A. Cetin. Fatigue life prediction for threaded riser connections, June 2009. M.Sc. Thesis at Norwegian University of Science and Technology, Department of Engineering Design and Materials.
- [22] J.-J. Chen and Y.-S. Shih. A study of the helical effect on the thread connection by three dimensional finite element analysis. *Nuclear Engineering and Design*, 191(2):109 – 116, 1999.
- [23] B.A. Dale. An experimental investigation of fatigue-crack growth in drillstring tubulars. *SPE Drilling Engineering*, 3(4):356–362, December 1988.
- [24] DET NORSKE VERITAS. *RECOMMENDED PRACTICE DNV-RP-C203 - Fatigue Design of Offshore Steel Structures*, October 2011.
- [25] N.E. Dowling. *Mechanical Behavior of Materials*. Prentice Hall, third edition, 2006.
- [26] M. Ferjani, D. Averbuch, and A. Constantinescu. A computational approach for the fatigue design of threaded connections. *International Journal of Fatigue*, 33(4):610 – 623, 2011.
- [27] A. Fjeldstad, F. Kirkemo, and A. Wormsen. Fatigue assessment of threaded segment specimens based on the weakest link theory. In *Proc. of OMAE2013*, volume 32 of *International Conference on Ocean, Offshore and Arctic Engineering*, Nantes, France, 2013.
- [28] G. Glinka. Development of weight functions and computer integration procedures for calculating stress intensity factors around cracks subjected to complex stress fields, March 1996. Report for Analytical Services & Materials Inc.

- [29] G. Glinka and G. Shen. Universal features of weight functions for cracks in mode I. *Engineering Fracture Mechanics*, 40(6):1135–1146, 1991.
- [30] B. Gross and J.E. Srawley. Plane strain crack toughness testing of high strength metallic materials. *ASTM STP*, 410, 1966.
- [31] PFAT Group. *PFAT - User's Guide and Manual*, 2012.
- [32] G. Härkegård and G. Halleraker. Assessment of methods for prediction of notch and size effects at the fatigue limit based on test data by Böhm and Magin. *International Journal of Fatigue*, 32(10):1701 – 1709, 2010.
- [33] T.H. Hill, P.V. Seshadri, and K.S. Durham. A unified approach to drillstem-failure prevention. *SPE Drilling Engineering*, 7(4):254–260, December 1992.
- [34] International Organization for Standardization. *ISO 13628-7:2005, Petroleum and natural gas industries - Design and operation of subsea production systems - Part 7: Completion/-workover riser systems*, January 2005.
- [35] J.R. Sims Jr. *Section VIII, Division 3 - Alternative Rules for Construction of High-Pressure Vessels*, volume 2, chapter 23. ASME Press, 2006.
- [36] A. Kiciak, G. Glinka, and D.J. Burns. Calculation of stress intensity factors and crack opening displacements for cracks subjected to complex stress fields. *Journal of Pressure Vessel Technology*, 125(3):260 – 266, 2003.
- [37] Z. Liu and K. Cai. Title unknown. *Iron and Steel*, 35(2):64–69, 2000. in Chinese.
- [38] A.R.C. Markl. Piping flexibility analysis. *Trans. ASME*, 77:419–441, 1955.
- [39] Y. Nadot. Propagation lifetime from the surface and internal defects in the ultra high cycle fatigue regime. *The Open Materials Science Journal*, 2:35 – 39, 2008.
- [40] I.S. Raju and J.C. Newman Jr. Stress-intensity factors for a wide range of semi-elliptical surface cracks in finite-thickness plates. *Engineering Fracture Mechanics*, 11:817–829, 1979.
- [41] J.R. Rice. Some remarks on elastic crack-tip stress fields. *Int. J. Solids Struct.*, 8(6):751–758, 1972.
- [42] E.C. Rodabaugh. Comparisons of ASME-code fatigue-evaluation methods for nuclear Class 1 piping with Class 2 or 3 piping. Technical Report NUREG /CR-3243, U.S. Nuclear Regulatory Commission, 1983.
- [43] B.M. Salihu. *Stress analysis of drillstring threaded connections*. PhD thesis, Cranfield University, Bedfordshire, UK, November 2011.
- [44] C. Santus, L. Bertini, M. Beghini, A. Merlo, and A. Baryshnikov. Torsional strength com-

parison between two assembling techniques for aluminium drill pipe to steel tool joint connection. *International Journal of Pressure Vessels and Piping*, 86(2-3):177 – 186, 2009.

- [45] J. Schijve. *Fatigue of structures and materials*. Springer-Verlag, Wiesbaden, second edition, 2009.
- [46] G. Shen and G. Glinka. Weight functions for a surface semi-elliptical crack in a finite thickness plate. *Theoretical and Applied Fracture Mechanics*, 15(2):247 – 255, 1991.
- [47] M. Shiratori, T. Miyoshi, and K. Tanikawa. Analysis of stress intensity factors for surface cracks subjected to arbitrarily distributed surface stress. *Trans. JSME*, 52:390–398, 1986.
- [48] Y. Shoji and T. Sawa. Stress concentration at the root of a bolt thread. In *ASME Proceedings Computer Technology and Bolted Joints*, volume 2 of *ASME 2010 Pressure Vessels and Piping Conference*, pages 427–432, 2010.
- [49] K.N. Smith, P. Watson, and T.H. Topper. A stress-strain function for the fatigue of metals. *Journal of Materials*, 5(4):767 – 778, 1970.
- [50] Dassault Systèmes. *Abaqus 6.11 - Example Problems Manual*, 2011.
- [51] Dassault Systèmes. *Abaqus 6.12 - Abaqus/CAE User's Manual*, 2012.
- [52] Technitube Röhrenwerke GmbH. *High Quality tubular products and accessories*, December 2008.
- [53] W. Tsutsui. Prediction of fatigue crack growth retardation due to tensile overload using two-parameter approach, June 2008. M.Sc. Thesis at Western Michigan University.
- [54] J. Van Wittenberghe. *Experimental Analysis and Modelling of the Fatigue Behaviour of Threaded Pipe Connections*. PhD thesis, Ghent University, Gent, Belgium, November 2011.
- [55] J. Van Wittenberghe, P. De Baets, and W. De Waele. Fatigue crack growth behavior of threaded pipe couplings. In *Proc. of the ASME Pressure Vessel and Piping Conference 2011*, volume 1, pages 1033 – 1039, 2011.
- [56] K. Walker. The effect of stress ratio during crack propagation and fatigue for 2024-T3 and 7075-T6 aluminum. In *Effects of Environment and Complex Load History on Fatigue Life*, volume ASTM STP 462, pages 1–14. American Society for Testing and Materials, West Conshohocken, PA, 1970.
- [57] X. Wang and S.B. Lambert. Stress intensity factors for low aspect ratio semi-elliptical surface cracks in finite-thickness plates subjected to nonuniform stresses. *Engineering Fracture Mechanics*, 51(4):517–532, 1995.
- [58] A. Wormsen, A. Fjeldstad, and G. Härkegård. A post-processor for fatigue crack growth analysis based on a finite element stress field. *Computer Methods in Applied Mechanics and Engineering*, 197(6):834 – 845, 2008.

- [59] L. Zhang and B.G. Thomas. Inclusions in continuous casting of steel. In *Proc. of XXIV National Steelmaking Symposium*, volume 24 of *National Steelmaking Symposium*, pages 138–183, Morelia, Mexico, 2003.
- [60] H. Zhao, Z.-B. Kuang, and Z.-H. Li. Stress-intensity factor for a semi-elliptical surface crack at the thread root of a screwed-pipe joint. *Computers & Structures*, 59(3):419 – 424, 1996.

## A. FE results

### A.1. Results of axisymmetric model with elastic-plastic material model

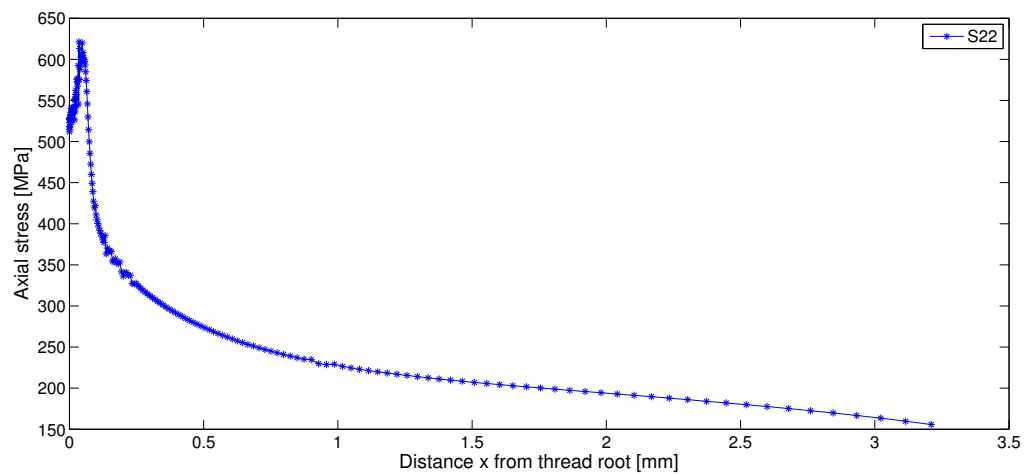


Figure A.1.: Axial stress distribution of the 2D axisymmetric model of the API Line Pipe connection from the root of the LET for a tensile stress of 150 MPa

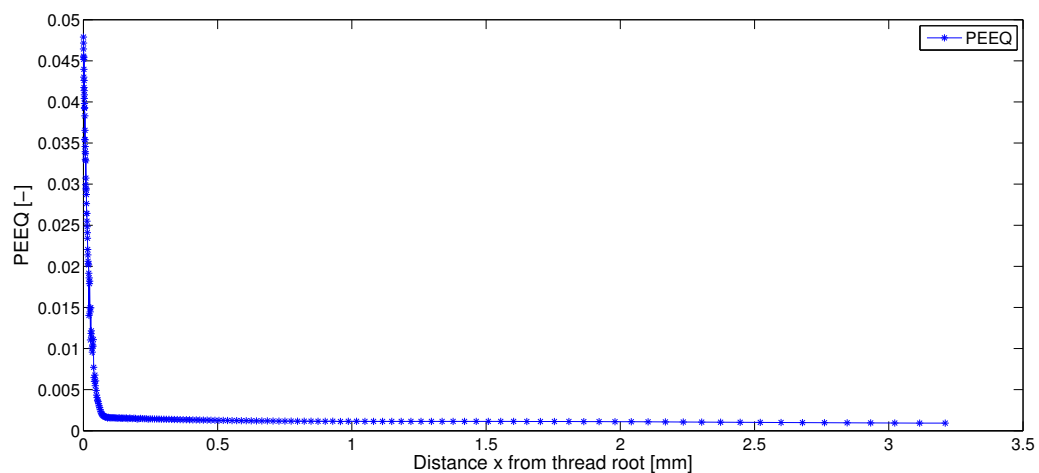


Figure A.2.: Equivalent strain distribution of the 2D axisymmetric model of the API Line Pipe connection from the root of the LET for a tensile stress of 150 MPa

## A.2. Results of 3D model

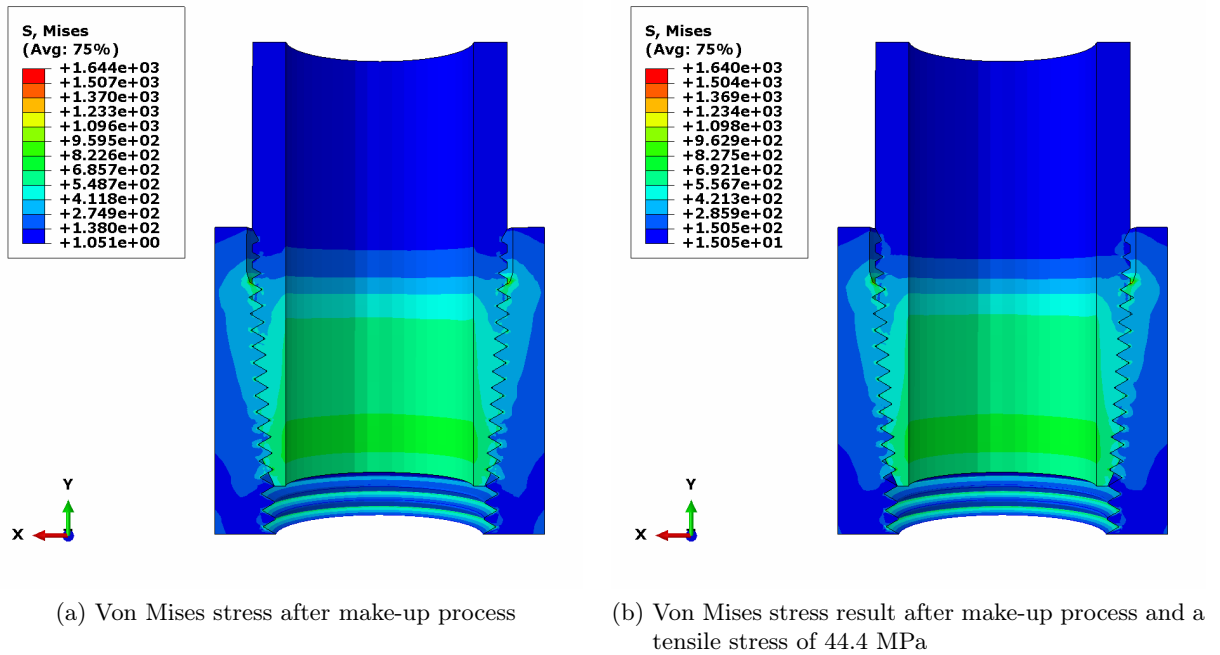


Figure A.3.: Von Mises stress results of the full 3D model of the 1" API Line Pipe connection with linear elastic material model

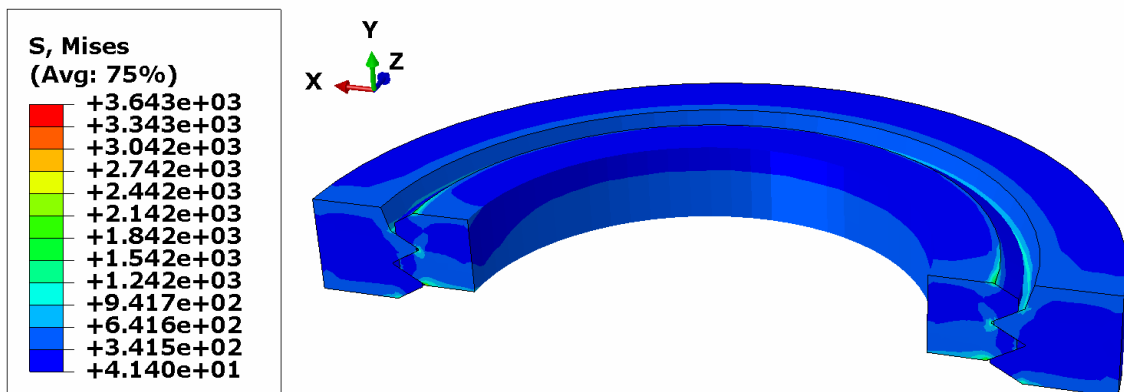


Figure A.4.: Von Mises stress results of the 1st 3D submodel of the 1" API Line Pipe connection with linear elastic material model

## B. Fatigue crack growth calculation

### B.1. Polinomial fitting of stress field

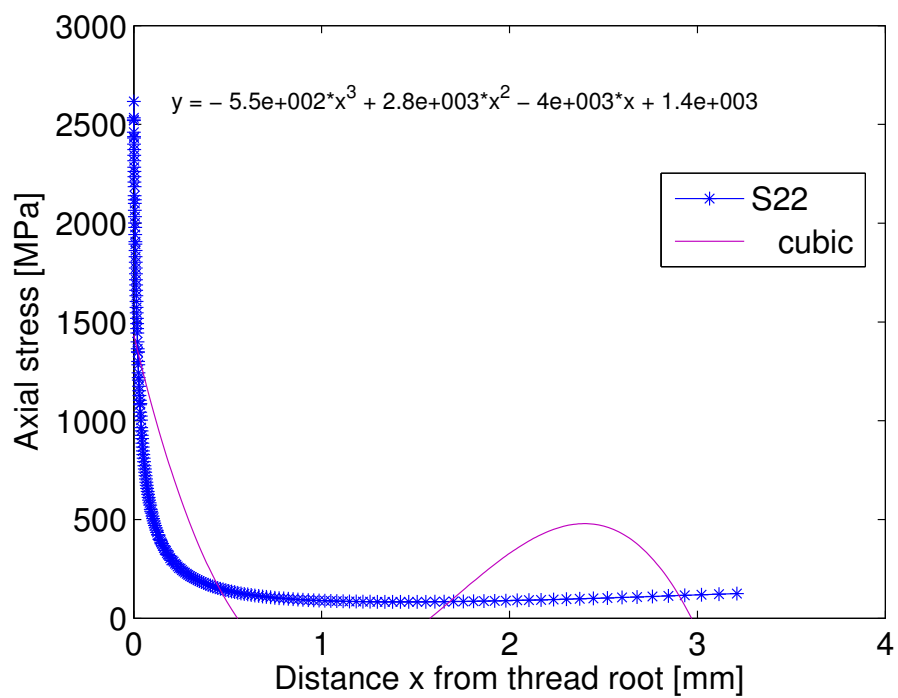


Figure B.1.: Total axial stress distribution from the root of the LET for a tensile stress of 44.4 MPa with 3rd order polinomial fit



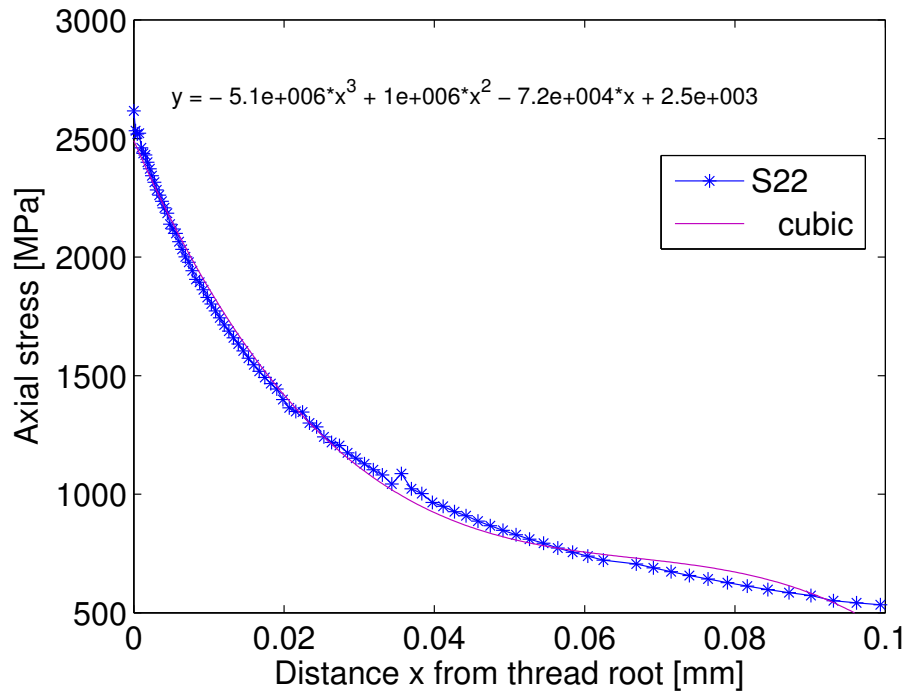


Figure B.2.: Part 1 of the axial stress distribution from the root of the LET for a tensile stress of 44.4 MPa

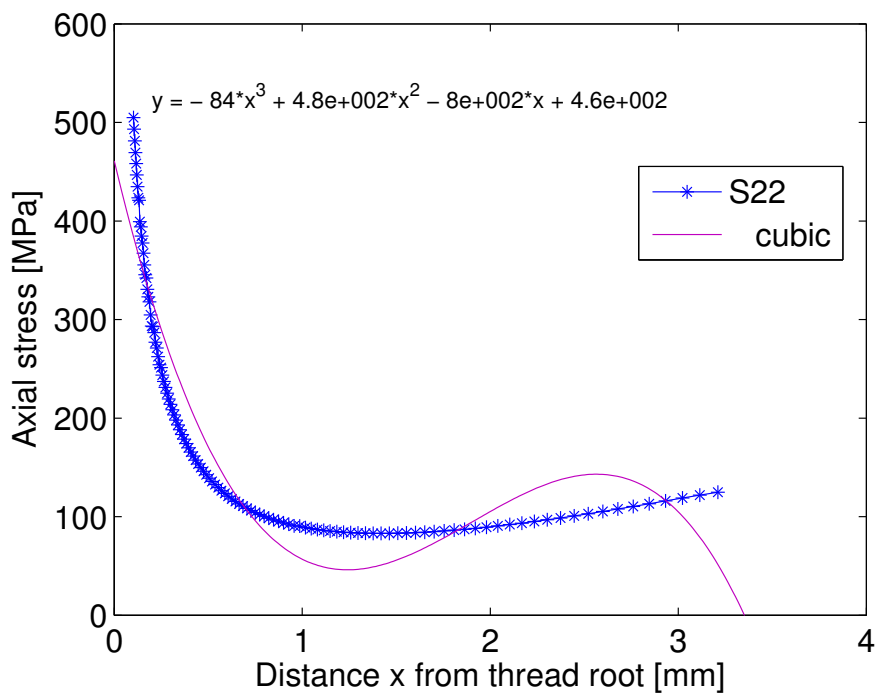


Figure B.3.: Part 2 of the axial stress distribution from the root of the LET for a tensile stress of 44.4 MPa

## B.2. Weight function method

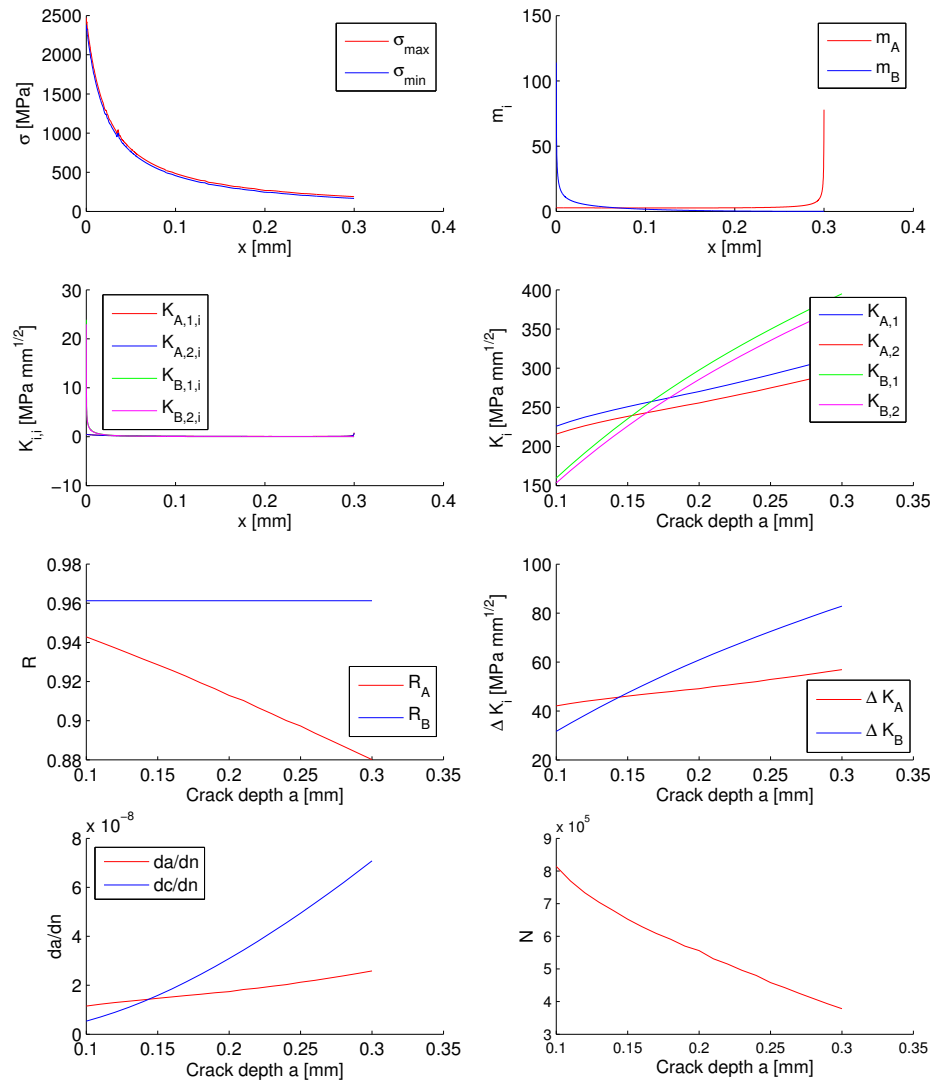


Figure B.4.: Crack growth results for a crack depth  $a = 0.3$  mm and a nominal tensile stress amplitude of 10 MPa

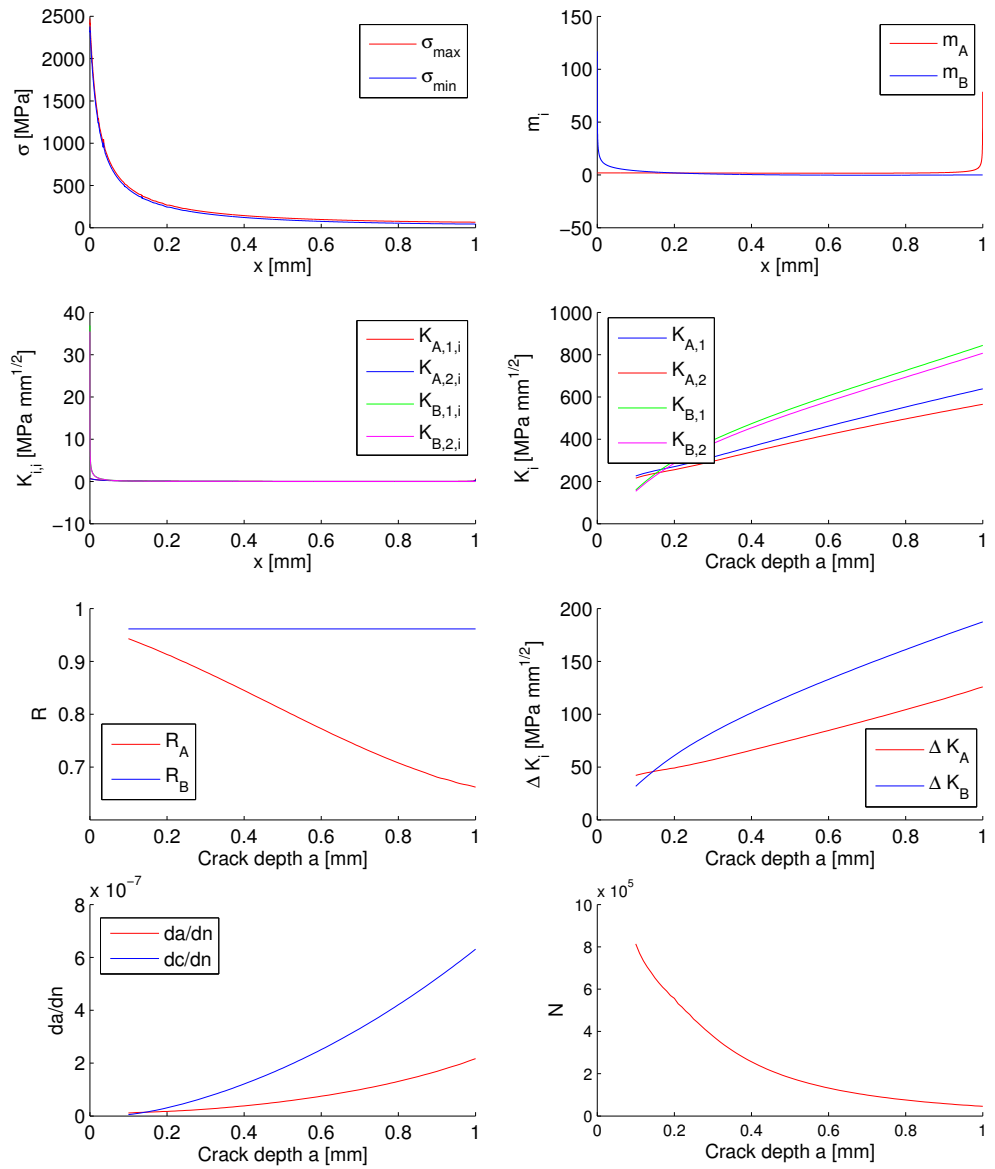


Figure B.5.: Crack growth results for a crack depth  $a = 1$  mm and a nominal tensile stress amplitude of 10 MPa

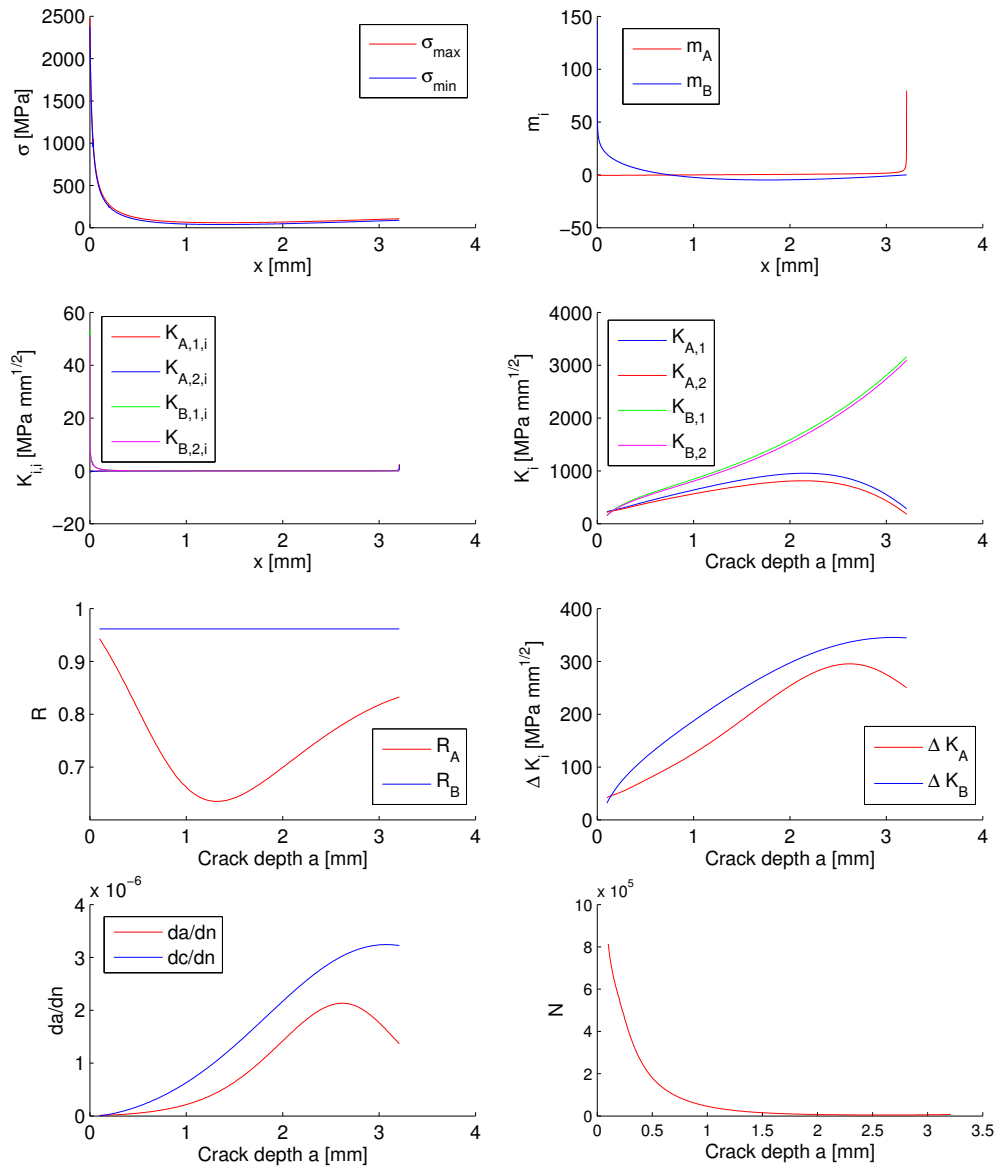


Figure B.6.: Crack growth results for a crack depth  $a = 3.21$  mm and a nominal tensile stress amplitude of 10 MPa

## C. Source code

Listing C.1: polifit.m

```
% Project thesis
% poli fit
% Moritz Braun

clc
clear all
load S22_path_80MPa.mat

x=S22_data_2(:,1);
S22=S22_data_2(:,2);

figure
hold on
plot(x,S22,'*')

n=length(x)
for t=1:6
    x_hoch(t) = sum(x.^t);
end

A=[n, x_hoch(1), x_hoch(2), x_hoch(3);...
    x_hoch(1), x_hoch(2), x_hoch(3), x_hoch(4);...
    x_hoch(2), x_hoch(3), x_hoch(4), x_hoch(5);...
    x_hoch(3), x_hoch(4), x_hoch(5), x_hoch(6)]

B = [sum(S22);sum(x.*S22);sum((x.^2).*S22);sum((x.^3).*S22)]

X = inv(A)*B

for t=1:n
    y(t) = X(1)+X(2).*x(t)+X(3).*x(t).^2+X(4).*x(t).^3;
end

plot(x,y,'-')
```

Listing C.2: weightfunc.m

```

% Project thesis
% weight function calc
% Moritz Braun

function weight_func
clear all
clc

% Input parameter
a_0 = 0.1;    %initial crack depth
c_0 = 0.5;    %initial crack width
t   = 3.2103; %wall thickness
l   = 1.3130; %notch length
R   = 0.1;

% Material parameter
m = 2.68;
gamma = 0.5;
C = 5.89E-13;
C_0 = C * (1 - R)^(m*(1-gamma));
delta_K_th = 63; %based on BS7910

%
% Stress gradient
%

load S22_path_10MPa.mat

x_t      = S22_data(:,1);
S22_t_1  = S22_data(:,3);
S22_t_2  = S22_data(:,2);
S=10
increment = 0.0001;

for k = 1:(length(S22_t_1)-1)
    B_1(k) = S22_t_1(k+1);
    A_1(k) = S22_t_1(k) - B_1(k);
    B_2(k) = S22_t_2(k+1);
    A_2(k) = S22_t_2(k) - B_2(k);
end

j=1;
n=1;
for x = (0+increment):increment:t;

```

```

x_i = x - x_t(j);

if x >= x_t(j+1)
    sig_plot_1(n) = A_1(j)*(1-x_i/(x_t(j+1)-x_t(j))) + B_1(j);
    sig_plot_2(n) = A_2(j)*(1-x_i/(x_t(j+1)-x_t(j))) + B_2(j);
    j=j+1;
else
    sig_plot_1(n) = A_1(j)*(1-x_i/(x_t(j+1)-x_t(j))) + B_1(j);
    sig_plot_2(n) = A_2(j)*(1-x_i/(x_t(j+1)-x_t(j))) + B_2(j);
end

n = n+1;
end

n=1;
for x = (0+increment):increment:(t-increment);
    B_1_fit(n) = sig_plot_1(n+1);
    A_1_fit(n) = sig_plot_1(n) - B_1_fit(n);
    B_2_fit(n) = sig_plot_2(n+1);
    A_2_fit(n) = sig_plot_2(n) - B_2_fit(n);
    n = n+1;
end

%
% Shallow semi-elliptical surface crack in a finite thickness plate
%

p=1;
c=c_0;

for a = a_0:0.01:(t);

    a_eff = a + l;
    t_eff = t + l;
    xi = a_eff/t_eff;
    chi = a/c;

    % Weightfunction

    % Deepest point
    Q = 1 + 1.464 *chi^(1.65);
    A0 = 1.0929 + 0.2581*chi - 0.7703*chi^2 + 0.4394*chi^3;
    A1 = 0.456 - 3.045*chi - 2.007*chi^2 + 1/(0.147 + chi^0.688);
    A2 = 0.995 - 1/(0.027 + chi) + 22*(1-chi)^9.953;
    A3 = -1.459 + 1/(0.014 + chi) - 24.211*(1-chi)^8.071;
    Y0 = A0 + A1*xi^2 + A2*xi^4 + A3*xi^6;

```

```

B0 = 0.4537 + 0.1231*chi - 0.7412*chi^2 + 0.46*chi^3;
B1 = -1.652 + 1.665*chi - 0.534*chi^2 + 1/(0.198 + chi^0.846);
B2 = 3.148 - 3.126*chi - 1/(0.041 + chi) + 17.259*(1-chi)^9.286;
B3 = -4.228 + 3.643*chi + 1/(0.02 + chi) - 21.924*(1-chi)^9.203;
Y1 = B0 + B1*xi^2 + B2*xi^4 + B3*xi^6;

M1A = 2*pi/(sqrt(2*Q)) * (2*Y0 - 3*Y1) - 24/5;
M2A = 3;
M3A = 6*pi/(sqrt(2*Q)) * (2*Y1 - Y0) + 8/5;

% Surface point
C0 = 1.29782 - 0.1548*chi - 0.0185*chi^2;
C1 = 1.5083 - 1.3219*chi + 0.5128*chi^2;
C2 = -1.101 - 0.879/(0.157 + chi);
F0 = (C0 + C1*xi^2 + C2*xi^4)*sqrt(chi);

D0 = 1.26827 - 1.0642*chi + 1.4646*chi^2 - 0.725*chi^3;
D1 = 1.1207 - 1.2289*chi + 0.5876*chi^2;
D2 = 0.19 - 0.608*chi + 0.199/(0.035 + chi);
F1 = (D0 + D1*xi^2 + D2*xi^4)*sqrt(chi);

M1B = 3*pi/(sqrt(Q)) * (5*F1 - 3*F0) - 8;
M2B = 15*pi/(sqrt(Q)) * (2*F0 - 3*F1) + 15;
M3B = 3*pi/(sqrt(Q)) * (10*F1 - 7*F0) - 8;

j=1;
for x = (0+increment):increment:(a-increment);
    mA(j) = 2/sqrt(2*pi*(a-x)) * (1 + M1A*(1-x/a)^(1/2) ...
        + M2A*(1-x/a) + M3A*(1-x/a)^(3/2));
    mB(j) = 2/sqrt(pi*x) * (1 + M1B*(x/a)^(1/2) ...
        + M2B*(x/a) + M3B*(x/a)^(3/2));
    j=j+1;
end

% Calculation of R-ratio at Point A & B
j=1;
for x = (a - 5*increment):increment:a;
    f = round(a/increment - 5);
    R_A_i(j) = sig_plot_2(f)/sig_plot_1(f);
    R_A(p) = sum(R_A_i)/length(R_A_i);
    R_B(p) = sig_plot_2(1)/sig_plot_1(1);
    %point B remains at the surface of a plate
    j=j+1;
end

% Integration

```



```

j=1;
for x = (0+increment):increment:(a-increment);

alpha_1(j) = B_1_fit(j) + a * A_1_fit(j);
beta_1(j) = -a * A_1_fit(j);
alpha_2(j) = B_2_fit(j) + a * A_2_fit(j);
beta_2(j) = -a * A_2_fit(j);

C_i1(j) = 2*a*((1-(x-increment)/a)^(1/2) - (1-x/a)^(1/2));
C_i2(j) = a*((1-(x-increment)/a)^(1) - (1-x/a)^(1));
C_i3(j) = 2*a/3*((1-(x-increment)/a)^(3/2) - (1-x/a)^(3/2));
C_i4(j) = a/2*((1-(x-increment)/a)^(2) - (1-x/a)^(2));
C_i5(j) = 2*a/5*((1-(x-increment)/a)^(5/2) - (1-x/a)^(5/2));
C_i6(j) = a/3*((1-(x-increment)/a)^(3) - (1-x/a)^(3));

D_i1(j) = 2*a*((x/a)^(1/2) - ((x-increment)/a)^(1/2));
D_i2(j) = a*((x/a)^(1) - ((x-increment)/a)^(1));
D_i3(j) = 2*a/3*((x/a)^(3/2) - ((x-increment)/a)^(3/2));
D_i4(j) = a/2*((x/a)^(2) - ((x-increment)/a)^(2));
D_i5(j) = 2*a/5*((x/a)^(5/2) - ((x-increment)/a)^(5/2));
D_i6(j) = a/3*((x/a)^(3) - ((x-increment)/a)^(3));

%Stress intensity factor distribution over crack depth for
%both load cases
KA1i(j) = sqrt(2/pi*a_eff) * (alpha_1(j)*(C_i1(j) + ...
M1A*C_i2(j) + M2A*C_i3(j) + M3A*C_i4(j)) + ...
beta_1(j)*(C_i3(j) + M1A*C_i4(j) + ...
M2A*C_i5(j) + M3A*C_i6(j)));

KB1i(j) = 2/sqrt(pi*a_eff) * ((alpha_1(j) + ...
beta_1(j)) * (D_i1(j) + M1B*D_i2(j) + ...
M2B*D_i3(j) + M3B*D_i4(j)) - beta_1(j)*(D_i3(j) + ...
M1B*C_i4(j) + M2B*D_i5(j) + M3B*D_i6(j)));

KA2i(j) = sqrt(2/pi*a_eff) * (alpha_2(j)*(C_i1(j) + ...
M1A*C_i2(j) + M2A*C_i3(j) + M3A*C_i4(j)) + ...
beta_2(j)*(C_i3(j) + M1A*C_i4(j) + ...
M2A*C_i5(j) + M3A*C_i6(j)));

KB2i(j) = 2/sqrt(pi*a_eff) * ((alpha_2(j) + ...
beta_2(j)) * (D_i1(j) + M1B*D_i2(j) + M2B*D_i3(j) ...
+ M3B*D_i4(j)) - beta_2(j)*(D_i3(j) + ...
M1B*C_i4(j) + M2B*D_i5(j) + M3B*D_i6(j)));

j=j+1;
end

```

```

KA1(p) = sum(KA1i);
KA2(p) = sum(KA2i);
KB1(p) = sum(KB1i);
KB2(p) = sum(KB2i);

delta_K_A(p) = abs(KA1(p) - KA2(p));
delta_K_B(p) = abs(KB1(p) - KB2(p));
delta_K_A_eff(p) = delta_K_A(p)/((1 - R_A(p))gamma);
delta_K_B_eff(p) = delta_K_B(p)/((1 - R_B(p))gamma);
if a == 0.2
    F_A = delta_K_A_eff(p)/(2*S*sqrt((pi*a)));
    S_A = delta_K_th/(2*F_A*sqrt((pi*a)));
end

da_dn(p) = C_0 * delta_K_A_eff(p)m;
dc_dn(p) = C_0 * delta_K_B_eff(p)m;

if a<t
    N(p) = (a/da_dn(p))*(1 - (a/(a+0.01))((m/2) - 1))/((m/2) - 1);
    dc = dc_dn(p)*N(p);
    c_store(p)=c;
    c = c+dc;
    a_store(p)=a;
end
p = p+1;

%Plotting of results
test_var = round(a*100);
switch test_var
case 30
    plot_figures(increment , a , a_0 , sig_plot_1 , sig_plot_2 , ...
        mA , mB , KA1i , KA2i , KB1i , KB2i , KA1 , KA2 , KB1 , KB2 , R_A , ...
        R_B , delta_K_A_eff , delta_K_B_eff , da_dn , dc_dn , N)

case 100
    plot_figures(increment , a , a_0 , sig_plot_1 , sig_plot_2 , ...
        mA , mB , KA1i , KA2i , KB1i , KB2i , KA1 , KA2 , KB1 , KB2 , R_A , ...
        R_B , delta_K_A_eff , delta_K_B_eff , da_dn , dc_dn , N)

case 321
    plot_figures(increment , a , a_0 , sig_plot_1 , sig_plot_2 , ...
        mA , mB , KA1i , KA2i , KB1i , KB2i , KA1 , KA2 , KB1 , KB2 , R_A , ...
        R_B , delta_K_A_eff , delta_K_B_eff , da_dn , dc_dn , N)
end

end

```

```

N_total = sum(N)

a_plot = a_store(1:10:end);
c_plot = c_store(1:10:end);

figure
hold on
xlhand = get(gca, 'xlabel');
set(xlhand, 'string', 'c_[mm]', 'fontsize', 16);
ylhand = get(gca, 'ylabel');
set(ylhand, 'string', 'a_[mm]', 'fontsize', 16);

for j=1:length(a_plot)
    plot_ellipse(a_plot(j), c_plot(j))
    j=j+1;
end
axis('tight')
end

function plot_ellipse(a_plot, c_plot)

    c=c_plot; %horizontal radius
    a=a_plot; %vertical radius
    x0=0; % x0, y0 ellipse centre coordinates
    y0=0;
    t=linspace( 0, pi, 100);
    x=x0+c*cos(t);
    y=y0+a*sin(t);
    plot(x,y)

end

function plot_figures(increment, a, a_0, sig_plot_1, sig_plot_2, ...
    mA, mB, KA1i, KA2i, KB1i, KB2i, KA1, KA2, KB1, KB2, R_A, R_B, ...
    delta_K_A, delta_K_B, da_dn, dc_dn, N)

    fontsize_plot = 12;

    x = (0+increment):increment:(a-increment);
    a_plot = (a_0):0.01:(a);
    figure
    subplot (4, 2, 1);
    for z = 1:length(x)
        S1_plot(z) = sig_plot_1(z);
        S2_plot(z) = sig_plot_2(z);
    end
    hold on

```

```

plot(x,S1_plot,'r-')
plot(x,S2_plot,'b-')
hleg1 = legend('\ $\sigma_{\max}$ ', ' $\sigma_{\min}$ ');
set(gca, 'FontSize', fontsize_plot);
xlhand = get(gca, 'xlabel');
set(xlhand, 'string', 'x_[mm]', 'fontsize', fontsize_plot);
ylhand = get(gca, 'ylabel');
set(ylhand, 'string', ' $\sigma_{[MPa]}$ ', 'fontsize', fontsize_plot);

subplot (4, 2, 2);
hold on
plot(x,mA, 'r-')
plot(x,mB, 'b-')
hleg1 = legend('m_{A}', 'm_{B}');
set(gca, 'FontSize', fontsize_plot);
xlhand = get(gca, 'xlabel');
set(xlhand, 'string', 'x_[mm]', 'fontsize', fontsize_plot);
ylhand = get(gca, 'ylabel');
set(ylhand, 'string', 'm_i', 'fontsize', fontsize_plot);

subplot (4, 2, 3);
hold on
plot(x,KA1i, 'r-')
plot(x,KA2i, 'b-')
plot(x,KB1i, 'g-')
plot(x,KB2i, 'm-')
hleg1 = legend('K_{A,1,i}', 'K_{A,2,i}', 'K_{B,1,i}', 'K_{B,2,i}');
set(gca, 'FontSize', fontsize_plot);
xlhand = get(gca, 'xlabel');
set(xlhand, 'string', 'x_[mm]', 'fontsize', fontsize_plot);
ylhand = get(gca, 'ylabel');
set(ylhand, 'string', 'K_{i,i}_{[MPa_{mm}^{1/2}]}' , 'fontsize', fontsize_plot);

subplot (4, 2, 4);
hold on
plot(a_plot,KA1, 'b-')
plot(a_plot,KA2, 'r-')
plot(a_plot,KB1, 'g-')
plot(a_plot,KB2, 'm-')
hleg1 = legend('K_{A,1}', 'K_{A,2}', 'K_{B,1}', 'K_{B,2}');
set(gca, 'FontSize', fontsize_plot);
xlhand = get(gca, 'xlabel');
set(xlhand, 'string', 'Crack_depth_a_[mm]', 'fontsize', fontsize_plot);
ylhand = get(gca, 'ylabel');
set(ylhand, 'string', 'K_i_{[MPa_{mm}^{1/2}]}' , 'fontsize', fontsize_plot);

subplot (4, 2, 5);

```

```

hold on
plot(a_plot,R_A,'r-')
plot(a_plot,R_B,'b-')
hleg1 = legend('R_A','R_B');
set(gca,'FontSize',fontsize_plot);
xlhand = get(gca,'xlabel');
set(xlhand,'string','Crack_depth_a [mm]','fontsize',fontsize_plot);
ylhand = get(gca,'ylabel');
set(ylhand,'string','R','fontsize',fontsize_plot);

subplot (4, 2, 6);
hold on
plot(a_plot,delta_K_A,'r-')
plot(a_plot,delta_K_B,'b-')
hleg1 = legend('Delta_K_A','Delta_K_B');
set(gca,'FontSize',fontsize_plot);
xlhand = get(gca,'xlabel');
set(xlhand,'string','Crack_depth_a [mm]','fontsize',fontsize_plot);
ylhand = get(gca,'ylabel');
set(ylhand,'string','Delta_K_i [MPa_mm^{1/2}]','fontsize',fontsize_plot);

subplot (4, 2, 7);
hold on
plot(a_plot,da_dn,'r-')
plot(a_plot,dc_dn,'b-')
hleg1 = legend('da/dn','dc/dn');
set(gca,'FontSize',fontsize_plot);
xlhand = get(gca,'xlabel');
set(xlhand,'string','Crack_depth_a [mm]','fontsize',fontsize_plot);
ylhand = get(gca,'ylabel');
set(ylhand,'string','da/dn','fontsize',fontsize_plot);

subplot (4, 2, 8);
hold on
plot(a_plot,N,'r-')
xlhand = get(gca,'xlabel');
set(xlhand,'string','Crack_depth_a [mm]','fontsize',fontsize_plot);
ylhand = get(gca,'ylabel');
set(ylhand,'string','N','fontsize',fontsize_plot);

```

**end**